



Numerical Simulation of Pulverized Coal Combustion

Der Fakultät für Maschinenbau, Verfahrens- und Energietechnik
der Technischen Universität Bergakademie Freiberg

vorgelegte

Dissertation

zur Erlangung des akademischen Grades

Doktor-Ingenieur
(Dr.-Ing.)

vorgelegt von

Dipl.-Math. Danny Messig

geboren am 17. April 1985 in Zschopau

Tag der Einreichung: 07. Juli 2017

1. Gutachter: Prof. Dr.-Ing. Christian Hasse
2. Gutachter: Prof. Dr. rer. nat. habil. Michael Eiermann

ERKLÄRUNG

Ich versichere, dass ich diese Arbeit selbständig verfasst und keine anderen Hilfsmittel als die angegebenen benutzt habe. Die Stellen der Arbeit, die anderen Werken dem Wortlaut oder dem Sinn nach entnommen sind, habe ich in jedem einzelnen Fall unter Angabe der Quelle als Entlehnung kenntlich gemacht. Diese Versicherung bezieht sich auch auf die bildlichen Darstellungen.

Teile dieser Arbeit wurden bereits in folgenden Publikationen veröffentlicht:

1. D. Messig, F. Hunger, J. Keller, and C. Hasse. Evaluation of radiation modeling approaches for non-premixed flamelets considering a laminar methane air flame. *Combustion and Flame*, 160:251-264, 2013.
2. S. Weise, D. Messig, B. Meyer, and C. Hasse. An abstraction layer for efficient memory management of tabulated chemistry and flamelet solutions. *Combustion Theory and Modelling*, 17(3):411-430, 2013.
3. U. Prüfert, S. Hartl, F. Hunger, D. Messig, M. Eiermann, and C. Hasse. A constrained control approach for the automated choice of an optimal progress variable for chemistry tabulation. *Flow Turbulence and Combustion*, 94(3):593-617, 2015.
4. B. Garten, F. Hunger, D. Messig, B. Stelzner, D. Trimis, and C. Hasse. Detailed radiation modeling of a partial-oxidation flame. *International Journal of Thermal Sciences*, 87:68- 84, 2015.
5. S. Popp, F. Hunger, S. Hartl, D. Messig, B. Coriton, J.H. Frank, F. Fuest, and C. Hasse. LES flamelet-progress variable modeling and measurements of a turbulent partially-premixed dimethyl ether jet flame. *Combustion and Flame*, 162(8):3016-3029, 2015.
6. D. Messig, M. Vascellari, and C. Hasse. Flame structure analysis and flamelet progress variable modelling of strained coal flames. *Combustion Theory and Modelling*, in press.
7. S. Weise, S. Popp, D. Messig and C. Hasse. A computationally efficient implementation of tabulated combustion chemistry based on polynomials and automatic source code generation. *Flow, Turbulence and Combustion*, in press.

Bei der Auswahl und Auswertung des Materials sowie bei der Herstellung des Manuskripts habe ich Unterstützung von folgenden Personen erhalten:

- Prof. Dr.-Ing. Christian Hasse
- Anne Allen Koth (Englisch-Korrektur)

Weitere Personen waren an der Abfassung der vorliegenden Arbeit nicht beteiligt. Die Hilfe eines Promotionsberaters habe ich nicht in Anspruch genommen. Weitere Personen haben von mir keine geldwerten Leistungen für Arbeiten erhalten, die nicht als solche kenntlich gemacht worden sind.

Die Arbeit wurde bisher weder im Inland noch im Ausland in gleicher oder ähnlicher Form einer anderen Prüfungsbehörde vorgelegt.

DANKSAGUNG

Die vorliegende Arbeit ist am Institut für Energieverfahrenstechnik und Chemieingenieurwesen am Lehrstuhl für Numerische Thermofluiddynamik entstanden.

Zunächst möchte ich mich herzlich bei Professor Christian Hasse für die Möglichkeit, diese Arbeit als Mitarbeiter der Professur Numerische Thermofluiddynamik zu erstellen, bedanken. Meinen Dank möchte ich ihm besonders für die zahlreichen Diskussionen, Ideen und vor allem für seine zur Verfügung gestellte Zeit sowie für sein Interesse am Gelingen dieser Arbeit aussprechen.

Professor Michael Eiermann danke ich für sein Interesse an dieser Arbeit und die Übernahme des Zweitgutachtens.

Weiterhin möchte ich meinen Dank an Professor Bernd Meyer zum Ausdruck bringen, welcher mir den Einstieg in die akademische Welt als wissenschaftlicher Mitarbeiter ermöglichte. Die Tätigkeit an seiner Professur befähigte mich als Mathematiker, die gestellten physikalischen bzw. technischen Problemstellungen zu erfassen und schließlich zu bearbeiten.

Nicht vergessen möchte ich auch die (ehemaligen) Kollegen der EVT und NTFD: Vielen Dank für die gute Zusammenarbeit sowie die gute Arbeitsatmosphäre. Besonders danken möchte ich dabei Steffen Weise für die gemeinsame Zeit zur Bereitstellung eines stabilen Workflows zur Benutzung der Flamelettabellen in zahlreichen CFD Programmen. Weiterhin sei Arne Scholtissek und Axel Zschutschke für die gemeinsame Entwicklung unseres Software Projektes ULF gedankt. Nicht zu vergessen: Dr. Michele Vascellari, welcher viel zum Gelingen der Arbeit im Bereich der Kohlemodellierung beigetragen hat.

Für die Hinweise und Korrekturvorschläge gilt mein Dank Martin Pollack, Arne Scholtissek, Michele Vascellari und Steffen Salenbauch.

Ebenfalls möchte ich mich bei Prof. Nasser Darabiha, Prof. Benoît Fiorina und Meng Xia vom École Centrale in Paris bedanken für die Bereitstellung der experimentellen Daten und die ergiebigen Diskussionen.

Dank auch an meinen großen Bruder Rico, welcher mich früh Durchsetzungsvermögen im Leben lehrte.

Zuletzt gilt mein Dank meinen Eltern Dietmar und Karina für alle ihre Liebe und Unterstützung, speziell auch in der stressigen Zeit. Ohne Sie wäre ich nicht da, wo ich jetzt bin.

Freiberg, 2017

Danny Messig

KURZFASSUNG

Die Arbeit befasst sich mit der Flamelet Modellierung für die Verbrennung von Kohlenstaub. Dabei liegt der Fokus sowohl auf der detaillierten Betrachtung der Gasphasenchemie als auch auf der Interaktion der Kohle mit der Gasphase. Ziel der Arbeit ist die Entwicklung einer Methode für die Simulation großtechnischer Kohlestaubfeuerungen.

Die energetische Umsetzung von Kohle läuft in drei wesentlichen Schritten ab: Verdampfung der Feuchtigkeit, Ausgasung der Kohle (Pyrolyse) und schließlich der Koksabbrand. Da die Struktur der Kohle als fossiler Brennstoff hoch komplex ist, existieren viele prädiktive, rechenaufwändige Modelle zur Beschreibung dieser Prozesse [1–4]. Diese Modelle können nicht direkt in numerischen Strömungssimulationen genutzt werden, dienen aber zur Kalibrierung einfacherer kinetischer Modelle. Diese in der Arbeit angewendete Prozedur wird in [5] beschrieben.

Zur detaillierten Beschreibung des Abbaus der entstehenden höheren Kohlenwasserstoffe werden in der Simulation große Reaktionsmechanismen benötigt. Die Benutzung solcher Mechanismen ist mit großen Rechenzeiten verbunden und daher bleibt deren Anwendbarkeit auf einfache Anwendungsfälle beschränkt. Der Vorteil der Flamelet Modellierung besteht darin, dass unter bestimmten Voraussetzungen der komplette thermo-chemische Zustand, bestehend aus Temperatur, Druck und Zusammensetzung, mit nur wenigen charakterisierenden Kontrollvariablen abgebildet werden kann. Durch Vorgabe und Variation der Kontrollvariablen können diese Zustände mittels kanonischer Flammenkonfigurationen vorberechnet und in sogenannten Flamelettabellen abgespeichert werden. Für das klassische Flamelet / Fortschrittsvariablen Modell [6] wird der thermo-chemische Zustand über Mischungsbruch und Fortschrittsvariablen parametrisiert, dabei bestimmt der Mischungsbruch den Anteil an Brennstoff im Gemisch und die Fortschrittsvariable den Fortschritt der chemischen Reaktion. Die Kontrollvariablen werden in der numerischen Simulation transportiert, an Stelle der Energie- und Speziesgleichungen. Dies stellt für große Mechanismen eine dramatische Reduktion der zu lösenden Gleichungen dar. Der thermo-chemische Zustand ergibt sich per Look-up aus den Flamelettabellen.

Im Zuge der Verbrennung trockener Kohle werden zwei Brennstoffe durch Pyrolyse und Koksabbrand freigesetzt. Für die Flamelet Modellierung bedeutet dies entsprechend je einen Mischungsbruch für Pyrolysegas und Produkte aus dem Koksabbrand. Neben der Fortschrittsvariablen wird ebenfalls die Enthalpie der Gasphase als Kontrollvariable benötigt aufgrund des intensiven Wärmeaustauschs zwischen Kohle und Gasphase. In der Arbeit erfolgt die Vorstellung der benötigten Transportgleichungen sowie die Beschreibung verschiedener Methoden zur Integration nicht-adiabater Zustände in Flamelettabellen. Dabei unterscheiden sich die vorgestellten Tabellierungsstrategien hauptsächlich in der betrachteten Verbrennungsart.

Erfolgt die Mischung von Brennstoff und Oxidationsmittel erst in der untersuchten Flammenkonfiguration, spricht man von Diffusionsflammenstrukturen; sind beide schon gemischt, so entstehen Vormischflammenstrukturen. Die Detektion solcher Strukturen erfolgt in der Arbeit anhand einer Flammenstrukturanalyse mittels Flammenmarker. Die prinzipielle Übertragbarkeit des Flamelet / Fortschrittsvariablen Modells auf turbulente Kohlestaubfeuerung wurde von Watanabe [7] gezeigt, jedoch ist die Bewertung der eingesetzten Flamelet Modellierung in Grobstruktursimulationen nicht ohne weiteres möglich. Deshalb werden zur Verifizierung der entwickelten Tabellierungsstrategie in der Arbeit einfache Flammenkonfigurationen betrachtet, die es erlauben, direkte Chemielösungen mit den Lösungen der tabellierten Chemie zu vergleichen. Für den entsprechenden Vergleich erfolgt die Vorstellung zweier Analysen. Bei der *a priori* Analyse wird der thermo-chemische Zustand der detaillierten Lösung mit dem tabellierten Zustand verglichen. Für den Look-up werden dabei die Kontrollvariablen der direkten Chemiesimulation benutzt. Die *a posteriori* Analyse ist der Vergleich einer voll gekoppelten Rechnung unter Benutzung der Tabellierungsstrategie mit der zugehörigen detaillierten Rechnung.

Die erste untersuchte Konfiguration stellt eine Gegenstromanordnung mit vorgewärmter Luft und Kohlebeladung dar. Die Hauptergebnisse dieser rein numerischen Studie wurden bereits veröffentlicht [8] und es konnte die erfolgreiche Applikation der vorgestellten Tabellierungsstrategie in dieser Anordnung für Tabellen basierend auf Diffusionsflammenstrukturen gezeigt werden.

Für die Validierung der detaillierten Rechnungen erfolgt die Nutzung experimenteller Daten [9, 10] für magere Methan-Sauerstoff-Stickstoff Mischungen in Staupunktströmungen. Es zeigt sich, dass diese Konfigurationen stark von den vorgemischten Gasflammen dominiert werden und somit Tabellen basierend auf Vormischflammenstrukturen einzusetzen sind. Die entwickelte Tabellierungsmethode ist in der Lage, auch diese Flammenstrukturen abzubilden.

Abschließend wird numerisch eine Parametervariation hinsichtlich Einlassgeschwindigkeit und Kohlebeladung vorgestellt, um die Robustheit und breite Anwendbarkeit der entwickelten Tabellierungsstrategie aufzuzeigen.

Zusammenfassend konnte mittels Flammenstrukturanalyse für jede vorgestellte Konfiguration der zu verwendende Typ der Tabelle bestimmt werden. In den untersuchten Konfigurationen führte deren Anwendung zu einer guten Übereinstimmung mit den detaillierten Rechnungen. Damit legt diese Arbeit den Grundstein für weiterführende Betrachtung zur Simulation großtechnischer Kohlestaubfeuerungen.

ABSTRACT

The dissertation addresses the flamelet modeling of pulverized coal combustion. The focus will be on a detailed consideration of the gaseous phase kinetics as well as the interaction of coal with the gaseous phase. The aim of this work is to develop a method for the simulation of large scale pulverized coal combustor.

The coal conversion proceeds in three important steps: vapor evaporation, the devolatilization process and finally the char burnout. As a fossil fuel, coal has a complex structure; therefore, there are several detailed, computationally expensive models to describe these processes [1–4]. These models cannot be directly applied for computational fluid dynamics (CFD) simulations, but can be used to calibrate easier kinetic models. This procedure, described in [5], is used throughout this thesis.

In order to characterize the breakdown of the released higher hydrocarbons in simulations, large reaction schemes are necessary. Such mechanisms are connected with high computational costs and therefore, only affordable in simple configurations. The advantage of flamelet modeling is the possibility to describe the thermo-chemical state, consisting in the temperature, pressure and composition, under certain assumptions with only few characterizing control parameters. By prescribing and varying the parameters, these states can be, by using canonical flame configuration, precalculated and finally tabulated. These tables are called flamelet look-up tables. For the classical Flamelet/Progress Variable (FPV) [6] approach the thermo-chemical state is parameterized by the mixture fraction and progress variable. The mixture fraction specifies the ratio of fuel in the mixture and the progress variable tracks the chemical reaction. The control variables are transported in the numerical simulation instead of energy and species equations. For large mechanisms this means a dramatic decrease in the number of transport equations. The thermo-chemical state is looked up in the flamelet tables depending on the control parameters.

Two fuel streams formed by pyrolysis and char burnout are released during the combustion of dry coal. For flamelet modeling, this means one mixture fraction for the volatiles and one for the products of char burnout. Beside the progress variable, the enthalpy is also necessary to describe non-adiabatic conditions due to the exchange of heat between the coal particles and gaseous phase. This thesis presents the corresponding transport equations and describes different models to deal with the integration of non-adiabatic states in the flamelet tables. The proposed tabulation strategies mainly depend on the burning mode considered. If the mixing of fuel and oxidizer takes place within the flame configuration investigated then a non-premixed flame structure is obtained, whereas if they are already mixed then a premixed flame structure follows. The detection of such structures throughout this work is carried out with a flame structure analysis by investigating flame markers. The theoretical portability of

the FPV approach for modeling turbulent pulverized coal combustion was shown by [7], but the evaluation of the flamelet modeling used in large eddy simulations is not straightforward. Therefore, one aim of this thesis is to directly analyse the selected tabulation strategy. To verify the tabulation strategies proposed, simple configurations are considered in the thesis, which allow detailed chemistry solutions to be compared with results obtained for tabulated chemistry. For this comparison, two analyses are presented. The *a priori* analysis compares the thermo-chemical state of the direct chemistry simulation with the tabulated one. For the look-up, the control variables from the detailed simulation are used. The *a posteriori* analysis is the comparison of a detailed simulation with the corresponding fully coupled calculation by using the tabulation strategy.

The first configuration investigated is a counterflow with preheated air and coal loading. The main results of this numerical study have already been published [8] and the applicability of the proposed tabulation method is shown for this non-premixed-driven setup.

To validate of the detailed simulations, experimental data [9, 10] on lean methane-oxygen-nitrogen mixtures in stagnation flows are used. It becomes apparent, that these configurations are dominated by the premixed gaseous flames and therefore tables based on premixed flames have to be applied. The tabulation strategy developed has the ability to capture this flame structures.

Finally, a parametric study of inlet velocity and coal loading is conducted numerically to show the robustness of the proposed tabulation strategy.

In conclusion, based on the respective flame structure analysis it was possible to determine the necessary burning mode for the table for the configurations investigated. The application of these tables in a fully coupled simulation leads to good agreement with the detailed calculation results. Therefore, this thesis lays the foundation for further investigations aimed at simulating large-scale pulverized coal combustors.

CONTENTS

LIST OF FIGURES	X
LIST OF TABLES	XIV
NOMENCLATURE	XV
1 INTRODUCTION	1
2 PHYSICAL MODEL FORMULATIONS	5
2.1 Coal models	5
2.1.1 Thermodynamic coal properties	6
2.1.2 Thermo-chemical conversion of coal	7
2.2 Conservation equations for laminar reactive flows	9
2.2.1 Equations for gaseous phase	9
2.2.2 Equations for dispersed solid phase	11
2.2.3 Fully coupled Transport and Chemistry (FTC) model for gas and solid phase	12
2.3 Flamelet modeling and tabulation strategies	14
2.3.1 Flamelet modeling for laminar non-premixed flames	14
2.3.2 Flamelet modeling for laminar premixed flames	16
2.3.3 Flamelet tabulation and coupling strategies	17
2.3.4 Flamelet tabulation for turbulent flames	21
2.3.5 Non-adiabatic flamelet look-up tables	22
2.3.6 Flamelet/Progress Variable (FPV) model for laminar coal flames . . .	28
2.3.7 Flamelet tabulation for turbulent coal flames	31
3 RESULTS	34
3.1 Counterflow flames	34
3.1.1 Flame structure analysis in strained counterflow coal flames	36
3.1.2 <i>A priori</i> analysis of flamelet look-up tables	39
3.1.3 Influence of different enthalpy levels in the flamelet look-up table . . .	39
3.1.4 The <i>a posteriori</i> analysis for a non-adiabatic DFLUT	41
3.1.5 Intermediate summary for counterflow flames	43
3.2 Stagnation flow flames reported by Xia et al. [9]	43
3.2.1 Methane-air flame	44
3.2.2 Coal-methane-air flame	48
3.2.3 Intermediate summary for stagnation flow flames reported in [9] . . .	58
3.3 Modified stagnation flow case for enhanced char-burnout	58
3.3.1 Validation	59
3.3.2 Parametric study	60
4 SUMMARY AND CONCLUSIONS	67

CONTENTS

A	APPENDIX	70
A.1	Detailed description of the solution procedure	70
A.1.1	Modified damped Newton's method with pseudo time stepping	70
A.1.2	Lagrangian tracking	71
A.2	Derivation of flamelet model for non-premixed flames	72
	REFERENCES	76

LIST OF FIGURES

Figure 1.1	Energy consumptions by source: facts and predictions [11].	1
Figure 1.2	Overview of selected submodels for PCC modeling. The dashed region marks the region of interest in this thesis.	1
Figure 1.3	Illustration of modular units, nuclei, bridges and chains in a coal molecule [12]. Unit A: aromatic nucleus, Unit B: partially hydrogenated nucleus, Unit C: biphenyl nucleus.	2
Figure 1.4	Details on resolution quality for different turbulence modeling. Adapted from [13].	3
Figure 2.1	Schematics for the gaseous strained flow configurations investigated by [9, 14].	10
Figure 2.2	Schematics for the particle loaded strained flow configurations investigated by [8, 9].	13
Figure 2.3	Sketch of typical non-premixed flame.	15
Figure 2.4	Sketch of canonical premixed flames.	16
Figure 2.5	The hatched region shows the valid states $\varphi(Z, Y_c)$ for a methane-air mixture with an initial temperature of 300 K. The grey region contains no valid solutions. The PV is defined as $Y_c := Y_{CO} + Y_{CO_2} + Y_{H_2} + Y_{H_2O}$	18
Figure 2.6	Workflow of look-up properties from FLUT. Adapted from [15] . . .	18
Figure 2.7	The S-shaped curve is obtained by plotting the maximum temperature T_{max} over the inverse of the SDR in logarithmic scale of the abscissa.	19
Figure 2.8	Selected curves of a DFLUT for a methane-air mixture for an initial temperature of 300 K. The PV is defined as $Y_c := Y_{CO} + Y_{CO_2} + Y_{H_2} + Y_{H_2O}$. Left: PV profiles for three selected χ_{st} over Z , right: PV profiles for two selected Z over χ_{st}	20
Figure 2.9	Flammability limits $[Z_{min}, Z_{max}]$ for a stoichiometric premixed methane-air flame with $T_{fr} = 300$ K.	21
Figure 2.10	Results of flamelet profiles for temperature showing solutions for an adiabatic flamelet and a flamelet with constant enthalpy shift over mixture fraction range.	23
Figure 2.11	Results of transient flamelet profiles for temperature at different times obtained for an stoichiometric methane-air mixture.	24
Figure 2.12	Results of steady flamelet profiles for temperature at different values of the scaling factor α	25
Figure 2.13	Detailed sketch of a burner-stabilized flame.	26

LIST OF FIGURES

Figure 2.14	A freely propagating flame with an initial temperature value of 600 K and burner-stabilized flame with an initial temperature value of 1000 K expressed in physical space (left) and composition space (right). The solid lines are solutions for the FP flame and the circles correspond to the BS flame. The temperature is marked in red whereas the mass fractions of OH are denoted in blue.	27
Figure 2.15	Workflow of look-up properties from non-adiabatic FLUTs.	28
Figure 2.16	Transformation of mixture fractions Z_{vol} and Z_{char} into $Z_{\text{sum}}-Y$ space. The valid region of the mixture fraction is limited to the necessity of oxygen for char burnout. For air thus follows that $\alpha_{cb} \approx 5.72$ and $Z_{\text{char,max}} \approx 0.149$	30
Figure 2.17	Sketch of the <i>a priori</i> analysis for FLUTs.	31
Figure 2.18	Sketch of the <i>a posteriori</i> analysis for FLUTs.	32
Figure 3.1	The flame structure analysis of the strained coal counterflow flames for the cases listed in Table 3.3. The vertical dashed lines mark the stagnation planes. The horizontal dashed lines in the third row indicate the stoichiometric mixture ($Z_{\text{st}} = 0.096$). The horizontal dashed lines in the last row show $\gamma_e = 0$ and the marked points indicate the zero-crossing of γ_e	38
Figure 3.2	The <i>a priori</i> analysis of a DFLUT (circles) and a PFLUT (squares) for all the three cases (Tables 3.3). FTC results (solid lines) are used as reference solutions. The vertical dashed lines mark the stagnation planes. The horizontal dashed lines in the first row indicate the stoichiometric mixture fraction ($Z_{\text{st}} = 0.096$).	39
Figure 3.3	<i>A priori</i> analysis using a DFLUT. Circles (<i>H</i>) show the results for a table with multiple levels of enthalpy. Squares (<i>No corr.</i>) and triangles (<i>T corr.</i>) show the results for an adiabatic table with and without temperature correction, respectively. The vertical dashed lines mark the stagnation plane.	40
Figure 3.4	The <i>a posteriori</i> analysis of the DFLUT FPV (dashed lines) comparing results from the FTC (solid lines) as reference solutions for all the cases listed in Table 3.3. The vertical dashed lines mark the stagnation plane. The horizontal dashed lines in the first row show the stoichiometric mixture fraction ($Z_{\text{st}} = 0.096$).	42
Figure 3.5	Direct views on the investigated flames [16].	43
Figure 3.6	Comparison of profiles in physical space for the mechanisms listed in Table 3.4: left plot: temperature, right plot: normalized OH mole fraction profiles compared to experiments [9].	45
Figure 3.7	Comparison of profiles for different diffusion modeling approaches using GRI-3.0 mechanism: left plot: temperature, right plot: normalized OH mole fraction profiles compared to experiments [9].	45

LIST OF FIGURES

Figure 3.8	Comparison of normalized $\text{CH}\cdot$ (left) and $\text{C}_2\cdot$ (right) mole fraction profiles between numerical and experimental results using Xia-Mech mechanism.	46
Figure 3.9	The flame structure analysis of the strained methane-air stagnation flow for Xia-Mech.	46
Figure 3.10	The <i>a posteriori</i> analysis for the strained methane-air stagnation flow for mixture-averaged diffusion modeling and CRECK-based mechanism.	47
Figure 3.11	The <i>a posteriori</i> analysis for the strained methane-air stagnation flow for $\text{Le}=1$ diffusion modeling and CRECK-based mechanism.	48
Figure 3.12	Influence of introducing coal on the position of the flame front in the coal-methane-air stagnation flow flame using MA-diffusion approach and the Xia-Mech mechanism. Left plot: temperature profiles, right plot: normalized X_{OH} profiles.	49
Figure 3.13	Flame structure analysis for the coal-methane-air case investigated by Xia et al. [9]. Upper left: temperature of gaseous phase and dispersed phase as well as the PV, upper right: flamelet parameters Z_{vol} , Z_{vol}, Y and the local equivalence ratio ϕ_{local} , lower left: major species profiles, lower right: flame markers γ_e and $\dot{\omega}_T$	50
Figure 3.14	The <i>a posteriori</i> analysis with a PFLUT for the reference case. Upper left: flamelet parameters Z_{vol} , Z_{vol}, Y_c , upper right: total enthalpy h_g , lower left: temperature, right: normalized X_{OH} profiles.	51
Figure 3.15	Comparison of coal-methane-air stagnation flow with experiments including coal [9].	52
Figure 3.16	Comparison of profiles for two mechanisms, left plot: temperature, right plot: normalized OH mole fraction profiles compared to experiments [9].	52
Figure 3.17	The RRSB distribution. Left: RRSB-PDF as in Eq. (3.6) and the corresponding approximation, right: mass fractions of particle classes as in Table 3.7.	53
Figure 3.18	Comparison of mono-disperse distribution and the RRSB distribution. Left: temperature, right: mole fraction of OH.	54
Figure 3.19	Comparison of mono-disperse distribution and the RRSB distribution. Left: Particle temperatures, right: mixture fractions and ϕ_{local}	54
Figure 3.20	Arrhenius diagram for kinetic rates k_{vol} for both coals HP and SP.	55
Figure 3.21	Influence of coal types on the position of the flame front, left plot: temperature, right plot: normalized OH mole fraction profiles compared to experiments [9].	56
Figure 3.22	Results of coal-methane-air stagnation flame with the optimized parameter compared with experiments including coal [9].	57

LIST OF FIGURES

Figure 3.23	Comparison of numerical results and experimental data for the case of the modified methane-enriched-air stagnation flow. Upper left: temperature of the gas-phase, upper right: normalised X_{OH} profiles, lower left: normalised X_{CH} profile and lower right: normalised X_{C_2}	59
Figure 3.24	Comparison of numerical results and experimental data for the case of the modified coal-methane-enriched-air stagnation flow case. Upper left: particle temperature and temperature of the gas-phase, upper right: normalised X_{OH} profiles, lower left: normalised X_{CH} profile and lower right: normalised X_{C_2}	60
Figure 3.25	Influence of inlet velocity on the flame structure of a coal-oxidizer stagnation flame with fixed coal-to-oxidizer ratio $\alpha_{in} = 0.066$	61
Figure 3.26	Influence of coal loading on the flame structure of a coal-oxidizer stagnation flame with fixed inlet velocity $v_{in} = 2.0 \frac{m}{s}$	63
Figure 3.27	The <i>a posteriori</i> analysis of a coal-oxidizer stagnation flame with fixed coal-to-oxidizer ratio $\alpha_{in} = 0.066$ and a varied the inlet velocity. The dashed lines are the results of the FPV model and solid lines representing the FTC solutions.	64
Figure 3.28	The <i>a posteriori</i> analysis of a coal-oxidizer stagnation flame with fixed inlet velocity $v_{in} = 2.0 \frac{m}{s}$ by varying the coal-to-oxidizer ratio α_{in} . The dashed lines are the results of the FPV-model and solid lines representing the FTC-solutions.	66

LIST OF TABLES

Table 2.1	Boundary conditions of premixed stoichiometric methane-air flames [17].	26
Table 3.1	Proximate and ultimate analysis of Pittsburgh coal as received. . . .	35
Table 3.2	Parameters of the SFOR devolatilization model and volatile composition for the Pittsburgh coal fitted according to [5].	35
Table 3.3	Input conditions for the reference cases.	36
Table 3.4	Details on mechanisms used to validate FTC model for methane-air stagnation flame.	44
Table 3.5	Proximate and ultimate analysis of Heizprofi (HP) lignite [9].	48
Table 3.6	Parameters of the SFOR devolatilization model and volatile composition for Heizprofi (HP) lignite.	49
Table 3.7	Mass fractions of the particle size distribution based on RRSB.	53
Table 3.8	Proximate and ultimate analysis of South Beulah (SB) lignite [9]. . . .	55
Table 3.9	Parameters of the SFOR devolatilization model and volatile composition for South Beulah (SB) lignite.	55
Table 3.10	Optimized parameters of the SFOR devolatilization model and volatile composition for Heizprofi (HP) lignite.	56
Table 3.11	Input parameters for the parametric study of the modified stagnation flow cases.	60

NOMENCLATURE

ABBREVIATIONS

<i>Symbol</i>	<i>Meaning</i>
DFLUT	Diffusion flamelet look-up table
PFLUT	Premixed flamelet look-up table
BS	Burner-stabilized premixed flame
BYU	Brigham Young University
CBC	Workshop on measurement and simulation of coal and biomass conversion
CBK	Carbon burnout kinetics
CCS	Carbon capture and sequestration/storage
CEMA	Chemical explosion mode analysis
CFD	Computational fluid dynamics
CPD	Chemical percolation devolatilization
CRIEPI	Central Research Institute of Electric Power Industry
DNS	Direct numerical simulation
FG-DVC	Combination of functional group and depolymerization-vaporization-cross-linking method
FLUT	Flamelet look-up table
FP	Freely propagating premixed flame
FPV	Flamelet/Progress variable
FTC	Full transport and chemistry

NOMENCLATURE

HRR	Heat Release Rate
LES	Large eddy simulation
LHV	Lower heating value
MA	Mixture-averaged
ODE	Ordinary differential equation
PCC	Pulverised coal combustion
PDF	Probability density function
PKP	Pyrolysis kinetic preprocessor
PLIF	Planar laser-induced fluorescence
PV	Progress variable
RANS	Reynolds-averaged Navier–Stokes
SDR	Scalar dissipation rate
SFOR	Single first order reaction
SMD	Sauter mean diameter
TCI	Turbulence-chemistry interaction
TNF	International workshop on measurement and computation of turbulent non-premixed flames
TRI	Turbulence-radiation interaction
ULF	Universal laminar flame solver (used in-house code)

GREEK SYMBOLS

<i>Symbol</i>	<i>Meaning</i>	<i>Unit</i>
α	Coal-to-oxidizer ratio	-
α_{cb}	Mass-ratio of consumed oxidant per converted carbon	-

NOMENCLATURE

α_k	Weighting factor for species k	-
χ	Scalar dissipation rate	$\frac{1}{s}$
$\dot{\omega}_c$	Reaction rate for progress variable	$\frac{kg}{sm^3}$
$\dot{\omega}_k$	Reaction rate for species k	$\frac{kg}{sm^3}$
$\dot{\omega}_T$	Heat release rate	$\frac{J}{sm^3}$
ϵ	Emissivity	-
γ_e	Chemical mode	$\frac{1}{s}$
λ_e	Eigenvalues of the chemical Jacobian matrix	$\frac{1}{s}$
μ	Dynamic viscosity	$\frac{kg}{ms}$
ϕ	Equivalence ratio	-
ρ	Density	$\frac{kg}{m^3}$
σ	Stefan-Boltzmann constant = $5.67 \times 10^{-8} \frac{J}{sm^2 K^4}$	$\frac{J}{sm^2 K^4}$
φ	Thermo-chemical state	-

LATIN SYMBOLS

<i>Symbol</i>	<i>Meaning</i>	<i>Unit</i>
\dot{m}	Mass flux	$\frac{kg}{s}$
\dot{q}	Heat flux	$\frac{J}{s}$
\dot{S}_ρ	Mass source term	$\frac{kg}{m^3 s}$
\dot{S}_T	Temperature source term	$\frac{J}{m^3 s}$
\dot{S}_u	Momentum source term	$\frac{kg}{m^3 s^2}$
\dot{S}_Y	Species source term	$\frac{kg}{m^3 s}$
\mathbf{J}_c	Jacobian matrix of chemical source terms	$\frac{1}{s}$
\mathcal{M}_k	Chemical symbol for species subscript k	-

NOMENCLATURE

\bar{M}	Mean molar mass of a mixture	$\frac{\text{kg}}{\text{kmol}}$
M_{flux}	Mass flow rate	$\frac{\text{kg}}{\text{m}^2 \text{ s}}$
A	Frequency factor	$\frac{1}{\text{s}}$
A_p	Particle surface area	m^2
c_p	Specific heat capacity	$\frac{\text{J}}{\text{kg K}}$
D	Diffusion coefficient	$\frac{\text{m}^2}{\text{s}}$
d_p	Particle diameter	m
E	Activation energy	$\frac{\text{J}}{\text{mol}}$
F	Drag force	$\frac{\text{kg m}}{\text{s}^2}$
h	Specific total enthalpy	$\frac{\text{J}}{\text{kg}}$
h_s	Specific sensible enthalpy	$\frac{\text{J}}{\text{kg}}$
h_t	Heat transfer coefficient	$\frac{\text{J}}{\text{s m}^2 \text{ K}}$
J	Pressure eigenvalue	$\frac{\text{kg}}{\text{m}^3 \text{ s}}$
k	Thermal conductivity	$\frac{\text{J}}{\text{s m K}}$
M	Molar mass	$\frac{\text{kg}}{\text{kmol}}$
m	Mass	kg
n_p	Particle number density	$\frac{1}{\text{m}^3}$
p	Pressure	$\frac{\text{kg}}{\text{m s}^2}$
R	Universal gas constant = $8.314 \frac{\text{J}}{\text{mol K}}$	$\frac{\text{J}}{\text{mol K}}$
r	Radial coordinate	m
s_l	Laminar burning velocity	$\frac{\text{m}}{\text{s}}$
T	Temperature	K
U	Relative radial velocity	$\frac{1}{\text{s}}$

NOMENCLATURE

u	Radial velocity	$\frac{\text{m}}{\text{s}}$
v	Axial velocity	$\frac{\text{m}}{\text{s}}$
X	Mole fraction	-
x	Axial coordinate	m
Y	Mass fraction	-
y_{vol}	Total volatile yield	$\frac{\text{kg}_{\text{vol}}}{\text{kg}_{\text{coal}}}$
Y_c	Progress variable	-
Z	Mixture fraction	-
z	Blowing factor	-
LHV	Specific lower heating value	$\frac{\text{J}}{\text{kg}}$
Sw	Swelling factor	-

SUBSCRIPTS

<i>Symbol</i>	<i>Meaning</i>
g	Gas
p	Particle
0	Initial state
C	Carbon
cb	Char burnout
char	Char
coal	Coal
conv	Convection
daf	Dry and ash free
ox	Oxidant

NOMENCLATURE

pyr	Pyrolysis
rad	Radiation
ref	Reference
st	Stoichiometric
vol	Volatiles
wall	Wall

 INTRODUCTION

In recent years, huge efforts have been made to replace fossil fuels by utilizing renewable resources such as wind, water, geothermal heat and sunlight. However, utilizing fossil fuels such as coal to produce power is still and will remain a dominant activity as visualised in Figure 1.1. The demand for energy is also increasing all over the world wide despite the new energy-saving technologies. The development of new technologies and the optimization of

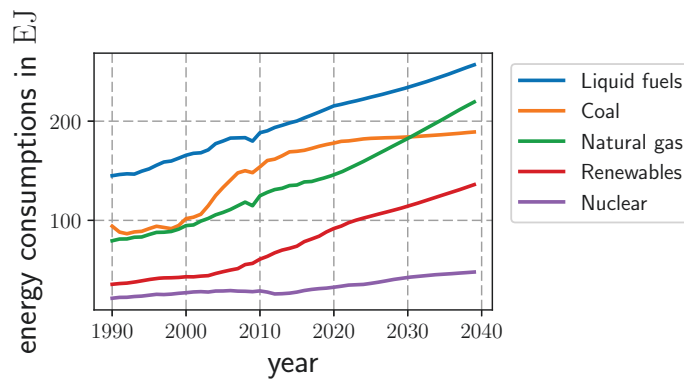


Figure 1.1.: Energy consumptions by source: facts and predictions [11].

existing ones requires a deeper understanding of physics behind them. The complex interplay of necessary models for pulverized coal combustion is given in Figure 1.2 and discussed hereafter. Tools are required to accurately predict the conversion of coal. For important steps for

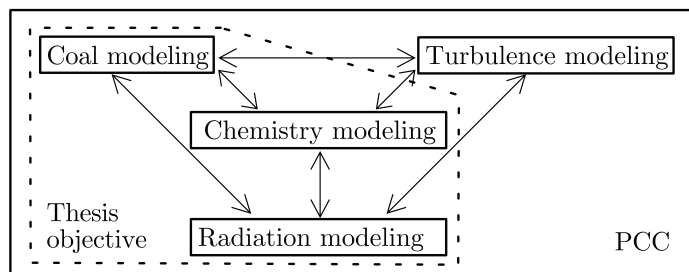


Figure 1.2.: Overview of selected submodels for PCC modeling. The dashed region marks the region of interest in this thesis.

conversion are drying, devolatilization and char burnout. The corresponding rates depend

INTRODUCTION

on the structure of coal, which is highly complex and consists of several modular units, nuclei, bridges and chains as illustrated in Figure 1.3. Predictive models for the coal conversion

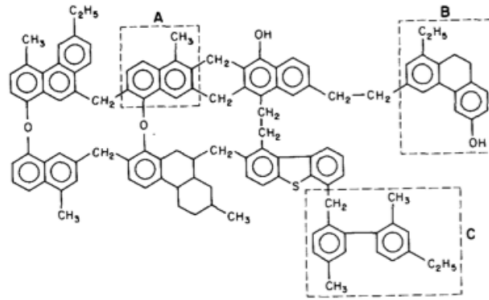


Figure 1.3.: Illustration of modular units, nuclei, bridges and chains in a coal molecule [12]. Unit A: aromatic nucleus, Unit B: partially hydrogenated nucleus, Unit C: biphenyl nucleus.

process dealing with these structural differences have been developed over recent decades. Detailed models for the devolatilization process are the Chemical Percolation Devolatilization (CPD) method [1], the combination of the functional group method and the depolymerization-vaporization-cross-linking (FG-DVC) method [2] and FLASHCHAIN [3]. For char burnout the Carbon Burnout Kinetics (CBK) models are usually utilized, version CBK/E being used for combustion [4] and CBK/G for gasification [18] are usually utilized. These models also consider pore diffusion, bulk diffusion and ash inhibition. Two aspects which are generally not considered are fragmentation during pyrolysis and catalytic effects of the ash. However, the methods' direct usage for computational fluid dynamic (CFD) reactor modeling is generally too computationally expensive. Following the strategy presented by Vascellari et al. [5], the results of advanced models are used to calibrate kinetic parameters of simplified models, which are valid only for certain conditions. This approach has been successfully applied by Vascellari et al. [19] to simulate the gasifier from Brigham Young University (BYU) [20] and in a comprehensive study by Stein et al. [21] on a laboratory-scale pulverised coal burner from the Central Research Institute of Electric Power Industry (CRIEPI) [22–24].

Laboratory- and industrial-scale reactors are usually driven by turbulent combustion, hence predictive turbulence modeling is also important for simulations. Different approaches exist with different degrees of resolution, as illustrated in Figure 1.4. Only the mean quantities are obtained for the Reynolds-averaged Navier–Stokes (RANS) approach, while the large eddy simulation (LES) approach resolves fluctuations bigger than a specified filter width. For direct numerical simulation (DNS), no turbulence model is necessary, because all spatial and temporal scales are resolved. The computational effort increases along with the resolution, therefore DNS is nowadays not applicable for laboratory-scale reactor simulations. The first pioneering work on LES for pulverized coal combustion (PCC) was performed with a relatively simple one-step chemistry approach by Kurose and Makino [25]. LES have become more and more popular for pulverized coal combustion in the last few years [21, 26–30]. Despite the signifi-

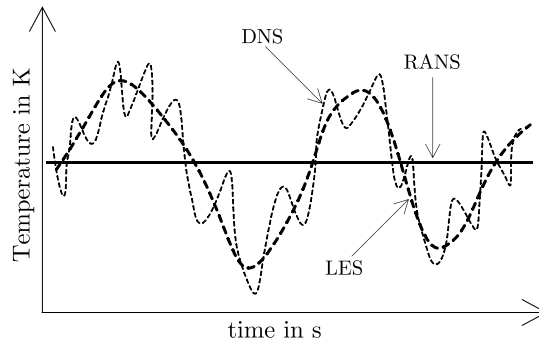


Figure 1.4.: Details on resolution quality for different turbulence modeling. Adapted from [13].

cantly improved description of the flow and mixing field, these studies usually approximate volatile matter with simplified approaches, neglecting the influence of large hydrocarbons, and use global reaction schemes to reduce computational costs.

However, to predict emissions of pollutants such as NO_x, soot or higher hydrocarbons, detailed reaction schemes are necessary. The regulations on pollutant emissions are becoming more and more stringent in order to slow down the green-house effect, so a lot of effort has been put into for clean coal technologies (CCTs). For gaseous combustion, a huge variety of models exist to account for turbulence-chemistry interaction (TCI) such as PDF methods [31], conditional moment closure [32], linear eddy modeling [33] and tabulation-based methods such as the laminar non-premixed flamelet [34], flamelet/progress variable (FPV) [6], flamelet generated manifold (FGM) [35] and the flame prolongation of intrinsic low-dimensional manifold (FPI) [36], which use only a few representative parameters to obtain the thermo-chemical state and other additional quantities, such as source terms or transport properties. Eaton et al. [37] presented a review paper on modeling strategies applied for coal combustion in 1999. Similar papers were published more recently by Chen et al. [38] and Edge et al. [26] on the oxy-fuel combustion of pulverized coal and by Tabet and Gökcalp [39] on co-firing of coal and biomass. Oxy-fuel combustion is a prominent candidate for carbon capture and storage (CCS) technologies and therefore for CCT.

The first applications of the FPV method for PCC were performed by Watanabe and Yamamoto [40] and Watanabe et al. [7]. To validate the proposed tabulation strategy for devolatilization and char burnout, a comparison was made between the detailed chemistry solution and the FPV solution [40]. The FPV method had problems in predicting the ignition distance to the nozzle. However, the general flame structure is similar. In [7] they enhanced their FPV method for turbulent combustion and drying of the coal. This method is compared against images of two experiments. There is still no detailed validation of the proposed method. Another unresolved issue is how to deal with the drop in enthalpy due to heat exchange between the gaseous phase and the dispersed phase. These points will be addressed in the thesis.

Several radiation models exist, differing significantly in their complexity and computational effort, even accounting for turbulence-radiation interaction (TRI) [41]. It was found that gaseous radiation can play a significant role [42, 43], especially if reabsorption occurs. However, particle radiation prevails over gas radiation [44], especially in PCC.

There are many coal experiments [23, 45–47] in the literature, but often not all boundary conditions are well defined for numerical modeling. Following the success story of the International Workshop on Measurement and Computation of Turbulent Non-premixed flames (TNF) [48] the Workshop on Measurement and Simulation of Coal and Biomass Conversion (CBC) [49] was recently found to improve the discussions between experimentalists and people performing simulations.

The objective of this work is to propose a predictive and computationally affordable method to model PCC and briefly analyse the sensitivity of this approach in well-defined laminar cases.

The thesis is structured as follows: Chapter 2 yields a overview on the models utilised for the coal conversion processes, followed by the general governing equation for reactive flow systems for the gaseous and solid dispersed phases. The detailed modeling of the two phases is called the fully coupled chemistry and transport (FTC) model. Section 2.3 covers the original Flamelet/Progress Variable (FPV) model and examines how to account for non-adiabatic effects in flamelet look-up tables (FLUT), which is important for flamelet modeling of coal flames. Finally, the FPV approach is proposed for the gas and coal phases.

The applications of the previously described models are given in Chapter 3, which is divided into three parts. The first, Section 3.1, deals with the purely numerical investigation of dry, devolatilizing coal particles in a counterflow and the applicability of a FLUT in that case. Section 3.2 covers the numerical results in a stagnation flow flame, which was experimentally investigated by Xia et al. [9]. Finally, in Section 3.3 the validation of the models is shown for a modified stagnation flame, accounting for both pyrolysis and char burnout.

Concluding remarks are given finally in Chapter 4.

All calculations in this thesis were carried out with the in-house solver ULF [50].

PHYSICAL MODEL FORMULATIONS

This work mainly highlights two models: the fully coupled transport and chemistry (FTC) model and the flamelet/progress variable (FPV) model. In both models, the flow field and coal particles are obtained by solving governing equations for mass, momentum and energy for each phase. In the FTC model, additional transport equations for each species are solved, whereas in the FPV model the chemical state is obtained from pre-calculated tables using a limited set of transported scalars.

This chapter is structured as follows: First the general coal conversion process will be discussed. The obtained models will be used for the FTC model for gaseous and solid phase. Section 2.3 introduces the basics of the FPV-model for gaseous phase. In order to apply the FPV model for coal and gas phase, the heat exchange between the phases has to be considered. Methods to deal with this non-adiabatic effect are afterwards presented. Finally, the FPV-model for the gas and solid phases is presented.

2.1 COAL MODELS

In general, the coal conversion process consists of several stages - drying, devolatilization, char burnout and ash inert heating - which may, but do not necessarily occur simultaneously. There are many subprocesses which occur during these stages, such as film and pore diffusion, pore evolution, intra-particle reaction and diffusion, thermal annealing or ash inhibition. Furthermore, coal is a fossil fuel and has different structures and rank. Coal is usually classified by proximate and ultimate analysis. The proximate analysis describes the fraction of major constituents - volatile matter, fixed carbon moisture and ash - while the ultimate analysis contains the elemental balance. The following ranks of coals are listed in decreasing volatile and increasing carbon content:

- lignite,
- sub-bituminous coal,
- bituminous coal,
- anthracite.

Based on the types of coal, several detailed models have been developed for coal pyrolysis, e.g. CPD [1], FG-DVC [2], FLASHCHAIN [3], and for char burnout, e.g. CBK/E [4] and

CBK/G [18], to deal with the structural differences when predicting the relevant subprocess during coal conversion. As the direct usage of these models in Computational Fluid Dynamics (CFD) is too computationally expensive, they are used to fit ordinary kinetic models [5, 19]. This procedure is also utilized here and will be described in the following sections.

2.1.1 Thermodynamic coal properties

The coal model introduced here highlights three components - dry-ash-free coal, char and ash - and does not include moisture. Their corresponding mass fractions $Y_{p,\text{coal}}$, $Y_{p,\text{char}}$ and $Y_{p,\text{ash}}$ describe the current stage of the thermal conversion process for coal. The sensible enthalpy and specific heat of the dry-ash-free coal components are modelled according to Merrick [51]

$$c_{p,\text{coal}}(T_p) = \left(\frac{R_g}{M_{\text{daf}}} \right) \left[g_1 \left(\frac{\theta_1}{T_p} \right) + 2g_1 \left(\frac{\theta_2}{T_p} \right) \right], \quad (2.1)$$

$$h_{s,\text{coal}}(T_p) = \left(\frac{R_g}{M_{\text{daf}}} \right) \left[\theta_1 \left(g_0 \left(\frac{\theta_1}{T_p} \right) - g_0 \left(\frac{\theta_1}{T_{\text{ref}}} \right) \right) \right. \quad (2.2)$$

$$\left. + 2\theta_2 \left(g_0 \left(\frac{\theta_2}{T_p} \right) - g_0 \left(\frac{\theta_2}{T_{\text{ref}}} \right) \right) \right], \quad (2.3)$$

where the functions g_0 and g_1 are defined as

$$g_0(z) = \frac{1}{e^z - 1}, \quad (2.4)$$

$$g_1(z) = \frac{z^2 e^z}{(e^z - 1)^2}, \quad (2.5)$$

and the characteristic temperatures θ_1 and θ_2 equal to 380 K and 1800 K, respectively. The definition of the mean molecular mass M_{daf} is given by

$$\frac{1}{M_{\text{daf}}} = \sum_{i=1}^{N_e} \frac{y_{i,\text{daf}}}{M_i}, \quad (2.6)$$

where $y_{i,\text{daf}}$ is the dry-ash-free mass fraction of the element i .

All thermodynamic properties of the char are provided from the graphite thermo object which is included in the Cantera chemistry software package [52].

The sensible enthalpy and the specific heat of the ash are modelled as

$$c_{p,\text{ash}}(T_p) = a_{0,\text{ash}} + a_{1,\text{ash}} T_p, \quad (2.7)$$

$$h_{s,\text{ash}}(T_p) = \int_{T_{\text{ref}}}^{T_p} c_{p,\text{ash}} dT_p = a_{0,\text{ash}} (T_p - T_{\text{ref}}) + \frac{a_{1,\text{ash}}}{2} (T_p^2 - T_{\text{ref}}^2), \quad (2.8)$$

where $a_{0,\text{ash}} = 754 \frac{\text{J}}{\text{kg K}}$ and $a_{1,\text{ash}} = 0.586 \frac{\text{J}}{\text{kg K}^2}$ [51].

The overall sensible enthalpy and specific heat of the coal particle are expressed as the mass-weighted sum of dry-ash-free coal, char and ash:

$$c_{p,p} = Y_{p,\text{coal}} c_{p,\text{coal}} + Y_{p,\text{char}} c_{p,\text{char}} + Y_{p,\text{ash}} c_{p,\text{ash}} , \quad (2.9)$$

$$h_{s,p} = Y_{p,\text{coal}} h_{s,\text{coal}} + Y_{p,\text{char}} h_{s,\text{char}} + Y_{p,\text{ash}} h_{s,\text{ash}} . \quad (2.10)$$

2.1.2 Thermo-chemical conversion of coal

The overall mass transfer from the coal particles to the gas phase is given by

$$\dot{m}_p = \dot{m}_{\text{vol}} + \dot{m}_{\text{char}} , \quad (2.11)$$

where the subscript “vol” denotes the mass-based devolatilization rate due to coal pyrolysis and the subscript “char” the consumption rate of char due to burnout. Devolatilization is represented by the mass-based balance equation

$$\text{dry coal} \rightarrow y_{\text{vol}} \text{ volatiles} + (1 - y_{\text{vol}}) \text{ char} . \quad (2.12)$$

The devolatilization rate of the coal particles is modeled by the Single First Order Reaction (SFOR) model [53]

$$\dot{m}_{\text{vol}} = m_p Y_{p,\text{coal}} y_{\text{vol}} A e^{(-E/RT_p)} , \quad (2.13)$$

where $Y_{p,\text{coal}}$ is the mass fraction of coal in the particle and y_{vol} is the total volatile yield per kg coal (daf). The kinetic constants A , E , the total volatile yield y_{vol} and the composition of the volatile matter are determined by the Pyrolysis Kinetic Preprocessor (PKP) [5]. Usually, the volatile composition varies during the devolatilization process and depends on the coal and the conditions (i.e. temperature, heating rate, etc.). However, the assumption of constant volatile matter is commonly used in numerical simulations of pulverized coal combustion [54–57] and this assumption is also made here. The volatile composition is defined using the method developed by Genetti [58], assuming C_6H_6 as tar.

To restore the energy balance of the lower heating values (LHVs) for (2.12) pyrolysis heat is introduced:

$$\Delta h_{\text{pyr}}(T_{\text{ref}}) = \frac{1}{y_{\text{vol}}} ((1 - y_{\text{vol}}) \text{LHV}_{\text{char}} + y_{\text{vol}} \text{LHV}_{\text{vol}} - \text{LHV}_{\text{coal}}) , \quad (2.14)$$

where the LHV of coal is calculated based on Dulong’s formula [59] and the reference temperature is $T_{\text{ref}} = 298.15 \text{ K}$. With this definition Δh_{pyr} is negative for an exothermic pyrolysis process and positive for an endothermic, and it is based on the mass rate of volatiles released.

To further account for the sensible enthalpies of coal, char and volatiles, the heat of pyrolysis is evaluated at the current particle temperature

$$\begin{aligned} \Delta h_{\text{pyr}}(T_p) = & \Delta h_{\text{pyr}}(T_{\text{ref}}) + \frac{1}{y_{\text{vol}}} \left[(1 - y_{\text{vol}}) (h_{\text{char}}(T_p) - h_{\text{char}}(T_{\text{ref}})) \right. \\ & \left. + y_{\text{vol}} \sum_{k=1}^{N_s} Y_{k,\text{vol}} (h_k(T_p) - h_k(T_{\text{ref}})) - (h_{\text{coal}}(T_p) - h_{\text{coal}}(T_{\text{ref}})) \right]. \end{aligned} \quad (2.15)$$

For the char conversion the heterogeneous reaction with oxygen to CO is considered:



The char burnout rate is described by the Baum and Street model [60]

$$\dot{m}_{\text{char}} = A_p p_{\text{ox}} \frac{D_0 \mathcal{R}}{D_0 + \mathcal{R}}, \quad (2.17)$$

which is a simple model accounting for the different combustion regimes for coal in air, namely diffusion and kinetic controlled regimes. In the above equation, A_p is the particle surface area, p_{ox} is the partial pressure of the oxidant species, D_0 the diffusion rate and \mathcal{R} the kinetic rate. The rates are given as

$$D_0 = C_1 \frac{([T_p + T_g]/2)^{0.75}}{d_p}, \quad (2.18)$$

$$\mathcal{R} = C_2 e^{-E/RT_p}, \quad (2.19)$$

where the corresponding model constants $C_1 = 5 \times 10^{-12}$, $C_2 = 0.002$ and $E = 7.9 \times 10^7$ are taken from [61].

The heat release of the char burnout Δh_{cb} is obtained by balancing the total enthalpies of char, O_2 and CO

$$\Delta h_{\text{cb}}(T_p) = \frac{M_{\text{CO}} h_{\text{CO}}(T_p) - \frac{1}{2} M_{\text{O}_2} h_{\text{O}_2}(T_p)}{M_{\text{C}}} - h_{\text{char}}(T_p) \quad (2.20)$$

Furthermore, particle swelling is coupled to the devolatilization progress by the empirical relation [60]

$$\frac{d_p}{d_{p,0}} = 1 + (\text{Sw} - 1) \frac{m_{\text{coal},0} - m_{\text{coal}}}{m_{\text{coal},0}}, \quad (2.21)$$

with the swelling coefficient Sw and $m_i = m_p Y_{p,i}$ for $i \in \{\text{coal}, \text{char}, \text{ash}\}$.

2.2 CONSERVATION EQUATIONS FOR LAMINAR REACTIVE FLOWS

This section deals with governing equations for the investigated strained flow flame configuration and is structured as follows: First the general three-dimensional equations and details on the diffusion modeling utilised are presented. These general equations are then transformed for strained one-dimensional flames. Finally the exchange with the dispersed phase is discussed. Throughout this section the Einstein Notation will be used.

2.2.1 Equations for gaseous phase

The conservation of mass, momentum, energy and species are given as follows:

$$\frac{\partial \rho_g}{\partial t} + \frac{\partial}{\partial x_i} (\rho_g u_{g,i}) = 0, \quad (2.22)$$

$$\frac{\partial}{\partial t} (\rho_g u_{g,j}) + \frac{\partial}{\partial x_i} (\rho_g u_{g,i} u_{g,j}) = -\frac{\partial p}{\partial x_i} + \frac{\partial \tau_{ij}}{\partial x_i} + \rho_g g_j, \quad (2.23)$$

$$\frac{\partial}{\partial t} (\rho_g h_g) + \frac{\partial}{\partial x_i} (\rho_g u_{g,i} h_g) = -\frac{\partial}{\partial x_i} \left(\sum_{k=1}^{N_s} h_{g,k} V_{k,i} \right) + \frac{\partial}{\partial x_i} \left(\lambda_g \frac{\partial T_g}{\partial x_i} \right) + \dot{Q}_R, \quad (2.24)$$

$$\frac{\partial}{\partial t} (\rho_g Y_k) + \frac{\partial}{\partial x_i} (\rho_g u_{g,i} Y_k) = -\frac{\partial V_{k,i}}{\partial x_i} + \dot{\omega}_k, \quad (2.25)$$

where ρ_g is the density, \mathbf{u}_g the velocity vector of the gas phase, p the pressure, \mathbf{g} the gravity force, h_g the total enthalpy of the gas, T_g the gas temperature, λ_g the thermal conductivity and Y_k the mass fraction of species k . The viscous tensor $\boldsymbol{\tau}$ is calculated for Newtonian fluids applying Stokes's law:

$$\tau_{ij} = -\frac{2}{3}\mu \frac{\partial u_k}{\partial x_k} \delta_{ij} + \mu \left(\frac{\partial u_i}{\partial x_j} + \frac{\partial u_j}{\partial x_i} \right). \quad (2.26)$$

There are several radiation models for the radiative source term \dot{Q}_R , which differ significantly in their complexity and computational effort. It was found that gaseous radiation can play a significant role [42], especially if reabsorption occurs. However, particle radiation prevails over gas radiation [44], therefore \dot{Q}_R will be neglected throughout this thesis, unless otherwise stated.

The definition of the laminar diffusion flux \mathbf{V}_k for the species k in general is given by

$$\mathbf{V}_k = \rho_g \mathbf{u}_k Y_k, \quad (2.27)$$

where the species diffusion flux \mathbf{u}_k is composed of a thermal $\mathbf{u}_{T,k}$, a diffusive $\mathbf{u}_{D,k}$ and a correction velocity \mathbf{u}_c

$$\mathbf{u}_k = \mathbf{u}_{D,k} + \mathbf{u}_{T,k} + \mathbf{u}_c. \quad (2.28)$$

In this work two approaches are used to calculate the diffusive species velocity $\mathbf{u}_{D,k}$:

$$u_{iD,k} = -\frac{D_{m,k}}{X_k} \frac{\partial X_k}{\partial x_i} \quad (\text{mixture-averaged}), \quad (2.29)$$

$$u_{iD,k} = -\frac{\lambda}{\rho c_p Y_k} \frac{\partial Y_k}{\partial x_i} \quad (\text{Le} = \text{Le}_k = 1), \quad (2.30)$$

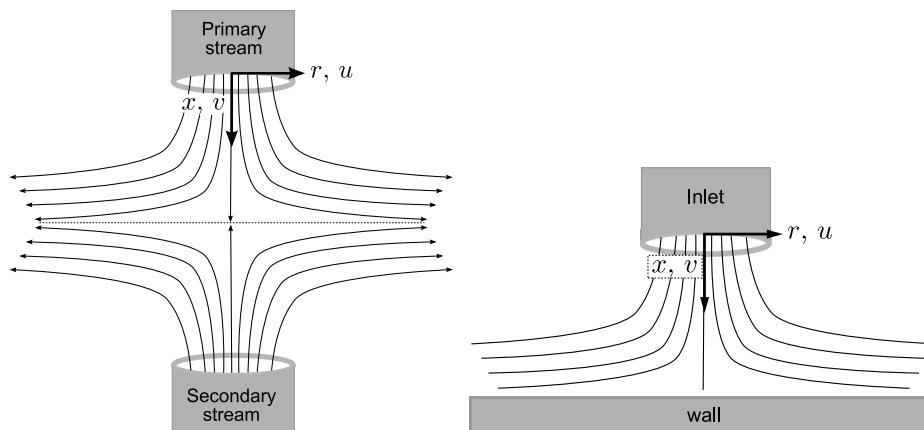
where $D_{m,k}$ is the pseudo-Fickian diffusion coefficient of species k into the mixture m by using the Hirschfelder and Curtis approximation [62]. The $Le = 1$ method assumes equal diffusivity of all species as well as the energy, whereas the mixture-averaged approach allows for individual mixing of the species. Another common approach is to substitute $D_{m,k}$ in Eq. (2.29) by the corresponding Lewis number

$$Le_k = \frac{\lambda}{\rho c_p D_{m,k}}. \quad (2.31)$$

The second term in Eq. (2.28) $\mathbf{u}_{T,k}$ describes the species diffusion caused by a temperature gradient. This Soret effect is neglected here. The sum of all diffusion fluxes has to be zero [63] otherwise the mass conservation is not fulfilled. Therefore, the correction velocity \mathbf{u}_c is introduced:

$$\mathbf{u}_c = -\rho_g \sum_{k=1}^{N_s} (\mathbf{u}_{D,k} + \mathbf{u}_{T,k}) Y_k. \quad (2.32)$$

The three-dimensional governing equations for reactive flows can be simplified for the stationary strained flow flames (Figure 2.1) investigated here. On the left-hand side the typical



(a) Schematic of a counterflow flame. (b) Schematic of stagnation flow flame.

Figure 2.1.: Schematics for the gaseous strained flow configurations investigated by [9, 14].

counterflow configuration is shown, where two counterflowing streams form a stagnation plane. The strained flow on the right-hand side is formed by introducing a stream at the inlet which then impinges with a wall.

Kee et al. [14] proposed a one-dimensional equation set for strained counterflow flames, by introducing a stream function which satisfies the continuity equation. Based on this stream function, the axial velocity v is then only a function of the axial coordinate x and the radial

velocity u varies linearly with the radius r , while $u = rU(x)$ holds. Based on these findings it is assumed that all other properties, such as the temperature and mass fractions, are also just functions of the coordinate x . Following these assumptions the general three-dimensional, equations reduce to the following set of one-dimensional equations

$$2\rho_g U_g + \frac{\partial \rho_g v_g}{\partial x} = 0, \quad (2.33)$$

$$\rho_g U_g^2 + \rho_g v_g \frac{\partial U_g}{\partial x} = \frac{\partial}{\partial x} \left(\mu_g \frac{\partial U_g}{\partial x} \right) + J, \quad (2.34)$$

$$\rho_g c_{p_g} v_g \frac{\partial T_g}{\partial x} = \frac{\partial}{\partial x} \left(k_g \frac{\partial T_g}{\partial x} \right) - \left(\sum_{k=1}^{N_s} \rho_g Y_k V_k c_{p,k} \right) \frac{\partial T_g}{\partial x} - \sum_{k=1}^{N_s} h_k \dot{\omega}_k, \quad (2.35)$$

$$\rho_g v_g \frac{\partial Y_k}{\partial x} = -\frac{\partial}{\partial x} (\rho_g Y_k V_{kx}) + \dot{\omega}_k, \quad (2.36)$$

where the subscript g denotes gas phase quantities and the eigenvalue $J = -\frac{1}{r} \frac{\partial p}{\partial x}$ fulfills the radial momentum conservation equation. This assumption can be proven by a similarity analysis as in Kee et al. [64].

2.2.2 Equations for dispersed solid phase

The conservation of mass, momentum, energy and number density for the disperse phase are given as follows:

$$\frac{\partial n_p m_p}{\partial t} + \frac{\partial}{\partial x_i} (n_p m_p u_{p,i}) = -\dot{m}_p, \quad (2.37)$$

$$\frac{\partial}{\partial t} (n_p m_p u_{p,j}) + \frac{\partial}{\partial x_i} (n_p m_p u_{p,i} u_{p,j}) = +n_p m_p f_j, \quad (2.38)$$

$$\frac{\partial}{\partial t} (n_p m_p h_p) + \frac{\partial}{\partial x_i} (n_p m_p u_{p,i} h_p) = -n_p (\dot{q} + \dot{m}_{\text{vol}} \Delta h_{\text{pyr}}(T_p) + \dot{m}_{\text{char}} \Delta h_{\text{cb}}(T_p)), \quad (2.39)$$

$$\frac{\partial n_p}{\partial t} + \frac{\partial}{\partial x_i} (n_p u_{p,i}) = 0, \quad (2.40)$$

$$(2.41)$$

where f_j are forces such as drag or gravity. The heat transfer \dot{q} by the particles can be broken down into the convective heat transfer \dot{q}_{conv} with the gas phase and the radiative heat transfer \dot{q}_{rad} to the surroundings

$$\dot{q}_{\text{conv}} = h_t A_p (T_p - T_g) \frac{z}{e^z - 1}, \quad (2.42)$$

$$\dot{q}_{\text{rad}} = \epsilon A_p \sigma (T_p^4 - T_s^4), \quad (2.43)$$

where A_p is the particle surface area, ϵ is the emissivity of coal particles (fixed at 0.85), σ is the Stefan-Boltzmann constant. The convective heat transfer coefficient is given by

$$h_t = \frac{\lambda_g \text{Nu}}{d_p}, \quad (2.44)$$

and the non-dimensional blowing factor z

$$z = \frac{c_{p,g}}{2\pi d_p \lambda_g} \dot{m}_p. \quad (2.45)$$

With the same assumptions as in Section 2.2.1, the stationary transport equations for the particles reduce to:

$$v_p \frac{\partial m_p}{\partial x} = -\dot{m}_p, \quad (2.46)$$

$$m_p U_p^2 + m_p v_p \frac{\partial U_p}{\partial x} = -\frac{F_r}{r}, \quad (2.47)$$

$$m_p v_p \frac{\partial v_p}{\partial x} = -F_x, \quad (2.48)$$

$$m_p v_p c_{p,p} \frac{\partial T_p}{\partial x} = -\dot{q}_{\text{conv}} - \dot{q}_{\text{rad}} - \dot{m}_{\text{vol}} \Delta h_{\text{pyr}}(T_p) - \dot{m}_{\text{char}} \Delta h_{\text{cb}}(T_p), \quad (2.49)$$

$$2n_p U_p + \frac{\partial n_p v_p}{\partial x} = 0, \quad (2.50)$$

where radial and axial components of the drag force are described with Stokes law:

$$F_x = 3\pi\mu_g d_p (v_p - v_g), \quad (2.51)$$

$$F_r = 3\pi\mu_g d_p (u_p - u_g). \quad (2.52)$$

2.2.3 Fully coupled Transport and Chemistry (FTC) model for gas and solid phase

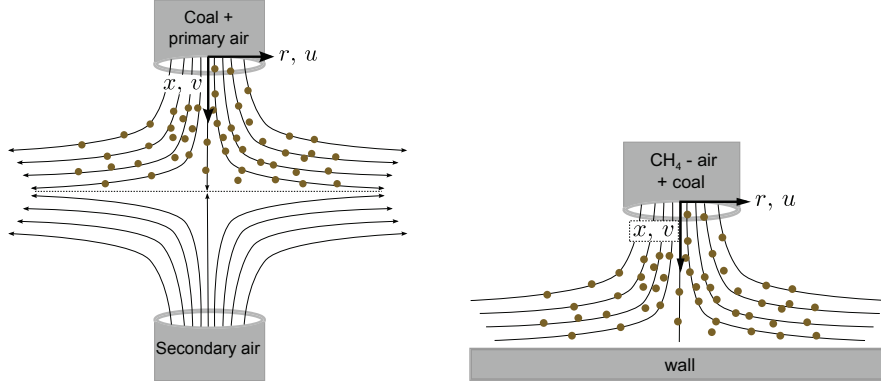
The investigated one dimensional flame configurations are shown in Figure 2.2, where the coal particles are introduced at the upper nozzle of the configurations. In order to accounting for the disperse coal particles, additional coupling terms \dot{S}_α are introduced in the stationary equation from Section 2.2.1 to ensure the conservation of mass, momentum and energy for both phases [8, 9, 65, 66]. These terms are marked in red in the following equations

$$2\rho_g U_g + \frac{\partial \rho_g v_g}{\partial x} = \dot{S}_\rho, \quad (2.53)$$

$$\rho_g U_g^2 + \rho_g v_g \frac{\partial U_g}{\partial x} = \frac{\partial}{\partial x} \left(\mu_g \frac{\partial U_g}{\partial x} \right) + J + \dot{S}_u, \quad (2.54)$$

$$\rho_g c_{p,g} v_g \frac{\partial T_g}{\partial x} = \frac{\partial}{\partial x} \left(k_g \frac{\partial T_g}{\partial x} \right) - \left(\sum_{k=1}^{N_s} \rho_g Y_k V_k c_{p,k} \right) \frac{\partial T_g}{\partial x} - \sum_{k=1}^{N_s} h_k \dot{\omega}_k + \dot{S}_T, \quad (2.55)$$

$$\rho_g v_g \frac{\partial Y_k}{\partial x} = -\frac{\partial}{\partial x} (\rho_g Y_k V_{kx}) + \dot{\omega}_k + \dot{S}_{Y,k}, \quad (2.56)$$



(a) Schematic of a counterflow flame with coal particles. (b) Schematic of stagnation flow flame with coal particles.

Figure 2.2.: Schematics for the particle loaded strained flow configurations investigated by [8, 9].

where the subscripts g and p denote gas phase quantities and particle quantities, respectively. The set of this equations ((2.53)-(2.56)) combined with set of equations for coal particles ((2.46)-(2.50)) is called the fully coupled transport and chemistry (FTC) model for gas and coal phase.

The source terms \dot{S}_α for the equations describing the gas phase read

$$\dot{S}_\rho = n_p \dot{m}_p, \quad (2.57)$$

$$\dot{S}_u = n_p \frac{F_r}{r} + n_p \dot{m}_p (U_p - U_g), \quad (2.58)$$

$$\dot{S}_T = n_p \dot{q}_{\text{conv}} + n_p \sum_{k=1}^{N_s} (\dot{m}_{\text{vol}} Y_{k,\text{vol}} + \dot{m}_{\text{char}} Y_{k,\text{cb}}) (h_k(T_p) - h_k(T_g)), \quad (2.59)$$

$$\dot{S}_{Y,k} = n_p (\dot{m}_{\text{vol}} (Y_{k,\text{vol}} - Y_k) + \dot{m}_{\text{char}} (Y_{k,\text{cb}} - Y_k)), \quad (2.60)$$

where the source terms \dot{m}_p , \dot{m}_{vol} and \dot{m}_{char} calculated according to the coal models previously defined in Section 2.1. The source terms \dot{S}_α couple the equations for the solid phase Eqs. 2.46-2.50 and the equations for the gas phase Eqs. 2.53-2.56. The mass fractions $Y_{k,\text{vol}}$ are the fixed volatile composition described in section 2.1.2, whereas $Y_{k,\text{cb}}$ is defined according to eq. (2.16)

$$Y_{k,\text{cb}} = \begin{cases} \frac{M_{\text{CO}}}{M_C}, & \text{for } k = \text{CO} \\ -0.5 \frac{M_{\text{O}_2}}{M_C}, & \text{for } k = \text{O}_2 \\ 0, & \text{else} \end{cases}. \quad (2.61)$$

The direct solution of the complete FTC model for coal is numerically not very robust. Therefore an iterative procedure suggested by Continillo and Sirignano [65] is applied here:

- (i) the gas phase is solved first with a damped, hybrid Newton solver
- (ii) then the solid phase is integrated with the pseudo particle residence time using the previously computed gas phase solution in the coupling terms.

Steps i and ii are repeated until user-defined tolerances are reached. A more detailed discussion on the solution procedure is given in Appendix A.1.

2.3 FLAMELET MODELING AND TABULATION STRATEGIES

The scope of this section is to introduce the general idea of flamelet modeling based on canonical premixed and non-premixed flame configurations. These will be applied to create tables for particle-loaded flames. This section starts with the introduction of flamelet models for non-premixed flames and premixed flames. Section 2.3.3 shows how to use the flamelet model and the canonical flame to create tables for gaseous flames. Due to the strong heat exchange between gas and coal particles enthalpy modeling has to be included in tables for coal. Different approaches to reach various enthalpy levels are presented in 2.3.5. And finally the Flamelet/Progress Variable (FPV) model for gas and coal is proposed.

2.3.1 Flamelet modeling for laminar non-premixed flames

The flamelet model for laminar non-premixed flames was originally developed by Peters [34] and is a widely used and heavily extended approach for combustion simulations [67–71]. The mixture fraction Z is one of the key parameters in flamelet modeling. Originally this parameter was introduced as the ratio of fuel mass flux and total mass flux:

$$Z = \frac{\dot{m}_{fuel}}{\dot{m}_{fuel} + \dot{m}_{ox}} \quad (2.62)$$

By definition, the mixture fraction becomes zero on the oxidizer side and one for pure fuel. A transport equation for the mixture fraction was derived [70] and reads:

$$\frac{\partial}{\partial t} (\rho_g Z) + \frac{\partial}{\partial x_i} (\rho_g u_{g,i} Z) = \frac{\partial}{\partial x_i} \left(\rho_g D_Z \frac{\partial Z}{\partial x_i} \right), \quad (2.63)$$

The connection between the well-known equivalence ratio ϕ and the mixture fraction Z is given by

$$\phi = \frac{Z}{1-Z} \frac{1-Z_{st}}{Z_{st}} \quad (2.64)$$

where Z_{st} is the mixture fraction at stoichiometry. Another key parameter is the progress variable (PV) Y_c , which is well-known from premixed flames. The definition applied here is the weighted sum of mass fractions

$$Y_c = \sum_{k=1}^{N_s} \alpha_k Y_k. \quad (2.65)$$

The transport equation for PV is derived by using the same weighting factors α_k and adding up the corresponding species transport equations (2.25)

$$\frac{\partial}{\partial t} (\rho_g Y_c) + \frac{\partial}{\partial x_i} (\rho_g u_{g,i} Y_c) = - \sum_{k=1}^{N_s} \alpha_k \frac{\partial V_{k,i}}{\partial x_i} + \underbrace{\sum_{k=1}^{N_s} \alpha_k \dot{\omega}_k}_{=:\dot{\omega}_c}. \quad (2.66)$$

Figure 2.3 shows a sketch of a typical non-premixed flame, where the fuel stream enters in the middle and oxidizer enters separately from the side. The classical non-premixed flamelet

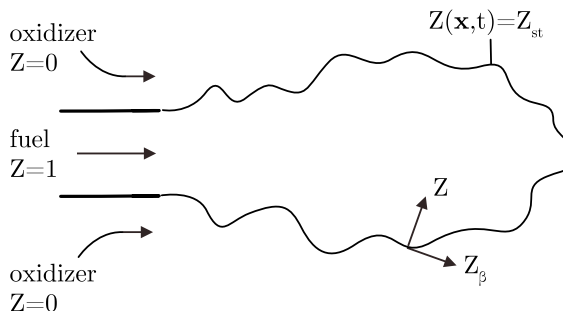


Figure 2.3.: Sketch of typical non-premixed flame.

model assumes the following:

- Reactive zone has smaller length scales (asymptotically) than surrounding mixture field
- Changes are mainly in orthogonal direction on iso-mixture fraction surfaces

Based on these assumptions, Equations (2.24)-(2.25) are transformed from physical space to mixture fraction space. Therefore, a coordinate transformation from the Euclidean system (t, x_1, x_2, x_3) to a local system (τ, Z, Z_2, Z_3) , which is perpendicular to the stoichiometric mixture surface (see Figure 2.3), is outlined in Appendix A.2 for the $Le = 1$ approach. The obtained flamelet equation for $Le = 1$ reads:

$$\rho_g \frac{\partial h_g}{\partial \tau} = \frac{\rho_g \chi}{2} \frac{\partial^2 h_g}{\partial Z^2} + \dot{Q}_R, \quad (2.67)$$

$$\rho_g \frac{\partial Y_k}{\partial \tau} = \frac{\rho_g \chi}{2} \frac{\partial^2 Y_k}{\partial Z^2} + \dot{\omega}_k, \quad (2.68)$$

$$(2.69)$$

where χ is the scalar dissipation rate (SDR) defined by

$$\chi = 2D_Z \frac{\partial Z}{\partial x_i} \frac{\partial Z}{\partial x_i}. \quad (2.70)$$

The SDR χ could be interpreted as an inverse mixing time and links the flow field with the mixing field. Flamelet equations are also available for variable Lewis numbers [70, 72] and were recently extended to include tangential diffusion effects on the iso-mixture fraction

surfaces [73]. However, in the remainder of this thesis, only $Le = 1$ flamelet equations are investigated.

The flamelet equation can be solved online [74], but a advantage in computational performance can be achieved by pre-tabulating over the SDR profile $\chi(Z)$. In order to specify $\chi(Z)$, a presumed function $f(Z)$ is used and the value $\chi_{st} = \chi(Z_{st})$ for the SDR at stoichiometry is selected

$$\chi = \chi_{st} \frac{f(Z)}{f(Z_{st})}. \quad (2.71)$$

For one-dimensional mixing layers, an analytical expression for $f(Z)$ was derived by [72]

$$f(Z) = \exp\left(-2\left(\operatorname{erfc}^{-1}(2Z)\right)\right). \quad (2.72)$$

The thermo-chemical state φ depends only on the mixture fraction Z and stoichiometric SDR χ_{st}

$$\varphi = \varphi(Z, \chi_{st}). \quad (2.73)$$

2.3.2 Flamelet modeling for laminar premixed flames

In line with Section 2.3.1 equations [75] exist to simulate premixed flames directly in composition space; however, this is not very common due to stability issues. This work focusses on a physical space solution for tabulation strategies based on premixed flame structures, which can be transformed into composition space using Eq. (2.65) afterwards. Beside the strained flames introduced in Section 2.2.1 other classes of canonical flames are freely propagating (FP) and burner-stabilized (BS) flames. A typical appearance of these premixed flames is shown in Figure 2.4. In addition to Eqs. (2.35) and (2.36), an Equation (2.74) for the mass

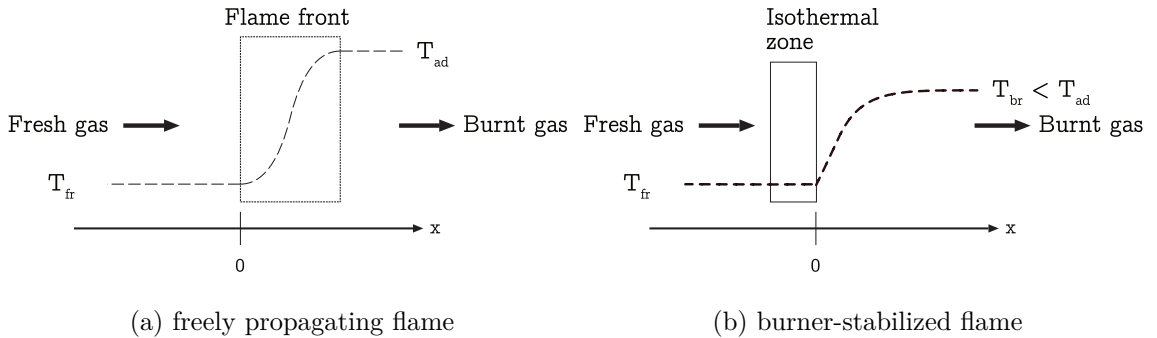


Figure 2.4.: Sketch of canonical premixed flames.

flux M_{flux} is solved for the FP flames. For the sake of completeness, the equations reads:

$$M_{flux} = \rho v_g = const, \quad (2.74)$$

$$\rho_g c_{p_g} v_g \frac{\partial T_g}{\partial x} = \frac{\partial}{\partial x} \left(k_g \frac{\partial T_g}{\partial x} \right) - \left(\sum_{k=1}^{N_s} \rho_g Y_k V_k c_{p,k} \right) \frac{\partial T_g}{\partial x} - \sum_{k=1}^{N_s} h_k \dot{\omega}_k, \quad (2.75)$$

$$\rho_g v_g \frac{\partial Y_k}{\partial x} = - \frac{\partial}{\partial x} (\rho_g Y_k V_{kx}) + \dot{\omega}_k. \quad (2.76)$$

The numerical results of a freely propagating flame are usually generated keeping the flame front on a particular point and fixing the temperature at that point. From the obtained mass flux M_{flux} and the fresh gas density $\rho_{g,fr}$, the laminar burning velocity s_l is evaluated:

$$s_l = \frac{M_{flux}}{\rho_{g,fr}}. \quad (2.77)$$

In conclusion, the state φ of a freely propagating flame depends on the mixture fraction Z and the physical coordinate x

$$\varphi_{FP} = \varphi_{FP}(Z, x). \quad (2.78)$$

The main difference between burner-stabilized flames and freely propagating flames is that the flow rate M_{flux} is no longer an unknown value of the system, but a parameter¹. For the burner-stabilized flame (Fig. 2.4b), first an isothermal zone is introduced and a velocity smaller than s_l is prescribed. Within this isothermal zone, a reduction in enthalpy takes place, which will be discussed in detail in Section 2.3.5. The corresponding thermo-chemical state φ of a burner-stabilized flame is determined by Z , x and the selected M_{flux}

$$\varphi_{BS} = \varphi_{BS}(Z, x, M_{flux}). \quad (2.79)$$

It is important to emphasize, that for the state φ_{BS} of a BS flame with $M_{flux} = s_l \rho_g$ the following holds

$$\varphi_{BS}(Z, x, M_{flux} = s_l \rho_g) = \varphi_{FP}(Z, x). \quad (2.80)$$

2.3.3 Flamelet tabulation and coupling strategies

This section addresses the procedure to create tables, based on the solutions obtained in Sections 2.3.1 and 2.3.2. There are several reasons for tabulating the thermo-chemical state φ , such as:

- Reduction in number of transport equations,
- Reduction of stiffness in the system,
- Accounting for Turbulence Chemistry Interaction (TCI)[6, 76].

¹ Eq. (2.74) for M_{flux} is not solved for a burner-stabilized flame.

Typical flamelet table parameters for gaseous flame applications are based on the mixture fraction Z and the progress variable Y_c [6]. By definition, the limits of Z are between zero and one, while the limits of PV $Y_{c,min}$ and $Y_{c,max}$ depends on the corresponding mixture as visualised in Figure 2.5. In order to avoid invalid data in the tables, it is necessary to span

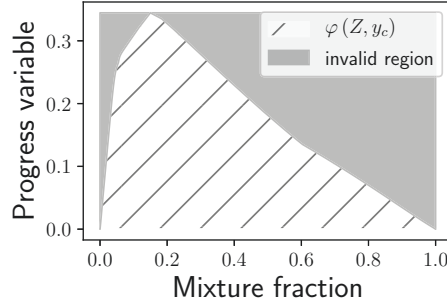


Figure 2.5.: The hatched region shows the valid states $\varphi(Z, Y_c)$ for a methane-air mixture with an initial temperature of 300 K. The grey region contains no valid solutions. The PV is defined as $Y_c := Y_{CO} + Y_{CO_2} + Y_{H_2} + Y_{H_2O}$.

the tables for Z and the normalized progress variable C

$$C = \frac{Y_c - Y_{c,min}}{Y_{c,max} - Y_{c,min}}, \quad (2.81)$$

to obtain a regular parameter set. The established way to request such pre-calculated tables is to solve transport equations for Z and Y_c and use these values to retrieve the thermo-chemical state φ by performing multi-dimension interpolation during the runtime (see Figure 2.6). This flexible framework allows for more state variables such as enthalpy or additional mixture

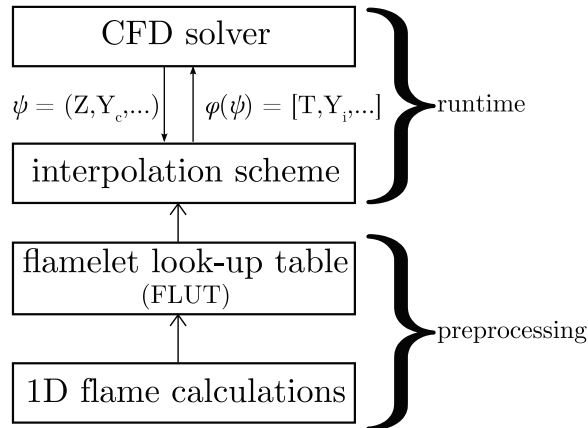


Figure 2.6.: Workflow of look-up properties from FLUT. Adapted from [15]

fractions, also for further solution variables such as thermo-physical and transport properties, and was successfully applied to model laminar and turbulent flames [43, 77–79]. FLUTs have grown exponentially in size with the number of input parameters, whereas the available memory per core in high-performance computing has fallen over recent years [80]. In order to

use high-dimensional tables the memory management methods developed by Weise et al. [80, 81] are directly integrated into the the workflow described above. In addition, a polynomial representation of the FLUT [15] offering additional runtime benefits is also selectable.

In order to retrieve the thermo-chemical state φ from such a table for Z and Y_c , the values $Y_{c,min}(Z)$ and $Y_{c,max}(Z)$ also have to be tabulated. For the first look-up, a value has to be assumed for C , which is then corrected for the second look-up as shown in Eq. (2.81) by taking the extrema of PV for the current Z from the first look-up.

The generation of such tables depends on the underlying canonical setups. A so called flamelet look-up table (FLUT) based on premixed flames is called a PFLUT, whereas a DFLUT is based on diffusion flames. The next two sections will provide details on the creation of a DFLUT and PFLUT respectively.

Tabulation strategy for a DFLUT

The steady-state solution of the flamelet equations contains the thermo-chemical state φ for the entire Z space at fixed χ_{st} with the presumed function f from Eq. 2.72. For a self-ignitable mixture the so-called S-shaped curve (Fig. 2.7a) can be obtained with the variation of χ_{st} . This curve describes the influence of SDR on the steady flamelet solution and shows the

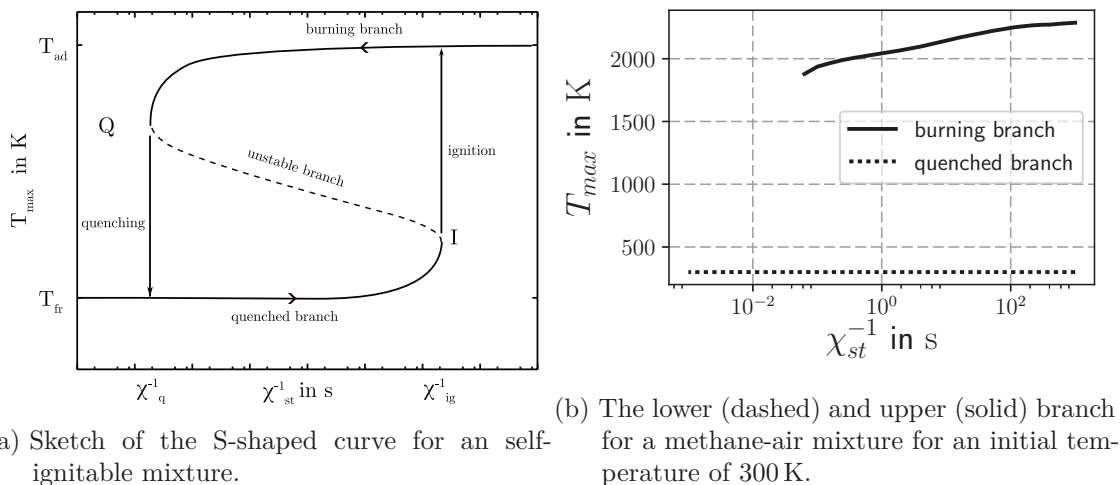


Figure 2.7.: The S-shaped curve is obtained by plotting the maximum temperature T_{max} over the inverse of the SDR in logarithmic scale of the abscissa.

interplay of reaction progress and diffusion effects. The upper part of the curve beginning at the non-strained burning solution ($\chi = 0$) and ending at the quenching SDR χ_q is called the burning branch. The lower branch starting from a quenched solution ($\chi > \chi_q$) and ending at the ignition SDR (χ_{ig}) is known as the quenched branch, where diffusion effects are stronger than reaction progress. The dashed line contains unstable solutions. Therefore, it is denoted as unstable branch. In Fig. 2.7b the burning branch for a stoichiometric methane-air mixture with an initial temperature of 300 K is shown as a solid line. Self-ignition does not occur in this mixture in the SDR range considered, thus the lower branch is a flat line (dashed line Fig. 2.7b).

The problem of tabulating φ as a function of Z and χ_{st} is to obtain the value for the stoichiometric SDR for all positions in the flame configuration considered. At an arbitrary position, Z and $\chi(Z)$ are available, while the SDR is based on the gradient of Z , so a high-resolution in space is needed. For the current flame configuration, using a presumed function f to calculate χ_{st} can be very error-prone [82]. Thus it was suggested by Pierce and Moin [6] to use the PV as an independent variable

$$\varphi(Z, \chi_{st}) \mapsto \varphi(Z, Y_c). \quad (2.82)$$

Figure 2.8 shows different PV profiles obtained with Eq. (2.65) in mixture fraction space on the left and as a function of stoichiometric SDR on the right for a methane-air mixture. The

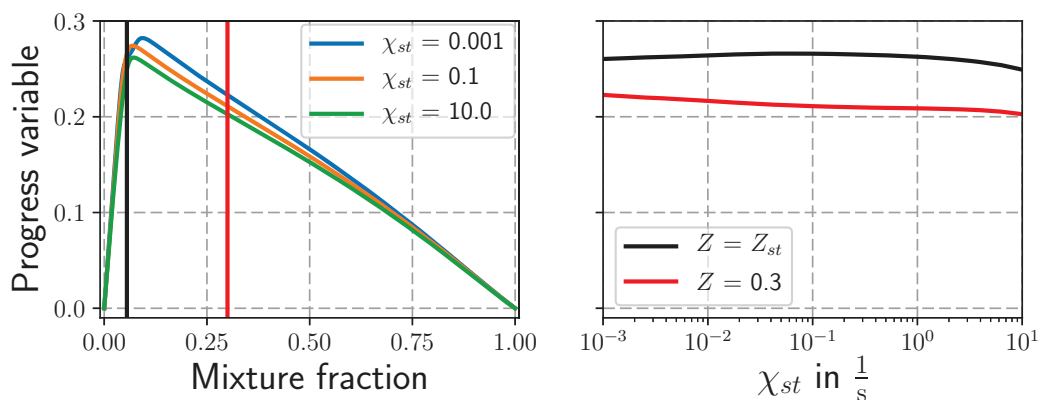


Figure 2.8.: Selected curves of a DFLUT for a methane-air mixture for an initial temperature of 300 K. The PV is defined as $Y_c := Y_{CO} + Y_{CO_2} + Y_{H_2} + Y_{H_2O}$. Left: PV profiles for three selected χ_{st} over Z , right: PV profiles for two selected Z over χ_{st} .

principal concept of mapping (2.82) is to switch the axis in the right-hand plot of Fig. 2.8. Problems could occur if this mapping is not injective², therefore different approaches [83, 84] were presented to optimize the weighting factors α_k in Eq. 2.65 to ensure a proper mapping. The Y_c profile for $Z = Z_{st}$ on the right-hand side of Fig. 2.8 is an example of a non-injective mapping. However, the affected thermo-chemical states are almost equal here.

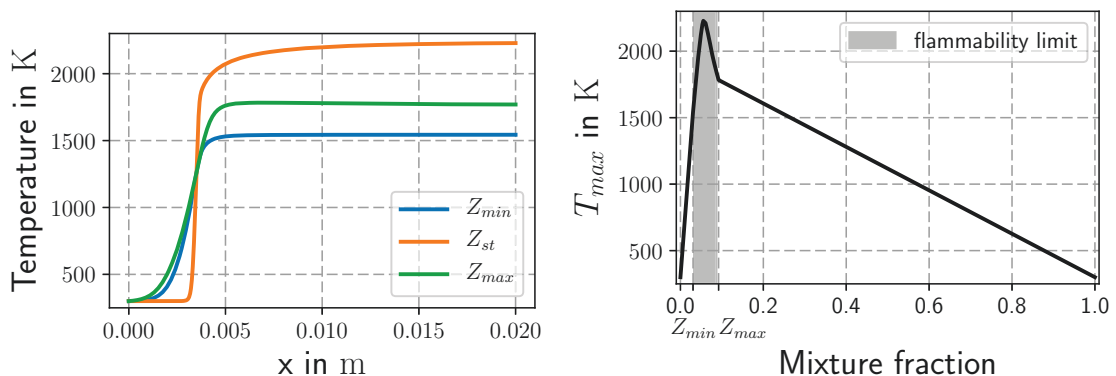
The procedure presented in this section is known as the Flamelet/Progress Variable (FPV) method.

Tabulation strategy for a PFLUT

Throughout this thesis an adiabatic PFLUT is created based on FP flames (Sec. 2.3.2). By specifying a different equivalence ratio ϕ or mixture fraction Z^3 , different thermo-chemical states φ are reached. An important issue for FP flames is the flammability limit, bounded by Z_{min} and Z_{max} , shown for a stoichiometric methane-air mixture with a fresh gas temperature of 300 K in Fig. 2.9b. Outside of the flammability region no flame can be established, so a

² A function $f : X \mapsto Y$ is called injective, if the following holds: $\forall a, b \in X, f(a) = f(b) \Rightarrow a = b$.

³ Z and ϕ are directly linked by Eq. (2.64)



(a) Temperature profiles in physical space for Z_{min} , Z_{st} , Z_{max} . (b) Profile of maximum temperature in composition space gained from the table.

Figure 2.9.: Flammability limits [Z_{min} , Z_{max}] for a stoichiometric premixed methane-air flame with $T_{fr} = 300$ K.

linear interpolation of the thermo-chemical state is performed between the nearest burning solution and pure fuel or oxidizer conditions, respectively, inside the table. In line with the FPV approach, a mapping from the axial coordinate x to the PV Y_c , again using Equation (2.65), is carried out in this work.

$$\varphi(Z, x) \xrightarrow{(2.65)} \varphi(Z, Y_c). \quad (2.83)$$

Similar approaches for building PFLUTs are the FGM [35] or the FPI method [36].

2.3.4 Flamelet tabulation for turbulent flames

This part is a short excursion on turbulent flamelet modeling and provides some indications on how to enhance laminar flamelet look-up tables for the modeling of turbulent flames.

The thermo-chemical state φ is not longer resolved in a turbulent simulation. For a large eddy simulation (LES), the state is decomposed into a resolved Favre-averaged state $\tilde{\varphi}$ and an unresolved residual state φ''

$$\varphi(\mathbf{x}, t) = \tilde{\varphi}(\mathbf{x}, t) + \varphi''(\mathbf{x}, t) \quad (2.84)$$

The FPV model for turbulent gaseous flames proposed by Pierce and Moin [6] provides equations for the filtered mixture fraction \tilde{Z} , the filtered progress variable \tilde{Y}_c and the subgrid variance of mixture fraction \tilde{Z}''^2 . The laminar state $\varphi(Z, C)$ has to be filtered to obtain $\tilde{\varphi}$

$$\tilde{\varphi} = \int \int \varphi(Z, C) \tilde{P}(Z, C) dZ dC, \quad (2.85)$$

where $\tilde{P}(Z, C)$ is the joint-PDF of Z and C . Assuming that these parameters are statistically independent allows the joint PDF to be separated into two independent PDFs

$$\tilde{P}(Z, C) = \tilde{P}(Z)\tilde{P}(C). \quad (2.86)$$

Filtering (Eq. (2.85)) is performed by applying a presumed β -PDF for Z and a δ -PDF for C [6]. The β -distribution for Z is given as

$$\tilde{P}(Z; \tilde{Z}, \widetilde{Z''^2}) = \frac{\Gamma(\beta_1 + \beta_2)}{\Gamma(\beta_1)\Gamma(\beta_2)} Z^{\beta_1-1} (1-Z)^{\beta_2-1}, \quad (2.87)$$

where

$$\beta_1 = \tilde{Z} \left[\frac{\tilde{Z}(1-\tilde{Z})}{\widetilde{Z''^2}} - 1 \right], \quad (2.88)$$

$$\beta_2 = (1-\tilde{Z}) \left[\frac{\tilde{Z}(1-\tilde{Z})}{\widetilde{Z''^2}} - 1 \right] \quad (2.89)$$

and Γ denotes the gamma function

$$\Gamma(\beta) = \int_0^\infty x^{\beta-1} e^{-x} dx \quad (2.90)$$

Filtering can be performed in advance and the filtered quantities can be stored in FLUTs. The filtered thermo-chemical state is represented by

$$\tilde{\varphi} = \tilde{\varphi}(\tilde{Z}, \widetilde{Z''^2}, \tilde{C}). \quad (2.91)$$

2.3.5 Non-adiabatic flamelet look-up tables

This section addresses how to include different enthalpy levels in a FLUT. The necessity of including various enthalpy levels in the tables for coal applications is due to enormous heat exchange between coal particles and gaseous phase and requires an additional parameter in the tables.

The enthalpy defect Δh represents the difference between the actual enthalpy and the enthalpy of an adiabatic flame, see e.g. [67, 85, 86]

$$\Delta h_g = h_g - h_{g,ad}. \quad (2.92)$$

Beside gaseous radiation, an other typical source of an enthalpy defect is the heat exchange with the disperse phase.

An easy way to cover heat losses is just to decrease temperatures of the reactants. When reaching enthalpy levels of real flames, unphysical boundary temperatures (below 270 K) could occur. Methods of avoiding unphysical boundary conditions for non-adiabatic flames will be

presented for premixed and non-premixed flames below. Finally, there is a discussion of how to create and assess the table.

Enthalpy defect modeling in non-premixed flames

The non-premixed flamelet equations can be solved in a Lagrangian or an Eulerian way. For the Lagrangian flamelet approach [87, 88], heat losses are obtained by transient calculation. The choice of the Lagrangian time could drastically influence the total heat loss. Estimating of the Lagrangian time is not straightforward, so the Eulerian approach is used in this work. In the following, only methods dealing with enthalpy defects within Eulerian flamelet approaches are described.

ENTHALPY SHIFT IN STEADY LAMINAR FLAMELETS In this approach, the flamelet equations are solved without an additional sink term in the energy equation. Instead, a shift of enthalpy at the boundaries is applied to cover the enthalpy defect. For the simulation it is common to specify the temperature instead of the enthalpy, so the temperature drop ΔT is calculated from the enthalpy shift Δh_g

$$\Delta T = \frac{\Delta h_g}{c_{p,g}}. \quad (2.93)$$

In order to avoid unrealistic low temperatures at $Z = 0$ and $Z = 1$, the mixture fraction range covered can be reduced as proposed by Hossain et al. [67]. The basic idea is to take an adiabatic solution ($\Delta h_g = 0$) and calculate a temperature profile according to Eq. (2.93). The new mixture fraction range $[Z_{\min}, Z_{\max}]$ is then obtained from the intersection of this temperature profile and the Z axis. Figure 2.10 gives a brief idea of this procedure. The

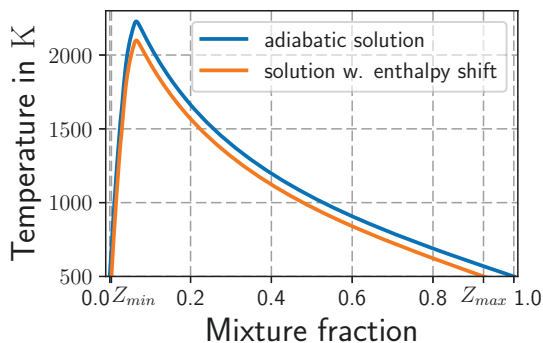


Figure 2.10.: Results of flamelet profiles for temperature showing solutions for an adiabatic flamelet and a flamelet with constant enthalpy shift over mixture fraction range.

composition at Z_{\min} and Z_{\max} are taken from corresponding points of the adiabatic solution. Hossain et al. [67] showed that relatively small errors are introduced.

A flamelet solution is obtained for each selected enthalpy defect Δh_g and stoichiometric SDR χ_{st} . By varying the two parameters, table for the thermo-chemical state φ can be

produced. In line with the discussions in Section 2.3.3, a mapping based on Equations (2.65) and (2.92) is performed for this method

$$\varphi(Z, \chi_{st}, \Delta h_g) \xrightarrow[(2.92)]{(2.65)} \varphi(Z, Y_c, h_g) \quad (2.94)$$

ENTHALPY REDUCTION WITH UNSTEADY LAMINAR FLAMELETS For this procedure an adiabatic steady flamelet solution is used to initialise a transient flamelet calculation. The energy equation is therefore solved with an additional source term such as the radiation source term \dot{Q}_R . The outcome of this method is a time-varying enthalpy defect which is distributed differently over the calculation domain. A typical example of this approach is visualised in Fig. 2.11. This method was already successfully applied by Ihme and Pitsch [89] in a LES simulation of the turbulent methane/air jet flame Sandia D [90]. The state φ in

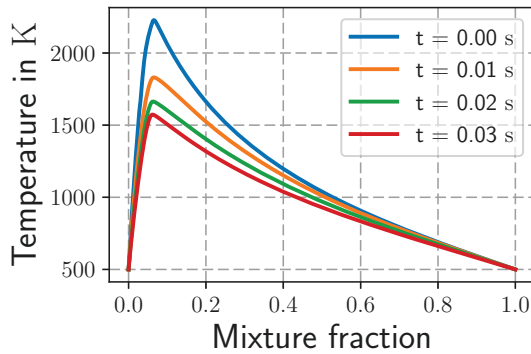


Figure 2.11.: Results of transient flamelet profiles for temperature at different times obtained for an stoichiometric methane-air mixture.

this method is characterised by the time t and stoichiometric SDR χ_{st} . For each time t an enthalpy profile $h_g(Z, \chi_{st}, t)$ is obtained. This profile and Eq. (2.65) are used for the following mapping

$$\varphi(Z, \chi_{st}, t) \xrightarrow{(2.65)} \varphi(Z, Y_c, h_g) \quad (2.95)$$

FACTORIZED TEMPERATURE SOURCE TERM IN STEADY LAMINAR FLAMELETS

The idea of this method, proposed by Rieth [91], is to take the Heat Release Rate (HRR) $\dot{\omega}_T$ as in Eq. (A.39), multiply it with a chosen parameter $\alpha \in [0, 1]$ and solve the steady flamelet equations. Equation (2.96) shows the modified transport equation for the temperature.

$$\rho_g c_{p_g} \frac{\partial T_g}{\partial \tau} = \rho_g c_{p_g} \frac{\chi}{2} \frac{\partial^2 T_g}{\partial Z^2} - \alpha \dot{\omega}_T. \quad (2.96)$$

Stoichiometric methane-air mixture results for different choices of α are shown in Figure 2.12 by way of example. The adiabatic solution is obtained for $\alpha = 1$, whereas pure mixing occurs for $\alpha = 0$, since the HRR is neglected.

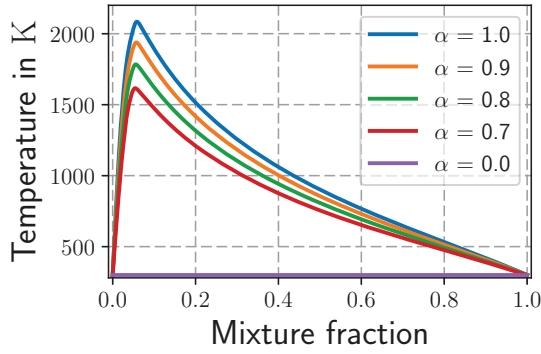


Figure 2.12.: Results of steady flamelet profiles for temperature at different values of the scaling factor α .

As in the previous method, there is a connection between α and the h_g -profile, so the mapping reads

$$\varphi(Z, \chi_{st}, \alpha) \xrightarrow{(2.65)} \varphi(Z, Y_c, h_g) \quad (2.97)$$

It is important to emphasize that this method can be used, whenever the temperature equation is solved.

In conclusion, three methods are proposed to include non-adiabatic effects in DFLUTs. The obtained thermo-chemical states $\varphi(Z, Y_c, h_g)$ are similar for the methods. Throughout this work the enthalpy shift method is used.

Enthalpy defect modeling in premixed flames

As already discussed in Section 2.3.2 the simulations used to generate a PFLUT are performed in physical space. The candidates considered for this generation are the freely propagating flames and the burner-stabilized flames introduced in Section 2.3.2.

In order to understand the enthalpy loss of a burner-stabilized flame, the explanation from Fiorina et al. [17] is adapted in this section. For simplicity, the $Le_k = 1$ assumption for all species k is used, but the discussion on the heat loss is also valid for mixture-averaged diffusion modeling. In Figure 2.13, h_{fr} denotes the enthalpy of the fresh mixture, $h(x = 0)$ the enthalpy of the gases after the isothermal zone and h_{br} the enthalpy of the burnt gases. The heat flux occurs at the end of the isothermal zone, therefore for $Le = 1$ holds

$$h(x) = h_{br} = h(x = 0), \text{ for } x \geq 0. \quad (2.98)$$

At the same position ($x = 0$) a conductive heat transfer \dot{Q} is assumed

$$\dot{Q} = -\lambda \left. \frac{\partial T}{\partial x} \right|_{x=0}. \quad (2.99)$$

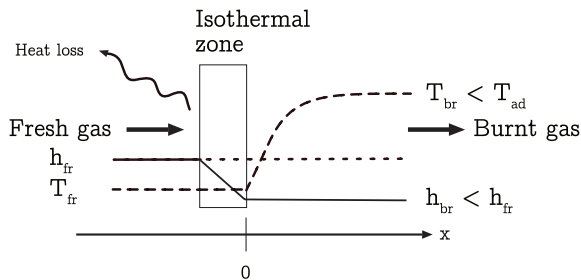


Figure 2.13.: Detailed sketch of a burner-stabilized flame.

Within the isothermal zone the heat flux \dot{Q} is exchanged with the surroundings

$$\dot{Q} = M_{flux} (h(x=0) - h_{fr}) . \quad (2.100)$$

The new enthalpy level $h(x=0)$ can be obtained from

$$h(x=0) = h_{br} = h_{fr} - \frac{\lambda}{M_{flux}} \left. \frac{\partial T}{\partial x} \right|_{x=0} . \quad (2.101)$$

By decreasing M_{flux} the enthalpy $h(x=0)$ decreases until the flame is extinguished.

To verify that two premixed flames with the same enthalpy level have the same flame structure, the example given by Fiorina et al. [17] is reproduced here. The boundary conditions for the freely propagating flame and the burner-stabilized flame are listed in Tab. 2.1. The

Table 2.1.: Boundary conditions of premixed stoichiometric methane-air flames [17].

flame type	T in K	h_{fr} in $\frac{\text{J}}{\text{kg}}$	$h(x=0)$ in $\frac{\text{J}}{\text{kg}}$
FP	600	8.2×10^4	8.2×10^4
BS	1000	5.8×10^5	

mass flow rate is adjusted to reach the same enthalpy level after the isothermal zone as in the freely propagating flame. Both flames are stoichiometric premixed laminar methane/air flames and the corresponding results are given in Figure 2.14. The temperature profiles on the left-hand side of Figure 2.14 (solid line for the freely propagating flame and circles for the burner-stabilized flame) show different trends over the physical coordinate x , as was to be expected. The profiles plotted in composition space can be found on the right-hand side of Fig. 2.14, where PV Y_c is selected to be the mass fraction of CO_2 ($Y_c = Y_{\text{CO}_2}$). The temperature and the species profiles⁴ are in very good agreement. This verifies that for the same enthalpy levels, the flame structure is not affected by the flame type and so both burner-stabilized and freely propagating flames can be used to generate a PFLUT. Furthermore, the enthalpy defect can be included in a PFLUT and used to reproduce any type of heat losses.

⁴ Y_{OH} chosen as in [17]

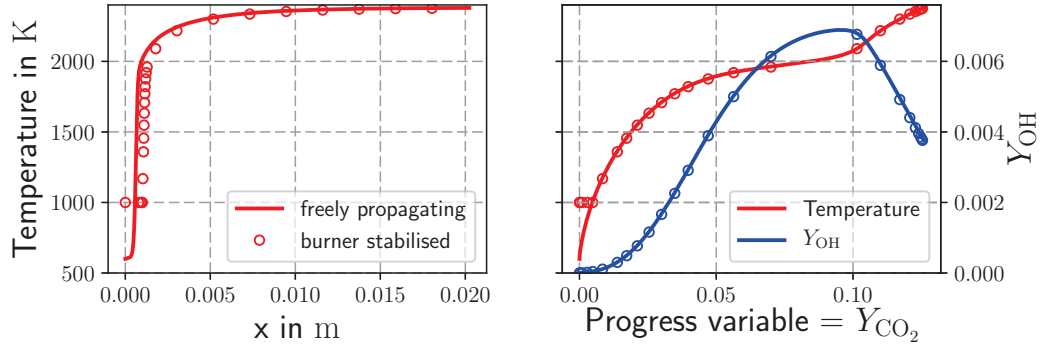


Figure 2.14.: A freely propagating flame with an initial temperature value of 600 K and burner-stabilized flame with an initial temperature value of 1000 K expressed in physical space (left) and composition space (right). The solid lines are solutions for the FP flame and the circles correspond to the BS flame. The temperature is marked in red whereas the mass fractions of OH are denoted in blue.

The thermo-chemical state φ of a BS flames is obtained for a fixed mixture fraction Z and the selected M_{flux} . Based on Equations (2.65) and (2.101), the following mapping is defined for the PFLUT.

$$\varphi_{BS}(Z, x, M_{flux}) \stackrel{(2.65)}{\longleftarrow} \stackrel{(2.101)}{\longrightarrow} \varphi(Z, Y_c, h_g) \quad (2.102)$$

Coupling strategy for non-adiabatic FLUT

The remaining question of this section is: How can the different enthalpy levels be included in a FLUT? This question will be answered in this section.

By accounting for non-adiabatic conditions, the enthalpy h_g varies over the mixture fraction Z . It is important to note, that the progress variable Y_c changes with Z and h_g . In line with the discussion in Sec. 2.3.3 on the advantages of using the normalized PV C instead of Y_c , a normalized enthalpy H is introduced

$$H = \frac{h_g - h_{g,min}(Z)}{h_{g,max}(Z) - h_{g,min}(Z)}. \quad (2.103)$$

Similarly to the PV the minimum of the enthalpy $h_{g,min}(Z)$ and the maximum $h_{g,max}(Z)$ also have to be included in a non-adiabatic FLUT.

For a FLUT defined for Z , H and C , at least three look-ups have to be performed in order to retrieve the thermo-chemical state φ based on the available parameters Z , h_g and Y_c . The procedure is outlined in Figure 2.15. The first interpolation is necessary to correct the normalized enthalpy H based on Eq. (2.103), the second one to calculate the normalized progress variable C as in Eq. (2.81) and finally the theoretically last look-up to obtain the state φ .

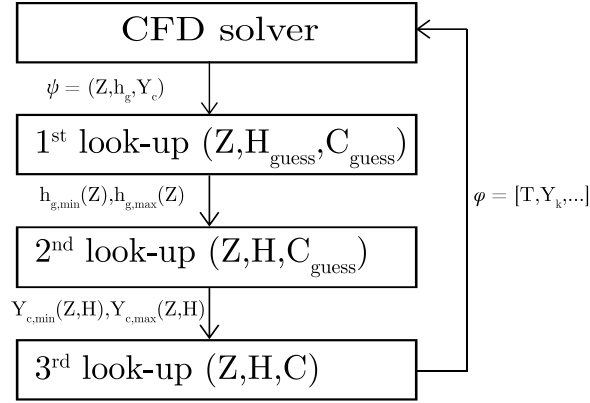


Figure 2.15.: Workflow of look-up properties from non-adiabatic FLUTs.

In practice it turns out that, due to the different mappings, H also depends on C , so additional interpolations need to be done for an iterative procedure until the following holds

$$\begin{aligned}
 Z &\approx Z^{FLUT}, \\
 h_g &\approx h_g^{FLUT}, \\
 Y_c &\approx Y_c^{FLUT}.
 \end{aligned} \tag{2.104}$$

In this work not more than five interpolations were necessary to reach the above conditions.

2.3.6 Flamelet/Progress Variable (FPV) model for laminar coal flames

For flamelet modeling for laminar gaseous flames, two-dimensional tables are mostly sufficient [36, 69, 82, 88]. However, coal releases two different fuel streams for pyrolysis and char burnout, respectively, resulting in two mixture fractions Z_{vol} , Z_{char} describing the process by which the fuel stream mixes with the oxidizer. They are defined by

$$Z_{\text{vol}} = \frac{m_{\text{g,vol}}}{m_g + m_{\text{g,vol}} + m_{\text{g,char}}}, \tag{2.105}$$

$$Z_{\text{char}} = \frac{m_{\text{g,char}}}{m_g + m_{\text{g,vol}} + m_{\text{g,char}}}, \tag{2.106}$$

where the mass m_g measures the mass of the gas stream introduced into the domain separately from coal particles, $m_{\text{g,vol}}$ and $m_{\text{g,char}}$ denote the mass of the released volatiles and char gases, respectively.

The thermo-chemical state φ in a coal calculation is parametrized by the progress variable Y_c , the mixture fraction for the volatiles Z_{vol} , the mixture fraction for the char Z_{char} and the total gas enthalpy h_g

$$\varphi = \varphi(Y_c, Z_{\text{vol}}, Z_{\text{char}}, h_g). \tag{2.107}$$

For all four parameters a transport equation⁵ is solved

$$\rho_g v_g \frac{\partial Z_{\text{vol}}}{\partial x} = \frac{\partial}{\partial x} \left(\rho_g D_{Z_{\text{vol}}} \frac{\partial Z_{\text{vol}}}{\partial x} \right) + \dot{S}_{Z_{\text{vol}}}, \quad (2.108)$$

$$\rho_g v_g \frac{\partial Z_{\text{char}}}{\partial x} = \frac{\partial}{\partial x} \left(\rho_g D_{Z_{\text{char}}} \frac{\partial Z_{\text{char}}}{\partial x} \right) + \dot{S}_{Z_{\text{char}}}, \quad (2.109)$$

$$\rho_g v_g \frac{\partial Y_c}{\partial x} = \frac{\partial}{\partial x} \left(\rho_g D_c \frac{\partial Y_c}{\partial x} \right) + \sum_{k=1}^{N_s} \alpha_k \dot{\omega}_k + \dot{S}_{Y_c}, \quad (2.110)$$

$$\rho_g v_g \frac{\partial h_g}{\partial x} = \frac{\partial}{\partial x} \left(k_g \frac{\partial T_g}{\partial x} \right) - \sum_{k=1}^{N_s} \frac{\partial}{\partial x} (\rho_g Y_k V_k h_k) + \dot{S}_h, \quad (2.111)$$

where the corresponding source terms \dot{S}_α , which describe the particle-gaseous phase interactions, are given by

$$\dot{S}_{Z_{\text{vol}}} = n_p (\dot{m}_{\text{vol}}(1 - Z_{\text{vol}}) - \dot{m}_{\text{char}} Z_{\text{vol}}), \quad (2.112)$$

$$\dot{S}_{Z_{\text{char}}} = n_p (\dot{m}_{\text{char}}(1 - Z_{\text{char}}) - \dot{m}_{\text{vol}} Z_{\text{char}}), \quad (2.113)$$

$$\dot{S}_{Y_c} = n_p \left(\dot{m}_{\text{vol}} \sum_{k=1}^{N_s} \alpha_k (Y_{k,\text{vol}} - Y_k) + \dot{m}_{\text{char}} \sum_{k=1}^{N_s} \alpha_k (Y_{k,\text{cb}} - Y_k) \right), \quad (2.114)$$

$$\dot{S}_h = n_p \dot{q}_{\text{conv}} + n_p \sum_{k=1}^{N_s} (\dot{m}_{\text{vol}} Y_{k,\text{vol}} + \dot{m}_{\text{char}} Y_{k,\text{cb}}) h_k(T_p) - n_p \dot{m}_p h_g. \quad (2.115)$$

In contrast to pure gaseous applications the mixture fractions are non-conserved scalars due to the source terms from the dispersed phase.

In addition, the particle Equations (2.37) to (2.40) are solved for the FPV model for laminar coal flames suggested here.

The principal concept of using two mixture fraction has already been applied in the context of multiple fuel injections in diesel engines [92, 93]. In order to obtain a regular parameter set, two parameters were introduced according to the authors' suggestions

$$Z_{\text{sum}} = Z_{\text{char}} + Z_{\text{vol}}, \quad (2.116)$$

$$Y = \frac{Z_{\text{vol}}}{Z_{\text{sum}}}, \quad (2.117)$$

where Z_{sum} is the sum of the mixture fractions for volatiles and char burnout and Y describes the ratio of volatiles in the total fuel mixture. The mapping region is visualised in Figure 2.16. The ratio Y completely occupies the range $[0, 1]$, whereas Z_{char} could never reach the value of one, because oxygen is needed to produce CO in the heterogeneous reaction (Eq. (2.16)). Therefore the modified mixture fraction Z^* is introduced as follows

$$Z^* = Z_{\text{sum}} (Y + (1 + \alpha_{cb})(1 - Y)), \quad (2.118)$$

⁵ For the sake of convenience only the equations for one-dimensional strained flow coal flames are reported.

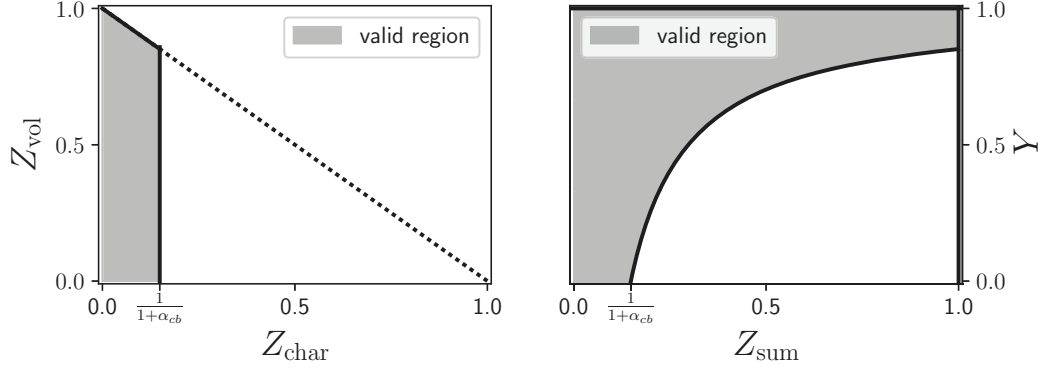
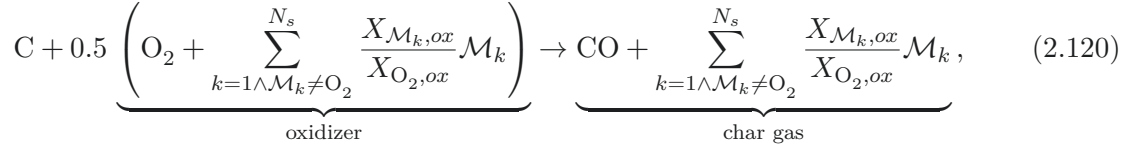


Figure 2.16.: Transformation of mixture fractions Z_{vol} and Z_{char} into $Z_{\text{sum}}-Y$ space. The valid region of the mixture fraction is limited to the necessity of oxygen for char burnout. For air thus follows that $\alpha_{\text{cb}} \approx 5.72$ and $Z_{\text{char,max}} \approx 0.149$.

with the mass ratio of consumed oxidant $m_{\text{ox,cb}}$ per converted carbon $m_{\text{C,cb}}$ defined by

$$\alpha_{\text{cb}} = \frac{m_{\text{ox,cb}}}{m_{\text{C,cb}}} = \frac{\bar{M}_{\text{ox}}}{2X_{\text{O}_2}M_{\text{C}}}. \quad (2.119)$$

The ratio α_{cb} is based on the full consumption of oxygen in the oxidizer for char burnout



where \mathcal{M}_k denotes the chemical symbol for the species subscript k . The modified mixture fraction Z^* occupies the whole $[0, 1]$ domain.

The concept of using pure gaseous flamelet look-up tables for two phase flows was originally introduced by Franzelli et al. [66] for spray flames. This concept is adapted in this work for coal flames. The flamelet look-up tables are now produced according to the procedures discussed in the previous sections, employing Z^* as the mixture fraction Z . The definition of the oxidizer does not change. The mass fractions $Y_{k,\text{fuel}}$ for the fuel are obtained with

$$Y_{k,\text{fuel}} = \frac{Y Y_{k,\text{vol}} + (1 + \alpha_{\text{cb}}) (1 - Y) Y_{k,\text{char}}}{Y + (1 + \alpha_{\text{cb}}) (1 - Y)}, \quad (2.121)$$

where $Y_{k,\text{vol}}$ is the volatile composition and $Y_{k,\text{char}}$ is the char gas composition and depends on the applied oxidizer. The char gas composition is defined similarly to [7, 40]

$$Y_{k,\text{char}} = \begin{cases} 0, & \text{for } k = \text{O}_2 \\ \frac{M_{\text{CO}} \left(1 + \frac{X_{\text{CO,ox}}}{2X_{\text{O}_2, \text{ox}}} \right)}{\frac{M_{\text{C}}(1 + \alpha_{\text{cb}})}{M_k X_{k,\text{ox}}}}, & \text{for } k = \text{CO} \\ \frac{M_k X_{k,\text{ox}}}{2X_{\text{O}_2, \text{ox}} M_{\text{C}}(1 + \alpha_{\text{cb}})}, & \text{else} \end{cases} \quad (2.122)$$

and were derived from Eq. (2.120). The temperature for the fuel is set to the particle temperature T_p at the inlet.

In order to assess the applicability of the tables, the *a priori* and the *a posteriori* analysis are introduced in the following.

A priori analysis

The scope of the *a priori* analysis is to work out the stand-alone error of retrieving the thermo-chemical state φ using the table parameters from the FTC results directly in the workflow introduced in Section 2.3.3. The thermo-chemical state $\varphi^{FLUT} (Z^{FTC}, Y_C^{FTC}, \text{etc.})$ can be directly compared to the corresponding state φ^{FTC} of the FTC solution. The procedure is outlined in Figure 2.17. This method allows to evaluation of whether a FLUT can correctly

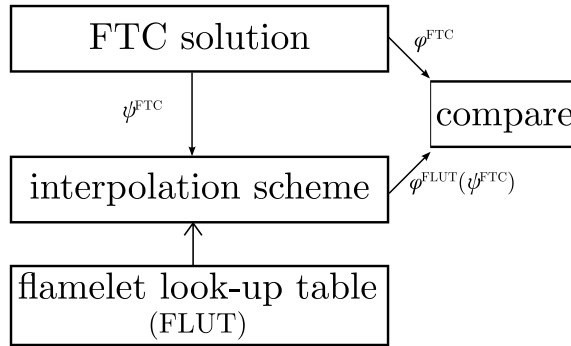


Figure 2.17.: Sketch of the *a priori* analysis for FLUTs.

reproduce the results, assuming that the flow behaviour is identical, instead of performing a fully coupled FPV simulation.

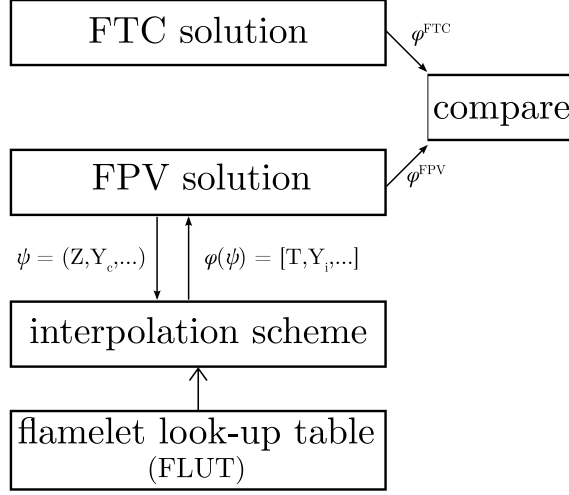
A posteriori analysis

In an *a posteriori* analysis a fully coupled simulation is performed using the thermo-chemical state φ obtained from a FLUT for the FPV model. For a converged FPV solution the state φ^{FPV} is then directly compared to the corresponding state φ^{FTC} of the FTC simulation (Fig. 2.18). This analysis allows the cumulated error for the applied FLUT to be quantified at the tested conditions.

Usually the cumulated error of an *a posteriori* analysis is expected to be greater than the stand-alone error of an *a priori* analysis.

2.3.7 Flamelet tabulation for turbulent coal flames

Like Section 2.3.4 this is just brief glance at how to enhance flamelet modeling for turbulent coal flames. A LES has to provide filtered mixture fractions \widetilde{Z}_{vol} , \widetilde{Z}_{vol} , the filtered progress variable \widetilde{Y}_c , filtered enthalpy \widetilde{h}_g and subgrid variance of the sum of the mixture fractions $\widetilde{Z}_{sum}''^2$.


 Figure 2.18.: Sketch of the *a posteriori* analysis for FLUTs.

The laminar state has to be filtered to obtain the filtered state

$$\tilde{\varphi} = \int \int \varphi(Y, Z^*, C, H) \tilde{P}(Y, Z^*, C, H) dY dZ^* dC dH. \quad (2.123)$$

Assuming statistical independence allows the joint PDF $\tilde{P}(Y, Z^*, C, H)$ to be separated into three PDFs

$$\tilde{P}(Y, Z^*, C, H) = \tilde{P}(Y, Z^*) \tilde{P}(C) \tilde{P}(H). \quad (2.124)$$

Filtering (Eq. (2.123)) is performed by applying a two-dimensional presumed β -PDF for $P(Y, Z^*)$ and a δ -PDF for $P(C)$ and $P(H)$. The two-dimensional β -distribution for Z_{vol} and Z_{char} is given as [94]

$$\tilde{P}^*(Z_{\text{vol}}, Z_{\text{char}}) = \frac{\Gamma(\beta_1 + \beta_2 + \beta_3)}{\Gamma(\beta_1)\Gamma(\beta_2)\Gamma(\beta_3)} Z_{\text{vol}}^{\beta_1-1} (Z_{\text{char}})^{\beta_2-1} (1 - Z_{\text{vol}} - Z_{\text{char}})^{\beta_3-1}, \quad (2.125)$$

where

$$\beta_1 = \tilde{Z}_{\text{vol}} \left[\frac{1-S}{Q} - 1 \right], \quad (2.126)$$

$$\beta_2 = \tilde{Z}_{\text{char}} \left[\frac{1-S}{Q} - 1 \right], \quad (2.127)$$

$$\beta_3 = (1 - \tilde{Z}_{\text{vol}} - \tilde{Z}_{\text{char}}) \left[\frac{1-S}{Q} - 1 \right] \quad (2.128)$$

and

$$\frac{1-S}{Q} = \frac{\tilde{Z}_i - \tilde{Z}_i^2}{\tilde{Z}_i'^2} \quad \forall i \in \{\text{vol}, \text{char}, \text{sum}\}. \quad (2.129)$$

PHYSICAL MODEL FORMULATIONS

Based on the mapping from $(Z_{\text{vol}}, Z_{\text{char}})$ -space into (Y, Z^*) -space, the joint-pdf $\tilde{P}(Y, Z^*)$ reads [92]

$$\tilde{P}(Y, Z^*) = \frac{1}{J(Z_{\text{vol}}, Z_{\text{char}})} P^*(Z_{\text{vol}}, Z_{\text{char}}) \quad (2.130)$$

where $J(Z_{\text{vol}}, Z_{\text{char}})$ is the determinant of the Jacobian for the mapping

$$J(Z_{\text{vol}}, Z_{\text{char}}) = \det \begin{pmatrix} \frac{\partial Z^*}{\partial Z_{\text{vol}}} & \frac{\partial Z^*}{\partial Z_{\text{char}}} \\ \frac{\partial Y}{\partial Z_{\text{vol}}} & \frac{\partial Y}{\partial Z_{\text{char}}} \end{pmatrix} = \det \begin{pmatrix} 1 & 1 + \alpha_{cb} \\ \frac{Z_{\text{char}}}{Z_{\text{sum}}^2} & -\frac{Z_{\text{vol}}}{Z_{\text{sum}}^2} \end{pmatrix} = -\frac{Z^*}{Z_{\text{sum}}^2}. \quad (2.131)$$

Filtering can be performed in advance and the filtered quantities can be stored in FLUTs.

RESULTS

In this section the complexity of coal modeling is increased in following steps:

1. a purely numerical study of strained counterflow flames without char combustion (Sec. 3.1),
2. a strained stagnation flow flame with almost no char burnout (Sec. 3.2),
3. a modified stagnation flow flame with detectable char conversion (Sec. 3.3).

For the strained counterflow flame of devolatilizing coal particles, the principal applicability of the FPV approach for coal flames is shown. Further, the necessity of including non-adiabatic solutions in the tables is discussed with the help of an *a priori* analysis.

A flame structure analysis is performed to identify the corresponding flame type and to discover which FLUT type is the most promising for which of the flames considered. Afterwards an *a posteriori* analysis will show the cumulated error of the selected FLUT in each case.

The validity of the proposed look-up tables for pulverized coal flame modeling including char oxidation will be given in Section 3.2, in addition to section 3.1.

The available experimental data for the strained stagnation flames in Section 3.2 are utilized to validate the FTC simulations for pure gaseous simulations as well as for simulation including coal modeling.

Finally, a parametric study on coal loading and inlet velocity is conducted to demonstrate the applicability of the FPV approach using *a posteriori* analysis.

3.1 COUNTERFLOW FLAMES

The purpose of this section is to investigate strained counterflow flames with pulverized coal flames as outlined in Figure 2.2a in order to show the applicability of the proposed tabulation strategy. The discussion on this type of flames follows and extends the discussion of Messig et al. [8]. In this purely numerical setup, highly volatile bituminous Pittsburgh coal is fed at the upper nozzle with preheated air. The temperatures of the coal and air are set to 700 K in order to create favorable conditions for starting the thermal conversion of the raw coal. This study uses a mono-disperse distribution of the particles with an initial diameter of 100 μm and an initial apparent density of 1000 $\frac{\text{kg}}{\text{m}^3}$. The ultimate and proximate analyses

RESULTS

Table 3.1.: Proximate and ultimate analysis of Pittsburgh coal as received.

Proximate analysis		Ultimate analysis	
Volatile matter	35.89	C	75.23
Fixed carbon	56.46	H	5.16
Moisture	0.47	O	9.83
Ash	6.95	N	1.43
HHV	30.94 $\frac{\text{MJ}}{\text{kg}}$	S	2.00

of the coal, which is introduced are the same as in [46, 77] and reported in Table 3.1. The SFOR parameters and the volatile composition are listed in Table 3.2. Here, the CPD model [1] was used to obtain the parameters from the fitting procedure which were described in [5]. Similar results were obtained considering the models FG-DVC [2] and FLASHCHAIN [3], respectively. The heating value of the coal as received is also reported in Table 3.1, while

Table 3.2.: Parameters of the SFOR devolatilization model and volatile composition for the Pittsburgh coal fitted according to [5].

SFOR model	
A	$72.0549 \times 10^3 \frac{1}{\text{s}}$
E	$54.285 \frac{\text{kJ}}{\text{molK}}$
y_{vol}	0.54
Volatile composition (% mass)	
CH_4	0.547%
C_6H_6	22.433%
C_2H_4	37.044%
CO	37.696%
H_2	0.236%
N_2	2.044%

the value for the volatile matter is calculated from the enthalpy of formations of the species, reported in Table 3.2. Based on Eq. 2.14, the heat of pyrolysis $\Delta h_{\text{pyr}}(T_{\text{ref}})$ is calculated as $0.269 \frac{\text{MJ}}{\text{kg}}$. The stoichiometric mixture fraction for the reaction of the prescribed volatile composition with air is then given by $Z_{st} = 0.096$. A swelling factor of $\text{Sw} = 1.05$ is applied to all simulations.

The lower nozzle is fed with secondary pre-heated air at same temperature as the primary air. The distance between the two nozzles is fixed at 0.02 m. In order to establish different flame regimes, the initial coal-to-oxidizer ratio α_{in} and the inlet velocity v_{in} are varied. The selected values are reported in Table 3.3. The second case is the reference case, the first case then shows the effect of reduced loading and the third case that of increasing the inlet velocity.

For the cases considered, a reduced version of the CRECK kinetic mechanism [95] is used, which contains 52 species and 452 reactions. This mechanism was developed by applying the

Table 3.3.: Input conditions for the reference cases.

Name	α_{in}	v_{in} in $\frac{m}{s}$
case 1	0.2	0.3
case 2	0.5	0.3
case 3	0.5	0.7

automatic reduction techniques described in [96] to predict the ignition of single coal particles [97]. For the species diffusion the $Le = 1$ approach, is used in this section.

Char oxidation is much slower compared to the devolatilization of coal particles and requires the presence of oxygen. Due to the relatively low residence time and the consumption of oxygen during volatiles combustion, char oxidation is negligible for these counterflow flames. Therefore, throughout this section char burnout is not considered, so the mixture fraction Z and the mixture fraction for volatiles Z_{vol} are used synonymously.

3.1.1 *Flame structure analysis in strained counterflow coal flames*

A flame structure analysis is performed in order to determine the burning mode of the configuration in order to suggest the appropriate tabulation strategy. The results of the FTC simulations for the reference cases are reported in Fig. 3.1 showing several profiles of solid and gas phases properties in physical space. In all the plots, the position of the stagnation plane ($v_g = 0$) is marked by the vertical dashed lines, while the horizontal lines in the third row denote the stoichiometric mixture fraction ($Z_{st} = 0.096$). All cases show a slow release of volatiles directly after injection. As soon as an ignitable mixture is reached, the gas temperature rises because of chemical reactions. Due to the convective heat transfer the particle temperature also increases, accompanied by an acceleration of the devolatilization process. While the particles are heating up, the local coal-to-oxidizer ratio α increases in all the cases, caused by the higher inertia of the coal. With the increased mass transfer by devolatilization from the particles to the gas phase α decreases. Finally, the ratio increases again because of the inertia near the stagnation plane. Apart from the last case, the volatiles are released completely.

The mixture fraction profile in the first case reaches values slightly above stoichiometry. In the other cases, significantly higher values of mixture fractions are obtained, which leads to different flame structures. The first case just shows one temperature peak, while the other cases have two peaks with a temperature decrease for high values of Z_{vol} .

Similar results are found for the product species CO_2 and H_2O . Typically of near - stoichiometric flames such as the first case typically, one peak of H_2O and nearly one of CO_2 are observed in the flame. In the region above stoichiometry, a small peak of CO compared to CO_2 is also found. The other fuel-rich cases exhibit two peaks of CO_2 and H_2O , while CO reaches values higher than CO_2 in the centre of the configuration. Oxygen is also completely consumed for the second and third cases.

RESULTS

To gain insights into the flame structure two flame markers are investigated: the heat release rate and the chemical explosive mode. First, positive peaks in the heat release rate $\dot{\omega}_T$ (see Eq. (A.39)) can identify the existence of a reaction zone [98, 99]. Then, the flame type can be determined using Chemical Explosive Mode Analysis (CEMA) [100, 101]. CEMA is based on an evaluation of the largest non-conservative eigenvalues λ_e of the chemical Jacobian \mathbf{J}_c

$$(\mathbf{J}_c)_{i,j} = \begin{cases} \frac{\partial \dot{\omega}_i}{\partial Y_j}, & \text{for } i, j \in \{1, \dots, N_s\} \\ \frac{\partial \dot{\omega}_i}{\partial T}, & \text{for } i \in \{1, \dots, N_s\} \text{ and } j = N_s + 1 \\ \frac{\partial \dot{\omega}_T}{\partial Y_j}, & \text{for } j \in \{1, \dots, N_s\} \text{ and } i = N_s + 1 \\ \frac{\partial \dot{\omega}_T}{\partial T}, & \text{for } i = N_s + 1 \text{ and } j = N_s + 1 \end{cases} . \quad (3.1)$$

The mixture is *chemically explosive* if the real part of λ_e ($Re(\lambda_e)$) is positive, otherwise it is *chemically non-explosive* [100]. A premixed flame is identified by the zero-crossing of $Re(\lambda_e)$, which represents the transition from the chemically explosive state of the reactants to the chemically non-explosive state for the products. On the other hand, a diffusion flame can be identified by positive peaks of $\dot{\omega}_T$ close to the stoichiometric conditions with the chemical non-explosive mode $Re(\lambda_e) < 0$.

For visualisation purposes the chemical mode γ_e proposed by Shan et al. [101] is used

$$\gamma_e = \text{sign}(\text{Re}(\lambda_e)) \cdot \log_{10}(1 + |\text{Re}(\lambda_e)|) , \quad (3.2)$$

where “sign” is the sign function. The heat release rate $\dot{\omega}_T$ and the chemical mode γ_e are reported in the last row of Fig. 3.1. The zero-crossing of γ_e combined with the first $\dot{\omega}_T$ peak indicates a lean premixed flame in all cases. The connected temperature increase supports the release of further volatiles and vice versa. Therefore a non-premixed flame, identified by the second $\dot{\omega}_T$ peak at stoichiometric conditions with negative γ_e , can be established near the first premixed flame. Due to the availability of more volatiles in the cases with higher particle loadings, a fuel-rich mixture is produced towards the centre of configuration. Near the stagnation plane, this mixture comes into contact with the secondary air and establishes a second non-premixed flame.

In conclusion, the cases depict complex flame structures with combinations of premixed and non-premixed reaction zones, which is challenging when it comes to applying a suitable tabulation strategy. Therefore, the next section evaluates the suitability of a PFLUT and a DFLUT according to the *a priori* analysis described in Section 2.3.6.

RESULTS

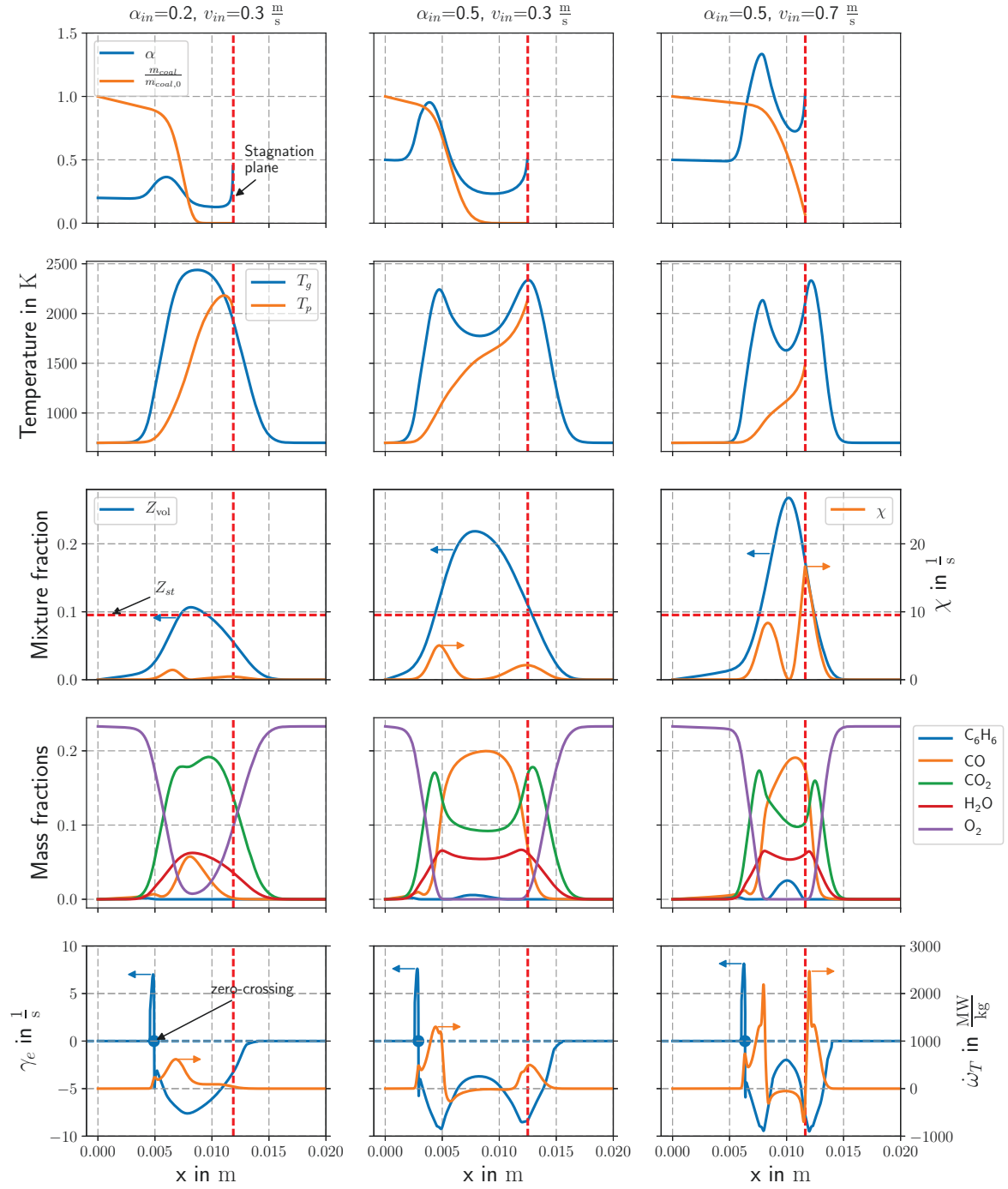


Figure 3.1.: The flame structure analysis of the strained coal counterflow flames for the cases listed in Table 3.3. The vertical dashed lines mark the stagnation planes. The horizontal dashed lines in the third row indicate the stoichiometric mixture ($Z_{st} = 0.096$). The horizontal dashed lines in the last row show $\gamma_e = 0$ and the marked points indicate the zero-crossing of γ_e .

RESULTS

3.1.2 *A priori* analysis of flamelet look-up tables

This section addresses the *a priori* analysis for the three counterflow coal cases listed in Table 3.3. The results for the temperature and selected species of the *a priori* analysis for both tables (PFLUT and DFLUT) are reported in Figure 3.2. The thermo-chemical state

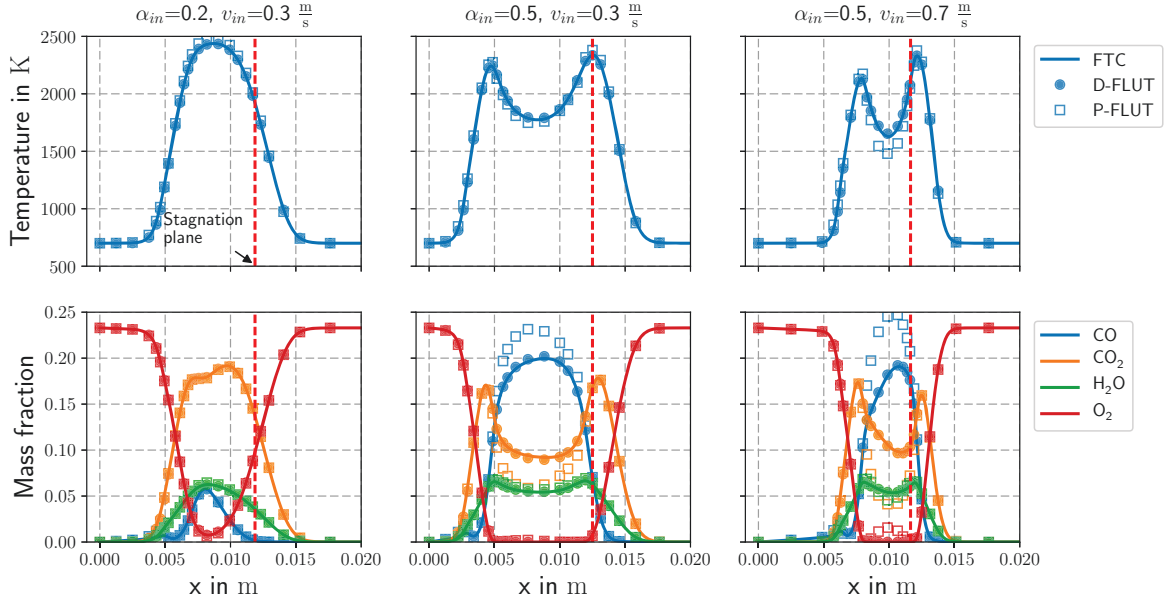


Figure 3.2.: The *a priori* analysis of a DFLUT (circles) and a PFLUT (squares) for all the three cases (Tables 3.3). FTC results (solid lines) are used as reference solutions. The vertical dashed lines mark the stagnation planes. The horizontal dashed lines in the first row indicate the stoichiometric mixture fraction ($Z_{st} = 0.096$).

obtained from a DFLUT agrees very well with the thermo-chemical state of the FTC solution in all cases. The PFLUT approach works sufficiently well for the first case, but shows large differences in temperature and the species CO and CO₂ for cases with higher particle loading in the fuel-rich region compared to the corresponding FTC results. According to the previous flame structure analysis (Section 3.1.1) this is the region between the two non-premixed flames, which cannot be captured in tables based on premixed flames.

3.1.3 *Influence of different enthalpy levels in the flamelet look-up table*

As shown in Section 2.3.5, it is possible to include enthalpy losses in flamelet look-up tables. The question arises of whether it is necessary to account for the enthalpy defect in the tables for coal-loaded flames.

The large influence of the heat transfer between the particles and gas phase is visualised in the first row of Figure 3.3. The dashed lines show pure mixing of air and volatiles, where solid lines are the calculated total enthalpies. The enthalpy defect increases as the strain rises. A

RESULTS

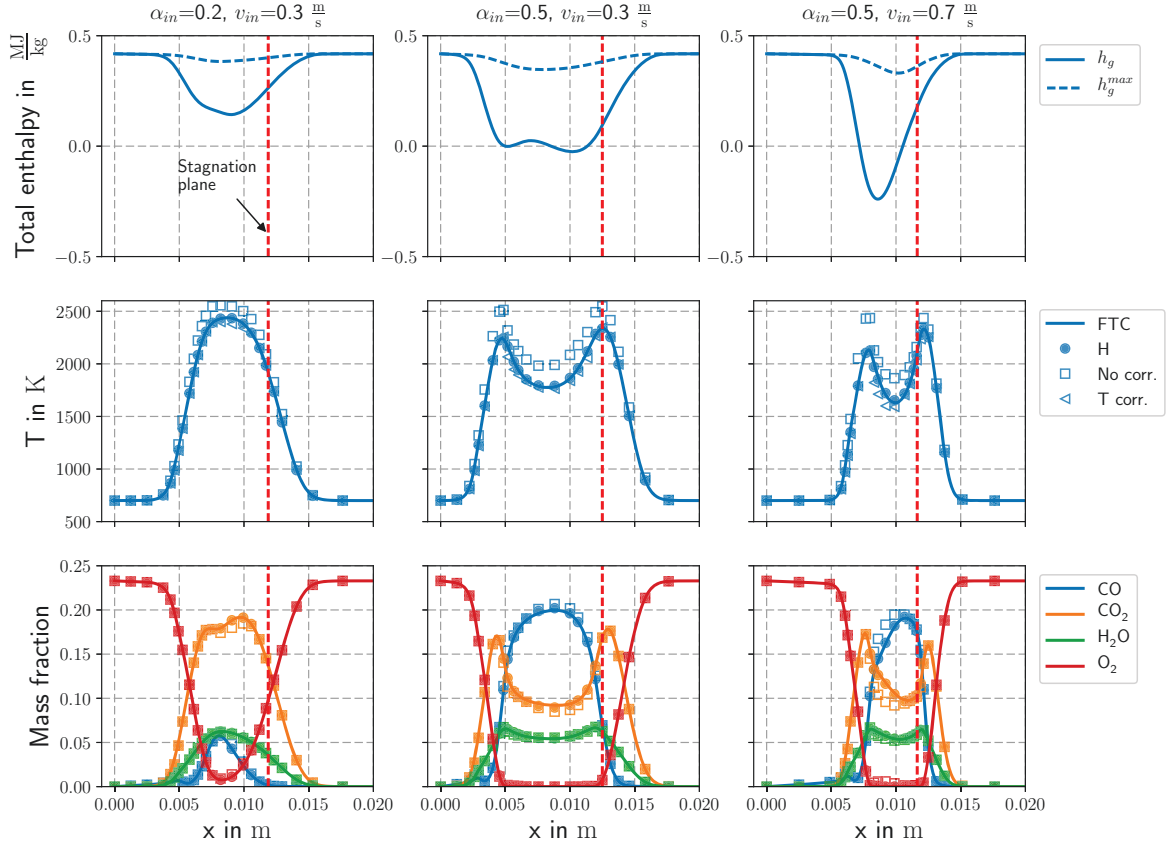


Figure 3.3.: *A priori* analysis using a DFLUT. Circles (H) show the results for a table with multiple levels of enthalpy. Squares (*No corr.*) and triangles (*T corr.*) show the results for an adiabatic table with and without temperature correction, respectively. The vertical dashed lines mark the stagnation plane.

common way to account for heat losses in purely gaseous simulations is to correct only the gas temperature [8, 102]

$$T_g^{\text{corr}} = T_g^{\text{FLUT}}(Z, C) + \frac{h_g^{\text{FTC}} - h_g^{\text{FLUT}}(Z, C)}{c_p^{\text{FLUT}}(Z, C)} \quad (3.3)$$

and update all temperature-dependent mixture properties. The last two rows of Figure 3.3 show the *a priori* analyses for a DFLUT accounting for the enthalpy defect (indicated by circles) and an adiabatic DFLUT with and without temperature correction according to Eq. (3.3) (indicated by triangles and squares, respectively). As expected, an overestimation of the temperature (up to 300 K) in the flame zone is observed when the enthalpy effects (squares) are ignored. Similarly to previous findings for the total enthalpy, the deviations in temperature is more evident with higher strain and particle loading. By performing a temperature correction (triangles) the opposite trend is obtained, although the deviations are less significant with respect to the non-corrected temperature profiles. The results of the *a priori* analysis for the species are shown in last row. As for the temperature, significant differences can be seen in regions of high enthalpy defect. Especially the overestimation of

RESULTS

CO in connection with the underestimation of CO_2 could be related to the dissociation of CO_2 for higher temperatures. However, to recapitulate the findings from Section 3.1.2, very good agreement is obtained for DFLUT accounting for enthalpy losses.

In conclusion, non-adiabatic look-up tables are necessary to correctly describe the progress of the thermo-chemical state in the coal flames considered here.

3.1.4 *The a posteriori analysis for a non-adiabatic DFLUT*

Based on the results of the *a priori* analysis (Section 3.1.2), only the reasonable results of the FPV with the non-adiabatic DFLUT are considered for the *a posteriori* analysis (see Sec. 2.3.6). The results for the transported variables Z_{vol} and Y_C is visualised in the first row of Figure 3.2 for all three cases. The general trend of this parameters is reproduced very well by the FPV-method compared to the FTC solution. The slight over-prediction of PV near the coal inlet is caused by differences in the PV source term $\dot{\omega}_c$ due to the interpolation between the quenched and the first burning solution in the non-premixed table. In addition, the flame analysis (Section 3.1.1) shows a lean premixed flame structure in this zone which cannot be captured perfectly with non-premixed flames. In all other parts of the domain only minor differences can be observed. The *a posteriori* analysis also compares relatively well in terms of the temperature, species and progress variable source term. The small deviations are directly linked to differences for PV. In conclusion, the FPV model with the non-premixed table is able to predict strained counterflow coal flames and the chemical state is a very sensitive with respect to the PV.

RESULTS

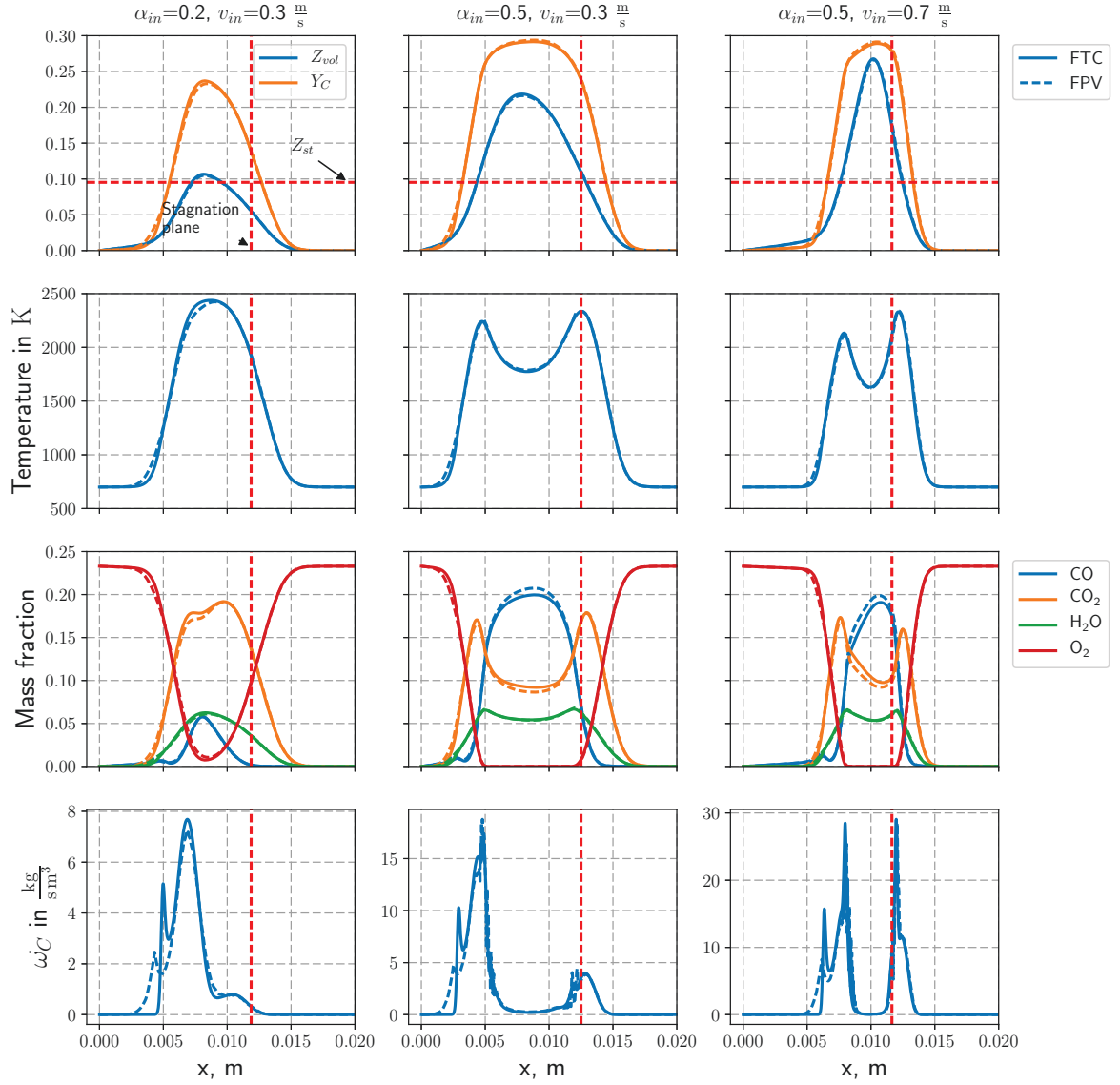


Figure 3.4.: The *a posteriori* analysis of the DFLUT FPV (dashed lines) comparing results from the FTC (solid lines) as reference solutions for all the cases listed in Table 3.3. The vertical dashed lines mark the stagnation plane. The horizontal dashed lines in the first row show the stoichiometric mixture fraction ($Z_{st} = 0.096$).

RESULTS

3.1.5 Intermediate summary for counterflow flames

The major findings of section 3.1 for the strained counterflow coal flames considered here can be summarized as follows:

- The flame structure analysis indicates that there is a weak lean premixed flame near the coal inlet, followed by a non-premixed flame caused by the volatiles mixing with the primary air. A second non-premixed reaction zone is established near the stagnation plane for higher coal loadings.
- The applicability of a DFLUT for the cases considered here is proven using the *a priori* analysis. The results of this analysis agree very well with the FTC simulations. The predictions of the PFLUT depict a rather poor agreement in the fuel-rich region.
- The *a priori* analysis further shows the need to include non-adiabatic flames in tables for coal flames, especially for predicting the species profiles. The temperature correction approach is found not to be sufficient here.
- And finally the *a posteriori* analysis confirms that the FPV model with the non-premixed look-up table is able reproduce complex flame structures with up to three reaction zones in these coal flames.

Despite the good results obtained for the *a priori* and the *a posteriori* analysis of the cases considered here, future investigations are required to evaluate the influence of char oxidation.

3.2 STAGNATION FLOW FLAMES REPORTED BY XIA ET AL. [9]

This section examines the strained stagnation flow flame configuration originally reported by Xia et al. [9] in order to validate the FTC-method. Photographs of the experiments are given in Figure 3.5. For the purely gaseous flame in Fig. 3.5a a typical blue flame for methane is

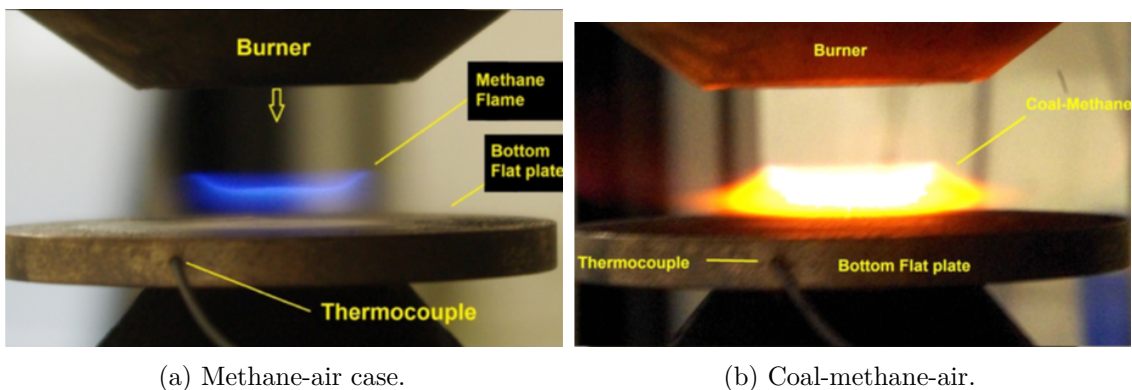


Figure 3.5.: Direct views on the investigated flames [16].

visible, whereas a yellow/orange flame is observed for the coal-loaded case on the right. This

RESULTS

yellow/orange flame is typical of coal-loaded flames due to particle radiation. A sketch of the setup with coal was already presented in Figure 2.2b on page 13.

A lean premixed methane-air stream (equivalence ratio $\phi = 0.82$) is injected at ambient pressure with or without coal particle loading. The stream then impacts on an isothermal wall at 600 K. The initial temperatures for gaseous phase is 310 K and initial the coal particle temperature is assumed to be the same [9]. The distance between the nozzle and the wall is 10 mm. The coal particles are injected at a gas flow velocity of $1.6 \frac{\text{m}}{\text{s}}$.

Xia et al. [9] reported experimental normalized species profiles for OH, CH \cdot and C $_2\cdot$ radicals. They used planar laser-induced fluorescence (PLIF) for the OH radicals and imaging of CH \cdot , C $_2\cdot$ spontaneous emissions to identify the flame structure. For more details on the diagnostic techniques used, please refer to [9].

In the following Section the purely methane-air flame is investigated to validate the developed code for gaseous flames. In Section 3.2.2 the sensitivity of parameters for the coal modeling on the results is discussed.

3.2.1 Methane-air flame

This section introduces the sensitivity of the gas phase modeling to the mechanism used, as well as the diffusion modeling approach considered. Afterwards, the flame structure is analysed and finally an *a posteriori* analysis of this setup is performed to show, that the classical FPV-method works for this gaseous flames.

The first mechanism used is the same as in Section 3.1 and will be called “CRECK-based” in the following. To be able to compare the numerical results against all measured species profiles, the same mechanism is applied as in [9], where is named Xia-Mech. Finally, the well-known and established methane mechanism GRI-3.0 [103] is also investigated in order to evaluate the performance of the other two mechanisms. Important to note, that the GRI 3.0 cannot be used for the coal calculation due to the higher hydrocarbons contained in the volatiles. The number of species and number of reactions for the mechanisms investigated are given in Table 3.4 . The three mechanisms show almost identical results and are in very

Table 3.4.: Details on mechanisms used to validate FTC model for methane-air stagnation flame.

mechanism name	# species	# reactions
CRECK-based [97]	52	452
Xia-Mech [9]	131	916
GRI 3.0 [103]	53	325

good agreement in terms of predicting the OH peak compared to the non-coal experiments as reported in Figure 3.6. However, GRI-3.0 captures the flame front the best, Xia-Mech performs best for the peak value position and finally the CRECK-based mechanism is slightly off compared with the others. The deviations near the wall and before the flame front are

RESULTS

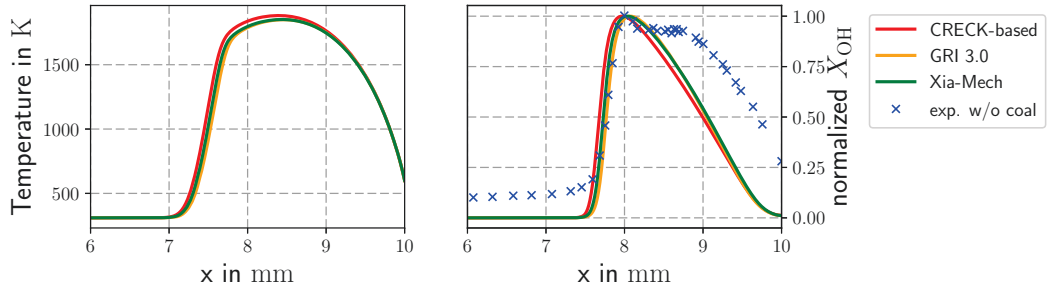


Figure 3.6.: Comparison of profiles in physical space for the mechanisms listed in Table 3.4: left plot: temperature, right plot: normalized OH mole fraction profiles compared to experiments [9].

also present in the numerical results by Xia et al. [9]. The temperature profiles for Xia-Mech and GRI-3.0 are almost identical, while the CRECK-based mechanism is shifted towards the inlet and shows higher temperatures compared to the others.

In contrast, the impact of diffusion modeling in the results is much higher, as visualised in Figure 3.7. The prediction of the flame front for the temperature is shifted towards the

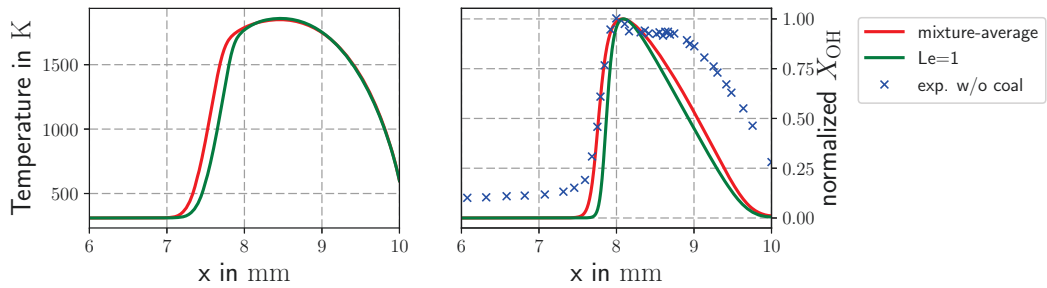


Figure 3.7.: Comparison of profiles for different diffusion modeling approaches using GRI-3.0 mechanism: left plot: temperature, right plot: normalized OH mole fraction profiles compared to experiments [9].

wall for the $Le = 1$ approach compared to the mixture-average approach. The prediction of the OH peak position are almost the same, while the OH profile for the $Le = 1$ approach is narrower and enclosed by the mixture-average profile.

Validation for the methane-air stagnation flow flame

As above stated, the GRI-3.0 and CRECK-based mechanisms do not contain the measured radicals $\text{CH}\cdot$ and $\text{C}_2\cdot$. Therefore the validation for these radicals is only performed for Xia-Mech. The numerical result for the measured radicals show contrary trends compared to the experimental profiles (see Fig. 3.8). While the numerical prediction the for $\text{CH}\cdot$ radical a slight shift towards the wall, the comparison for the $\text{C}_2\cdot$ radical exhibits a shift towards the nozzle. In general, the predictions show a narrower profile compared to the experiments, which could be related to the high noise-to-signal ratio [10]. However, these findings are consistent with the numerical profiles reported in [9]. It is important to note that there are relatively small maxi-

RESULTS

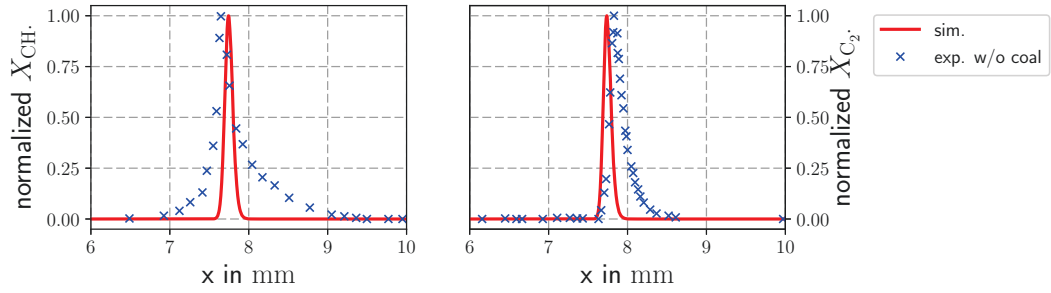


Figure 3.8.: Comparison of normalized $\text{CH}\cdot$ (left) and $\text{C}_2\cdot$ (right) mole fraction profiles between numerical and experimental results using Xia-Mech mechanism.

imum values for the calculated radicals ($\max(X_{\text{CH}\cdot}) = 1.33 \times 10^{-11}$, $\max(X_{\text{C}_2\cdot}) = 1.19 \times 10^{-10}$), which are in the same range as the specified tolerances in the simulations.

In conclusion, the modeling of the gaseous phase is able to predict the flame front and general trends of the experiments.

Flame structure analysis for the methane-air stagnation flow flame

Similarly to Section 3.1.1 a flame structure analysis is performed for the methane-air stagnation flame. For the pure premixed gaseous setup, one single premixed flame is expected. This anticipation is shown with results in Fig. 3.9, where the chemical mode γ_e and the HRR are displayed in the lower right plot. Both the peak of HRR and the zero-crossing of the chemical

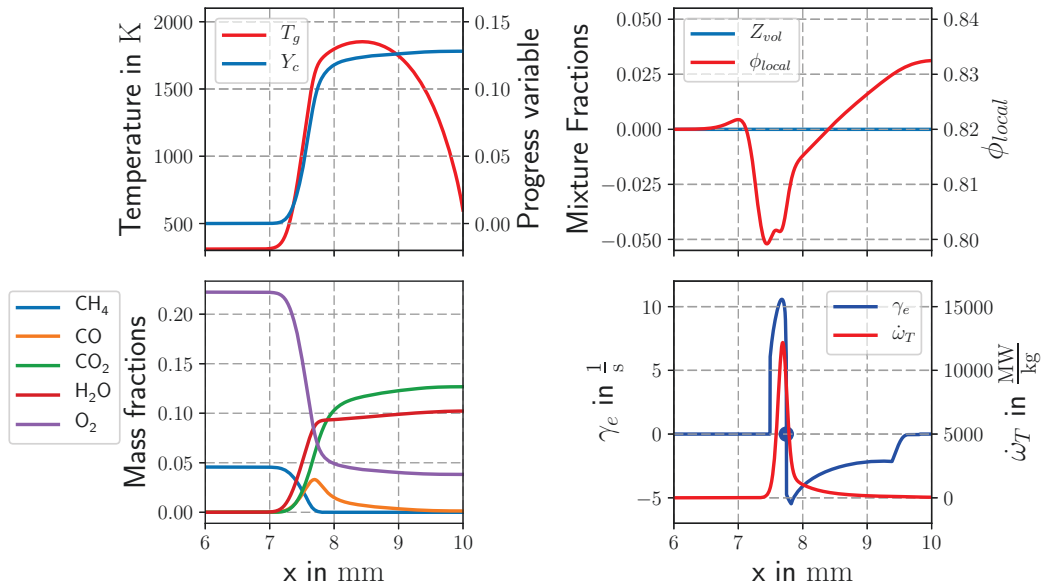


Figure 3.9.: The flame structure analysis of the strained methane-air stagnation flow for Xia-Mech.

mode are aligned at same position, identifying a premixed flame front.

RESULTS

The locally calculated equivalence ratio ϕ_{local} (upper right plot) and available oxygen (lower left plot) illustrate the lean character of the premixed flame. The fluctuations in the ratio is due to the mixture-average diffusion. The volatile mixture fraction Z_{vol} (upper right plot) stays at zero over the whole domain, because no coal is introduced in this setup.

In the upper left plot of Fig. 3.9 the almost aligned temperature and progress variable profiles in the ignition zone again demonstrate a purely premixed flame front.

Based on the flame structure analysis, an *a posteriori* analysis is applied for a PFLUT for this case without coal loading.

The a posteriori analysis for the methane-air stagnation flow flame

The *a posteriori* analysis results in Fig. 3.10 for the temperature and OH depict a slight shift in the profiles towards the nozzle. This is a well-known issue when using tables based on

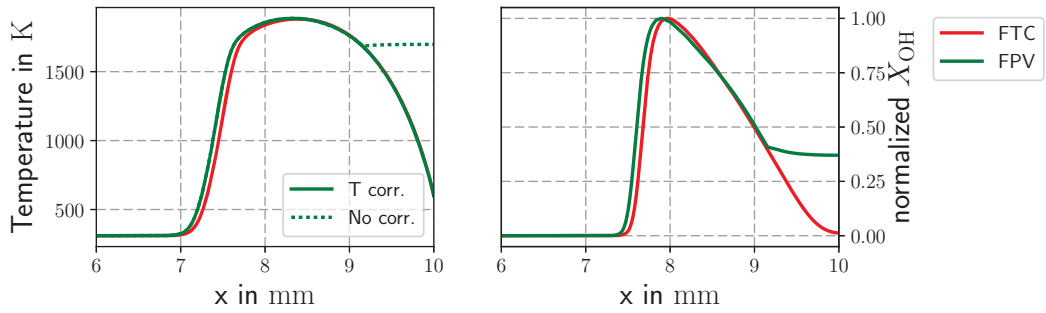


Figure 3.10.: The *a posteriori* analysis for the strained methane-air stagnation flow for mixture-averaged diffusion modeling and CRECK-based mechanism.

premixed flames with mixture-average diffusion modeling. Additionally, a big deviation can be observed near the wall for the normalized X_{OH} profile in the right plot. Due to the cooled wall, a huge enthalpy defect is introduced, which is greater than the included ones in the table. Therefore, the temperature has to be adjusted according to Eq. (3.3), otherwise a maximum error of 1000 K would occur near the wall when comparing the corrected and uncorrected temperatures of the FPV model in the left plot. No correction is known for species, therefore the deviations in the species profile start exactly at the point where a temperature correction needs to be applied.

In order to verify the general procedure, the $Le = 1$ approach is additionally applied for the *a posteriori* analysis. As a result, no shift in the profiles can be observed in Fig. 3.11, which is again consistent with the literature [36]. The deviation in the species profile on the right is again due to a huge enthalpy effect as discussed above for the mixture-average approach.

In conclusion, the non-adiabatic FPV approach is able to reproduce the FTC results for a methane-air stagnation flow flame well, as long as the enthalpy level is valid for table. The correction of the temperature has to be applied in this configuration, otherwise an error in temperature of 1000 K will occur for the PFLUT considered.

RESULTS

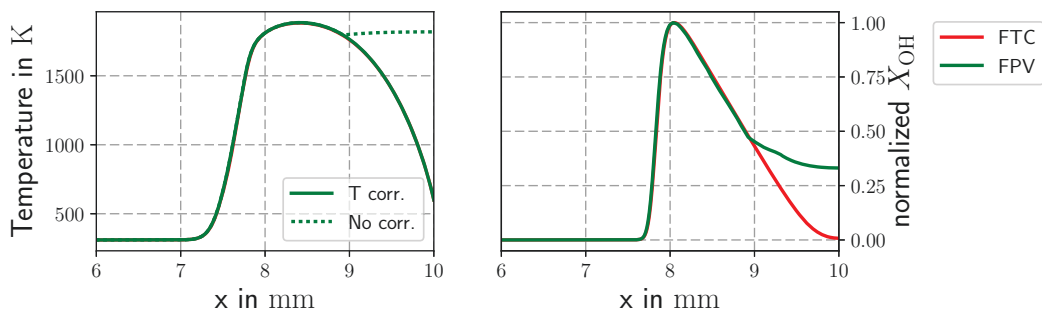


Figure 3.11.: The *a posteriori* analysis for the strained methane-air stagnation flow for $Le=1$ diffusion modeling and CRECK-based mechanism.

3.2.2 Coal-methane-air flame

In the following, the missing coal parameters are described, which are necessary to perform the calculations considering coal in the configuration. A flame structure analysis and an *a posteriori* analysis are performed for the default parameters. Afterwards, the results' sensitivity to the selected parameters is discussed.

A grounded high volatile lignite called Heizprofi (HP) is used in the experiments and the corresponding ultimate and proximate analyses are given in Table 3.5 [9]. The parameters

Table 3.5.: Proximate and ultimate analysis of Heizprofi (HP) lignite [9].

Proximate analysis		Ultimate analysis	
Volatile matter	50.6	C	69.0
Fixed carbon	45.1	H	5.0
Moisture	19.0	O	24.7
Ash	4.3	N	0.8
		S	0.5

for the SFOR model and volatile composition in Table 3.6 are obtained using the calibrating procedure with the CPD model as discussed by Vascellari et al. [5]. The reported Sauter mean diameter (SMD) is $15 \mu\text{m}$ and an emissivity of $\varepsilon = 0.85$ is used.

By assuming that the particles are spherical, the coal-to-oxidizer ratio α can be calculated from the number density n_p , particle density ρ_p , particle diameter d_p and gas density ρ_g :

$$V_p = \frac{1}{6} \pi d_p^3, \quad (3.4)$$

$$\alpha = n_p V_p \frac{\rho_p}{\rho_g}. \quad (3.5)$$

For the recorded values [9] the coal-to-oxidizer ratio α has a value of $0.0666 \frac{\text{kg}_{\text{coal}}}{\text{kg}_{\text{air}}}$.

The reference case is performed using the Xia-Mech mechanism and a mono-disperse distribution with an initial diameter equal to the reported SMD. The comparison of the cases with and without coal is shown in 3.12 for the temperature and normalized X_{OH} profile. The igni-

RESULTS

Table 3.6.: Parameters of the SFOR devolatilization model and volatile composition for Heizprofil (HP) lignite.

SFOR model	
A	$236.012 \times 10^3 \frac{1}{s}$
E	$47.0827 \frac{\text{kJ}}{\text{molK}}$
y_{vol}	0.67
Volatile composition (% mass)	
CO_2	45.796%
CO	6.477%
H_2	4.213%
C_6H_6	42.316%
N_2	1.198%

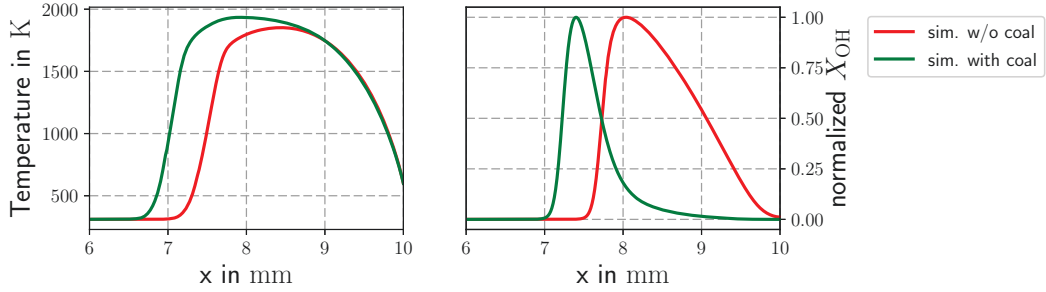


Figure 3.12.: Influence of introducing coal on the position of the flame front in the coal-methane-air stagnation flow flame using MA-diffusion approach and the Xia-Mech mechanism. Left plot: temperature profiles, right plot: normalized X_{OH} profiles.

tion zone of the coal flame is shifted towards the nozzle, due to the additionally available fuel from the coal compared to the purely gaseous configuration. The slope of the temperature profiles in the ignition zone is not affected. The temperature profiles near the wall are almost similar, so cooling by the wall is dominant in this region. An increase in the temperature peak is also visible when coal particles are introduced.

As well as the X_{OH} profile shifting, it also becomes more narrow compared to the gaseous configuration. This is an indication, that the volatiles are released in a very small region in the reference case.

Flame structure analysis for the coal-methane-air stagnation flow flame

The results of the flame structure analysis for the reference case are displayed in Fig. 3.13. The profiles for the gaseous and particle temperature, as well as the PV are shown in the upper left plot. The ignition of the gaseous phase promotes the release of volatiles and the rise in the particle temperature. Near the wall, the cooling of the isothermal wall is dominant, as a consequence of which the temperatures are almost identical. The progress variable Y_c rises

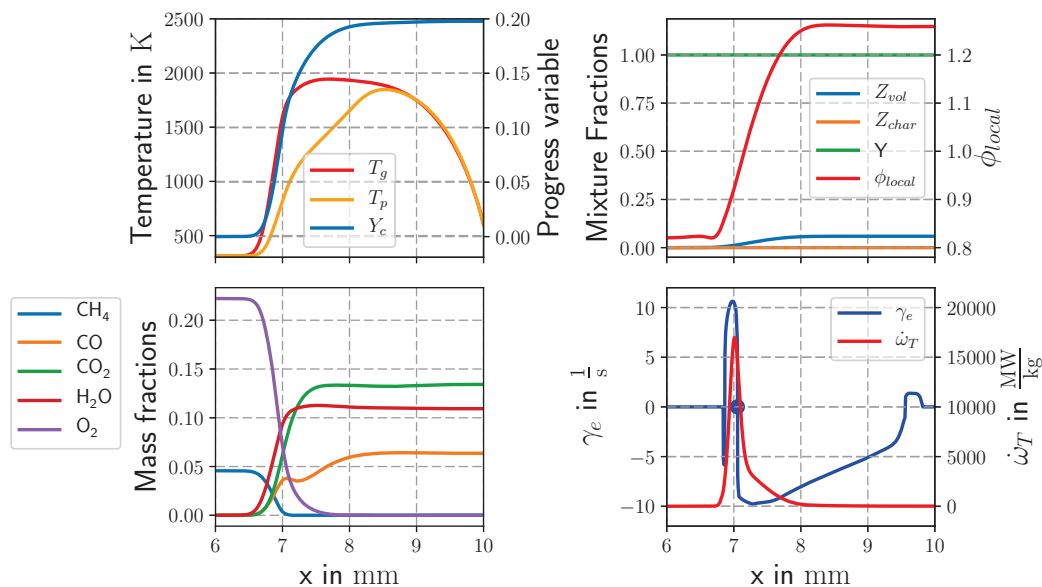


Figure 3.13.: Flame structure analysis for the coal-methane-air case investigated by Xia et al. [9]. Upper left: temperature of gaseous phase and dispersed phase as well as the PV, upper right: flamelet parameters Z_{vol} , Z_{vol} , Y and the local equivalence ratio ϕ_{local} , lower left: major species profiles, lower right: flame markers γ_e and $\dot{\omega}_T$.

immediately near the ignition zone and stays almost constant afterwards, which is similar to the purely gaseous setup.

When coal is introduced to methane-air flame, the equivalence ratio ϕ_{local} (upper right plot) becomes greater than one, so the flame characteristic changes from lean to fuel-rich. This finding is supported by oxygen vanishing near the wall (lower left plot). The upper right plot of Fig. 3.13 also indicates the importance of pyrolysis modeling in this setup, because the value of Y is almost identically one, and consequently Z_{char} remains zero, therefore no char oxidation occurs in this setup.

The flame markers - the chemical mode γ_e and the HRR $\dot{\omega}_T$ - in the lower right corner indicate that there is just one premixed flame, similarly to the purely gaseous setup. The only peak of HRR and the zero-crossing of the chemical mode are both aligned at the same position, illustrating that there is a premixed flame front.

As with to the pure gaseous setup discussed before, the *a posteriori* analysis is performed for a PFLUT. The result of this analysis is described in the following section.

The a posteriori analysis for the coal-methane-air stagnation flow flame

The results of the *a posteriori* analysis for the reference case are shown in Figure 3.14. Similarly to the discussion for the pure gaseous calculation a little shift in the ignition zone is observed for the temperature (lower left plot) and X_{OH} (lower right plot) profiles. The maximum temperature for the FPV solution is lower compared to the FTC solution, which

RESULTS

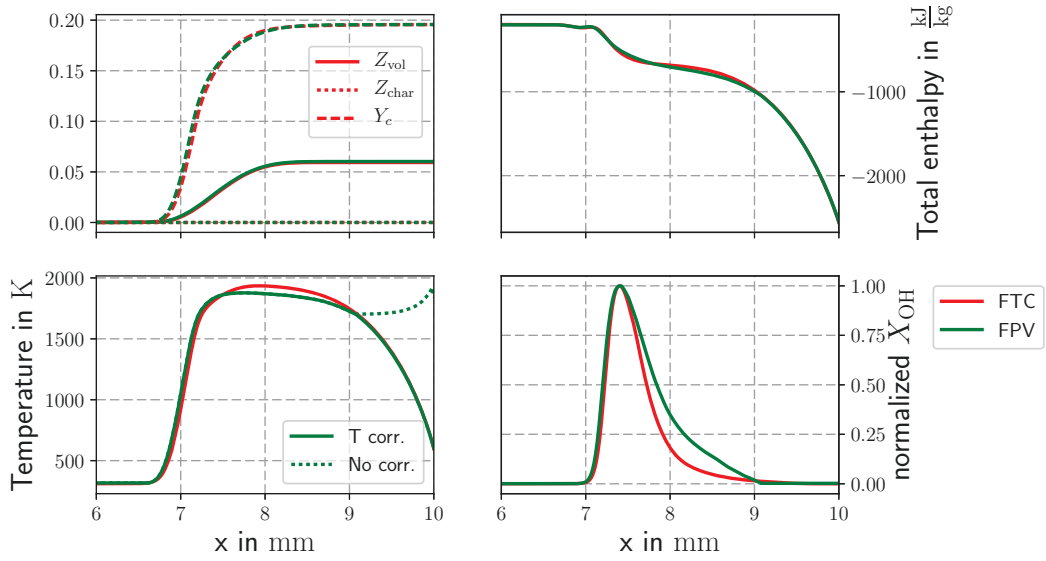


Figure 3.14.: The *a posteriori* analysis with a PFLUT for the reference case. Upper left: flamelet parameters Z_{vol} , Z_{char} , Y_c , upper right: total enthalpy h_g , lower left: temperature, right: normalized X_{OH} profiles.

was not visible for the methane-air flame. However, the general trend is well reproduced if a temperature correction is considered.

The peak position of the X_{OH} profile is captured well by the FPV calculation, while the profile is wider towards the wall. The deviations for the OH occur exact in the same region, where temperature is underestimated.

The same shift is also observable for the control variables Z_{vol} , Y_c and h_g (first row). The trends of total enthalpy h_g profiles (upper right plot) are inline with the findings for the temperatures as expected. The regions with deviations in PV are aligned with the occurrence of the deviations for the temperature profile. Based on these findings it is assumed that discrepancies are mostly connected to the definition of the PV and the corresponding source term, which is tabulated in the applied PFLUT.

Comparison with experiments

The comparison of all experimental profiles for OH, $C_2\cdot$ and $CH\cdot$ in Fig. 3.15 indicates that there is a mismatch in the prediction of the peak positions prediction of OH (upper right) and $CH\cdot$ (lower left). While the numerical X_{OH} profile is shifted towards the nozzle compared to experiments, the numerical $X_{CH\cdot}$ profile is shifted towards the wall. Additionally, the contrary trends of the peak predictions for the $CH\cdot$ and $C_2\cdot$ profiles are consistent with the discussion on Fig. 3.8.

In conclusion, with the current coal parameters the wideness and the general trend of the experimental profiles cannot be reproduced. Therefore, the results' sensitivity to changes in the numerical setup will be investigated in the following.

RESULTS

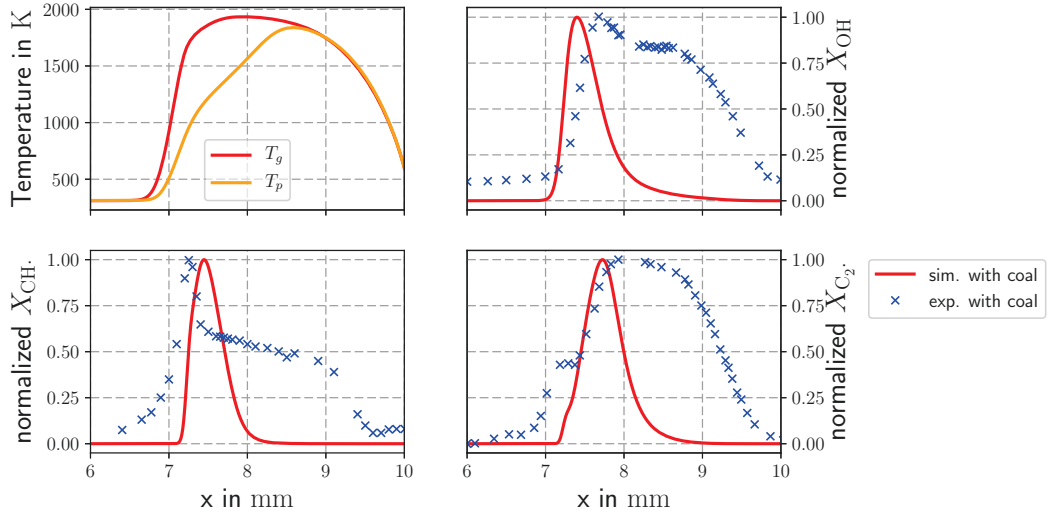


Figure 3.15.: Comparison of coal-methane-air stagnation flow with experiments including coal [9].

Influence of mechanism

Including higher hydrocarbons like tar (here simplified as C_6H_6) the GRI-3.0 mechanism cannot be used any more for the coal cases. The results for mechanisms study are available in Fig. 3.16 for the CRECK-based mechanism and the Xia-Mech mechanism. From pure gaseous

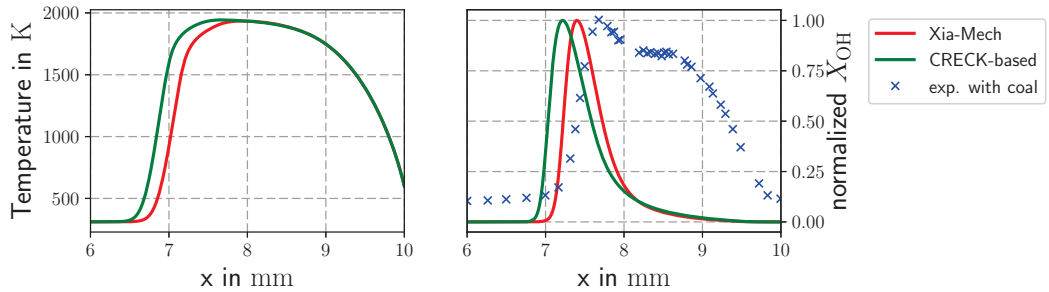


Figure 3.16.: Comparison of profiles for two mechanisms, left plot: temperature, right plot: normalized OH mole fraction profiles compared to experiments [9].

simulations almost no influence could be observed for the mechanisms used. This changes with the injection of coal particles. The ignition position of the flame for CRECK-based simulation is shifted even further away from the wall compared to the shift between experiments and the results for the Xia-Mech mechanism. Maybe this originates in the reduction process from the CRECK mechanism [95] to the CRECK-based mechanism discussed by Tufano et al. [97], which was performed for other operating conditions.

Influence of particle size distribution

In all other calculations up to now, a mono-disperse distribution of coal particles with a diameter of $15\mu m$ has been used, as suggested by Xia et al. [9]. However, in practical

RESULTS

applications a particle size distribution is observed for grounded coal. Therefore, this study will use the Rosin-Rammler-Sperling-Bennett (RRSB) distribution in its original formulation [104]

$$RRSB - PDF(d_p) = 1 - \exp\left(\left(-\frac{d_p}{d_{p,0}}\right)^n\right) \quad (3.6)$$

to investigate the influence of the particle size distribution on the results. The value of this probability density function (PDF) for a diameter d_p describes the probability of finding particles with that diameter or smaller values. An approximation of this distribution for a fixed spread parameter $n = 5$ was obtained by optimizing $d_{p,0}$ for nine particle classes in order to achieve a Sauter Mean Diameter (SMD) of $15 \mu\text{m}$ reported in the experiments [9]. The corresponding mass fractions for the particle classes is given in Table 3.7 for $n = 5$ and $d_{p,0} = 14.895$. For a visual impression, Fig. 3.17 illustrates the distribution (left) and the

Table 3.7.: Mass fractions of the particle size distribution based on RRSB.

d_p in μm	5.0	7.5	10.0	12.5	15.0	17.5	20.0	22.5	25.0
Mass fraction	0.0001	0.0031	0.0253	0.1100	0.2719	0.3521	0.1987	0.0372	0.0016

mass fraction (right) of the selected particle classes. For the given parameters, the probability

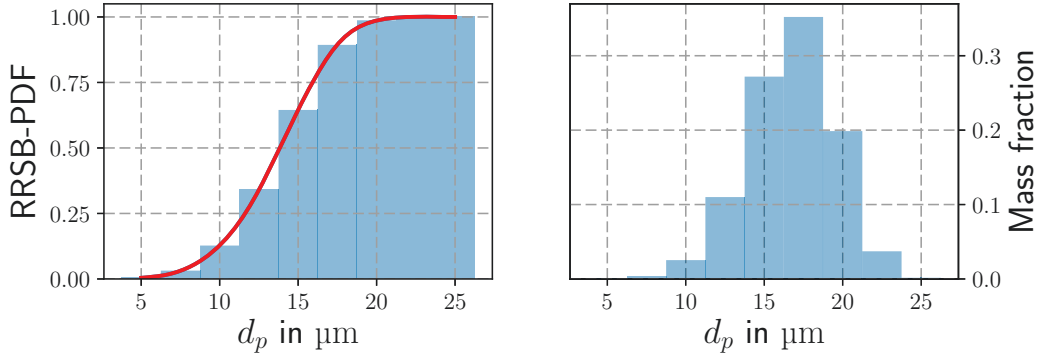


Figure 3.17.: The RRSB distribution. Left: RRSB-PDF as in Eq. (3.6) and the corresponding approximation, right: mass fractions of particle classes as in Table 3.7.

of finding particles with a diameter greater than $17.5 \mu\text{m}$ is below 20%. The distribution of the mass fractions is skewed to the left, meaning that the mass of the distribution is more concentrated on the right-hand side of the figure.

The calculated SMD of this distribution is $16.21 \mu\text{m}$ and therefore comparable to the measured value [9].

The results of this study is shown in Figure 3.18. The overall behaviour of the simulations does not change significantly, as shown for the gas temperature and normalized X_{OH} profiles. In conclusion, the assumption of using a mono-disperse distribution is valid in this flame configuration; only minor deviations occur in the region where OH is consumed after the ignition zone. It is important to note that the influence of the spread parameter n and the

RESULTS

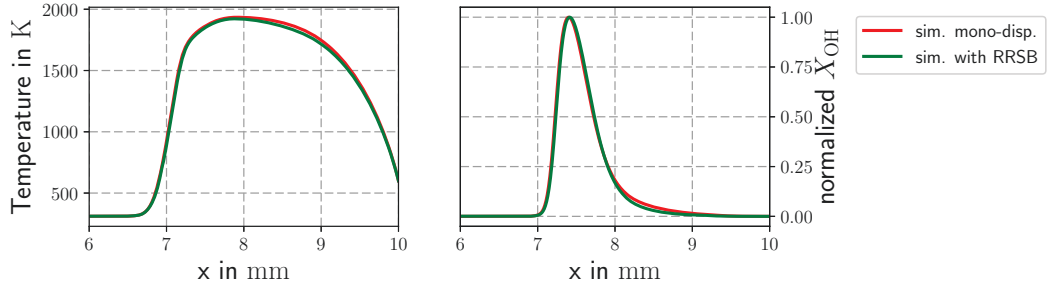


Figure 3.18.: Comparison of mono-disperse distribution and the RRSB distribution. Left: temperature, right: mole fraction of OH.

influence of number of particle classes was not investigated here, because no information on the particle size distribution were given for the experiments.

The poly-disperse simulation provides some insights into the particle behaviour for different particle diameters. The particle temperatures of five selected particle classes are visualised in the left-hand side of Fig. 3.19. It is interesting to note that the mono-disperse particle

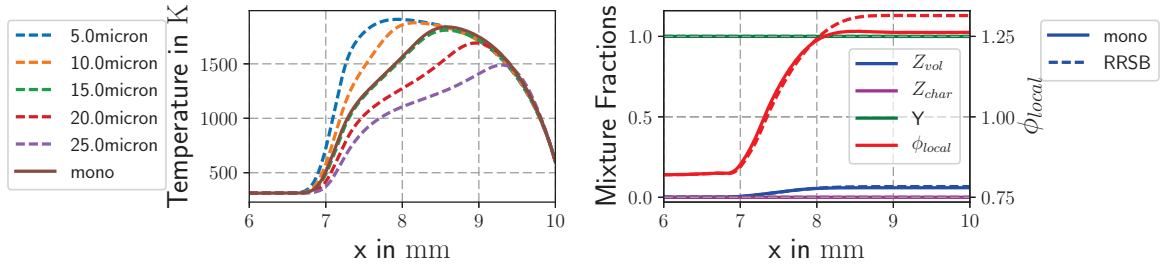


Figure 3.19.: Comparison of mono-disperse distribution and the RRSB distribution. Left: Particle temperatures, right: mixture fractions and ϕ_{local} .

temperature shows a similar trend compared to the corresponding particle size class of the poly-disperse simulation. The fact that bigger particles need more time to heat-up than smaller ones is not surprising at all.

The greatest deviation can be observed for the locally calculated equivalence ratio ϕ_{local} . Based on that ratio, the RRSB case releases more fuel. This is due to the fact that small particles were able to use the available oxygen for char combustion. Overall, however, there is still not sufficient char burnout, due to the lack of oxygen for the majority of the particles. However, for the other reported quantities, the mixture fractions Z_{vol} , Z_{char} and the ratio Y , there are just minor changes in Z_{vol} ,

Influence of coal type / SFOR parameters

The flame structure analysis showed that pyrolysis plays an important role. In a first step a comparison is made between the HP coal and South Beulah (SB) lignite. Afterwards, the SFOR parameters were optimized in order to match the experimental data [9].

RESULTS

The ultimate and proximate analyses for the SB is given in Table 3.8 and are comparable to corresponding values for the HP coal. The SB coal contains more ash and less volatiles compared to HP based on proximate analysis. The SB coal was investigated numerically by

Table 3.8.: Proximate and ultimate analysis of South Beulah (SB) lignite [9].

Proximate analysis		Ultimate analysis	
Volatile matter	38.6	C	71.8
Fixed carbon	47.7	H	4.7
Moisture	18.1	O	19.2
Ash	13.7	N	1.4
		S	2.9

[9], the corresponding parameters for SFOR model and volatile composition (Tab. 3.9) were obtained by personal communication with Xia [10]. The kinetic rates $k_{vol} = Ae^{(-E/RT_p)}$ for

Table 3.9.: Parameters of the SFOR devolatilization model and volatile composition for South Beulah (SB) lignite.

SFOR model		Volatile composition (% mass)			
A	$1.58 \times 10^8 \frac{1}{s}$	CH ₄	3.4%	C ₂ H ₄	1.04%
E	$1.28 \times 10^2 \frac{kJ}{molK}$	CO	17.0%	C ₂ H ₆	1.04%
y_{vol}	0.6	CO ₂	15.0%	C ₃ H ₆	1.04%
		H ₂	0.66%	C ₃ H ₈	0.52%
		H ₂ O	12.0%	C ₆ H ₆	48.3%

both coal are plotted in Arrhenius diagram Fig. 3.20. The kinetic rate for the SB coal is much

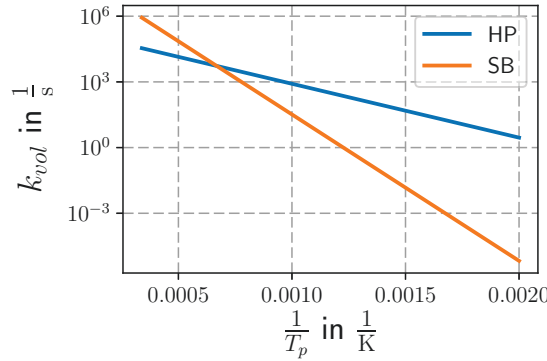


Figure 3.20.: Arrhenius diagram for kinetic rates k_{vol} for both coals HP and SP.

smaller for lower temperature compared to the HP rate. Therefore, a shift of the ignition zone towards the wall is expected when the coal is changed from HP to SB.

The results for the influence of coals and their parameters are given in Fig. 3.21 for Xia-Mech. The general trends of the temperature and the species profiles are similar, but the

RESULTS

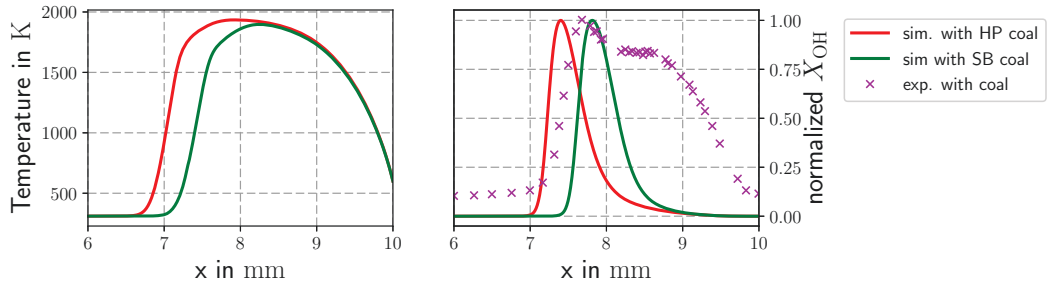


Figure 3.21.: Influence of coal types on the position of the flame front, left plot: temperature, right plot: normalized OH mole fraction profiles compared to experiments [9].

ignition zone of the flame is shifted towards the wall when the results for the SB coal are compared with the results for the HP coal, which is consistent with the findings on Figure 3.20.

The peak in the experimental data for the normalized X_{OH} is exactly between the numerical profiles. The sensitivity of the X_{OH} peak position to the SFOR parameters is high, so this strained stagnation flame is mainly driven by the pyrolysis process, which is also consistent with the findings from the flame structure analysis.

The SFOR parameters were optimized using the same genetic algorithm as described in Vascellari et al. [5]. For the objective function, the deviations between simulation and experimental X_{OH} data was used. The optimized parameters obtained are listed in Table 3.10. A

Table 3.10.: Optimized parameters of the SFOR devolatilization model and volatile composition for Heizprofi (HP) lignite.

SFOR model		Volatile composition (% mass)	
A	$3.31 \times 10^8 \frac{1}{\text{s}}$	CO_2	8.8705%
E	$9.48 \times 10^1 \frac{\text{kJ}}{\text{mol K}}$	CO	73.3584%
y_{vol}	0.41	H_2	11.6339%
		C_6H_6	2.6116%
		N_2	3.5256%

comparison of the simulations with the optimized parameters and the experimental data is given in Fig. 3.22. The peak position of the OH profile in the upper right plot is now captured well, but the second hump of the experimental X_{OH} profile is still not captured. The reasons for this could be related to the pyrolysis model used and the corresponding assumptions

- fixed volatile composition,
- tar is considered to be C_6H_6 only.

For the $\text{CH}\cdot$ profile a similar trend to the experiments can be observed; however, the position of the peak is not captured. Finally, the numerical $X_{\text{C}_2\cdot}$ shows a completely different trend than the experimental profile, but there are similarities compared to the reported numerical profiles [9].

RESULTS

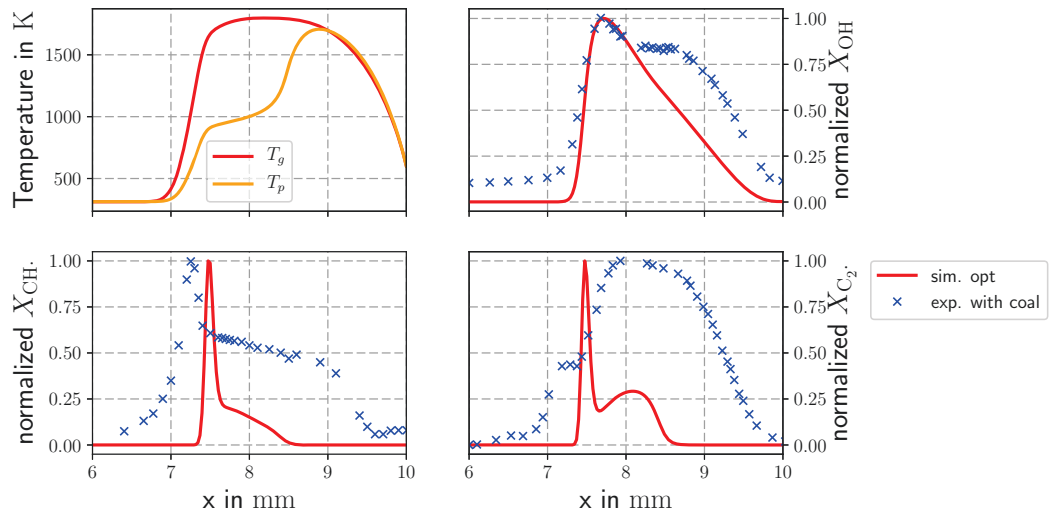


Figure 3.22.: Results of coal-methane-air stagnation flame with the optimized parameter compared with experiments including coal [9].

RESULTS

3.2.3 Intermediate summary for stagnation flow flames reported in [9]

The major findings for the strained stagnation flow flames considered can be summarized as follows:

- The developed code was first validated for pure gaseous cases.
- The coal-loaded case reported by [9] shows almost no char burnout.
- The assumption of using only mono-dispersed distribution is valid in the flame investigated here.
- The flame structure analysis indicates one premixed flame for both experimental setups.
- The cooled wall produces huge enthalpy loss in the flames which were not completely covered by the applied PFLUT.
- The overall trend of the flames was reproduced by an *a posteriori* analysis.
- Numerical results show high sensitivity to the SFOR parameters; for the optimized parameters the general trend and the peak position for species OH were reproduced.

3.3 MODIFIED STAGNATION FLOW CASE FOR ENHANCED CHAR-BURNOUT

The stagnation flow case originally investigated [9] did not show any char burnout. Different adaptations are possible to increase char-burnout, such as

- Increasing oxygen-to-coal ratio, by increasing O_2 content of the system or reduction of coal loading,
- Increasing residence time of the particles, by decreasing v_{in} or increasing the domain.

In order to achieve char burnout, new experiments were performed and kindly provided by Xia [10]. They increased the distance between the nozzle and the wall from 10 to 20 mm and the inlet velocity from 1.6 to 2.6 $\frac{m}{s}$. The coal-to-oxidizer ratio $\alpha_{in} = 0.066$ was kept the same, while a leaner methane-oxidizer mixture with $\phi_{in} = 0.563$ was used compared to the original value of 0.82. The oxidizer was now enriched air with an oxygen volume fraction of 30%. They again investigated a purely gaseous case and a coal-loaded case. Both cases were used to finally validate the in-house code ULF [50] for coal-loaded flames. Measurements are available for the radicals $OH\cdot$, $CH\cdot$ and $C_2\cdot$. Furthermore, a purely numerical parametric study was carried out to investigate the limits of the FPV approach for the gas and coal phases. All the calculations in this section were performed with the Xia-Mech mechanism. In the coal-loaded experiments the lignite Heizprofi was again used. For the numerical setup, the previously obtained SFOR parameters listed in Table 3.6 are used throughout this section.

RESULTS

3.3.1 Validation

For the validation process, the pure methane-air configuration is investigated first like in the previous setup. The comparison of the experimental data with the obtained results and the

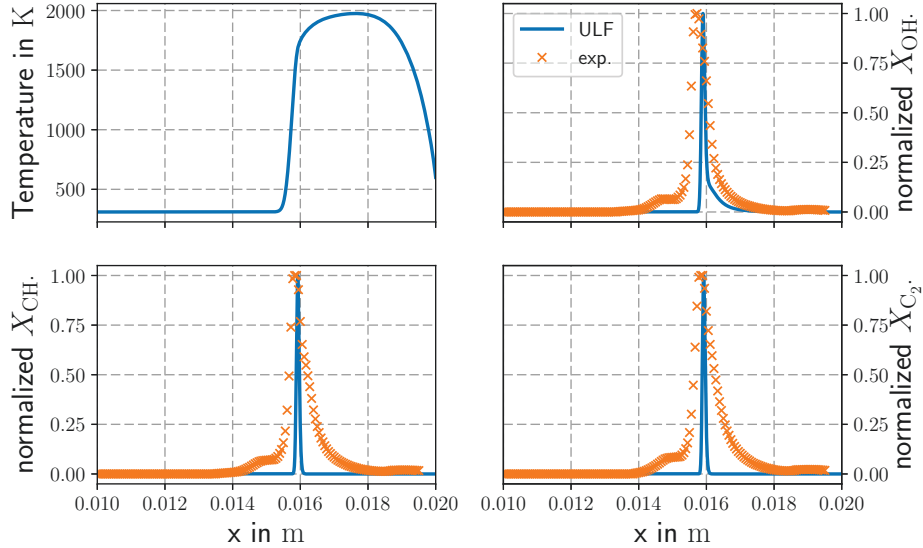


Figure 3.23.: Comparison of numerical results and experimental data for the case of the modified methane-enriched-air stagnation flow. Upper left: temperature of the gas-phase, upper right: normalised X_{OH} profiles, lower left: normalised X_{CH} profile and lower right: normalised X_{C_2} .

temperature of the gaseous phase is given in Fig. 3.23. For all three radicals, the peak position is slightly shifted towards the wall and the experimental profiles are wider than the numerical profiles. For the latter the noise-to-signal ratio is relatively high [10]. However, the numerical species profiles are in fairly good agreement with the experiments, which is consistent with the findings from the previous section.

When coal is introduced into the system, the ignition zone is shifted towards the nozzle as with the original stagnation flow setup as shown in Fig 3.24. This shift is caused by the higher availability of fuel for the coal-loaded case. For the pure gas-phase calculation, the ignition with respect to temperature takes place between 15 and 16 mm and in the case of coal this is shifted by 1 mm towards the nozzle.

For the peak position for the radicals $\text{CH}\cdot$ (lower left) and $\text{C}_2\cdot$ (lower right), the same discussion holds as in Section 3.2. While the simulation predicts the peak of X_{CH} before the corresponding experimental data peak, the prediction for X_{C_2} is reversed. In contrast to the original setup, the trends of numerical profiles for these two radicals are comparable to the experimental trends. For $\text{CH}\cdot$ the numerical profile is even broader than in the experiments, while in the previous study it was impossible to reach the breadth of the experimental data.

The numerical X_{OH} profile shows a completely contrary trend. The peak position is shifted 1.0 mm from the experimental prediction. The shape is also completely different compared

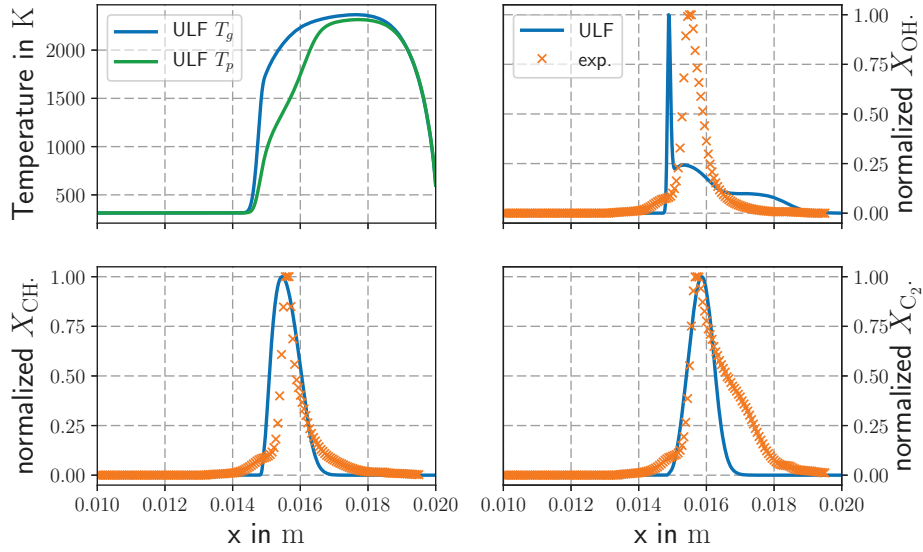


Figure 3.24.: Comparison of numerical results and experimental data for the case of the modified coal-methane-enriched-air stagnation flow case. Upper left: particle temperature and temperature of the gas-phase, upper right: normalised X_{OH} profiles, lower left: normalised X_{CH} profile and lower right: normalised X_{C_2} .

to the experiments. The experimental curve shows one smooth peak, whereas the simulation show one spiky peak followed by two decreasing humps. The reasons for this deviations could be due to a high noise-to-signal ratio [10]. It is more likely that the used sub-mechanism for $\text{OH}\cdot$ fails to predict the experimental profile. The applied sub-mechanism was originally developed by Panoutsos et al. [105] for methane-air flames. Alviso et al. [106] showed the applicability of the sub-mechanism for spray-methane-air flames, the behaviour on enriched air and other higher hydrocarbons such as C_6H_6 remains unclear.

However, considering the uncertainties in the experiments and the parameter sensitivity in the simulation, the overall agreement is sufficient.

3.3.2 Parametric study

In the parametric study the coal-to-oxidizer ratio α_{in} and the inlet velocity v_{in} are varied in order to obtain higher char burnout. All available simulations are a combination of the values listed in Table 3.11, including also the validation case ($\alpha_{in} = 0.066$, $v_{in} = 2.6 \frac{\text{m}}{\text{s}}$).

Table 3.11.: Input parameters for the parametric study of the modified stagnation flow cases.

α_{in}	v_{in} in $\frac{\text{m}}{\text{s}}$
0.033	1.0
0.066	2.0
0.100	2.6

RESULTS

Flame structure analysis for the parametric study

Two studies will be presented in the following. First the influence of v_{in} is investigated with a fixed $\alpha_{in} = 0.066$ and afterwards $v_{in} = 2.0 \frac{\text{m}}{\text{s}}$ is fixed and α_{in} is varied.

INFLUENCE OF INLET VELOCITY ON THE FLAME STRUCTURE Figure 3.25 illustrates the influence of inlet velocity on the flame structure. For all three cases the pyrolysis

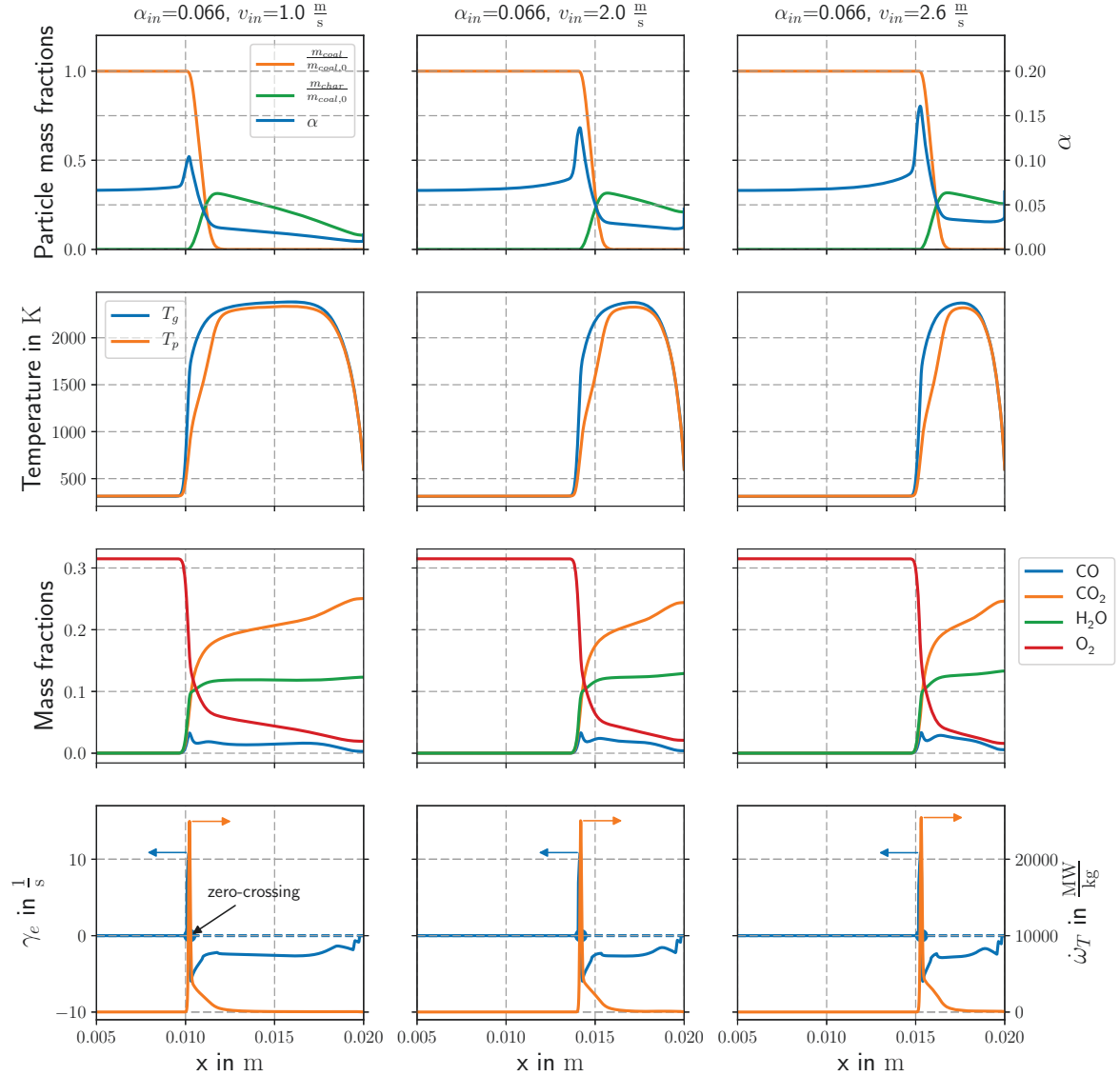


Figure 3.25.: Influence of inlet velocity on the flame structure of a coal-oxidizer stagnation flame with fixed coal-to-oxidizer ratio $\alpha_{in} = 0.066$.

process is finished, indicated by the normalized coal content in the particles $\left(\frac{m_{coal}}{m_{coal,0}}\right)$ in the first row. Please remember that in the modeling approach considered, coal is transformed to char and volatiles (see Eq. (2.12)), therefore in every case first a maximum value for normalized char content $\left(\frac{m_{char}}{m_{coal,0}}\right)$ is reached caused by the pyrolysis process. Afterwards the content decreases due to char burnout. As expected, the case with the longest residence time

RESULTS

($v_{in} = 1.0 \frac{m}{s}$) reaches the highest level of char burnout. The local coal-to-oxidizer ratio α slightly increases towards the ignition zone for all cases caused by the higher inertia of the particles. As soon as the particles reach the flame the α profile drops due to the pyrolysis process. The slight decrease in α towards the wall is caused by char burnout. In the immediate vicinity of the wall it increases again, because of the inertia of the particles.

The general influence of the inlet velocity on the visualized cases is that the ignition zone is shifted towards the wall and the profiles became smaller when the inlet velocity is higher. This general trend is as expected. For the temperature profiles in the second row the general shape and maximum value is the same, just the width of flame grows as the inlet velocity decreases. The behaviour of the major species (row three) is similar in all cases; in line with the temperature profile, only width of the reaction zone becomes smaller with higher velocity. It is remarkable that in all cases oxygen was available near the wall, so the char-burnout is mainly suppressed by the cooled wall.

In the last row the flame markers chemical mode γ_e and HRR $\dot{\omega}_T$ are shown. The zero-crossing of γ_e combined with the single aligned peak of $\dot{\omega}_T$ indicates just one premixed flame for all cases.

INFLUENCE OF COAL LOADING ON THE FLAME STRUCTURE The influence of coal loading on the flame structure for a fixed inlet velocity is depicted in Fig. 3.26. It is interesting to note that the position of the ignition zone does not significantly change with different coal loadings: the stabilisation of the flame depends more on the inlet velocity than on α_{in} . The general trend of α displayed in the first row is similar to the previous studies, except that the values increase with higher loading as expected. Again, all cases show the complete release of the volatiles. The highest level of char burnout is reached by the case with the lowest loading, whereas for the highest loading almost no char burnout occurs due to the oxygen being consumed near the wall due (row three).

The temperature profiles displayed in the second row are very similar in shape and position, except that the maximum value rises when a higher amount of coal is introduced at the inlet. This is consistent with an increase in the product species H_2O and CO_2 with more coal loading, which corresponds to a decrease of O_2 and an overall increase of CO due to incomplete combustion, as illustrated in the third row.

The flame structure analysis of the case with variations of coal loading does not reveal a change in the flame type. There is still one premixed flame as indicated by the zero-crossing of γ_e and an aligned single peak of the HRR $\dot{\omega}_T$ shown in the last row.

In conclusion, the influence of inlet velocity on flame position and shape is much greater compared to influence of the coal loading. Furthermore, the cooling caused by wall prevent char burnout.

RESULTS

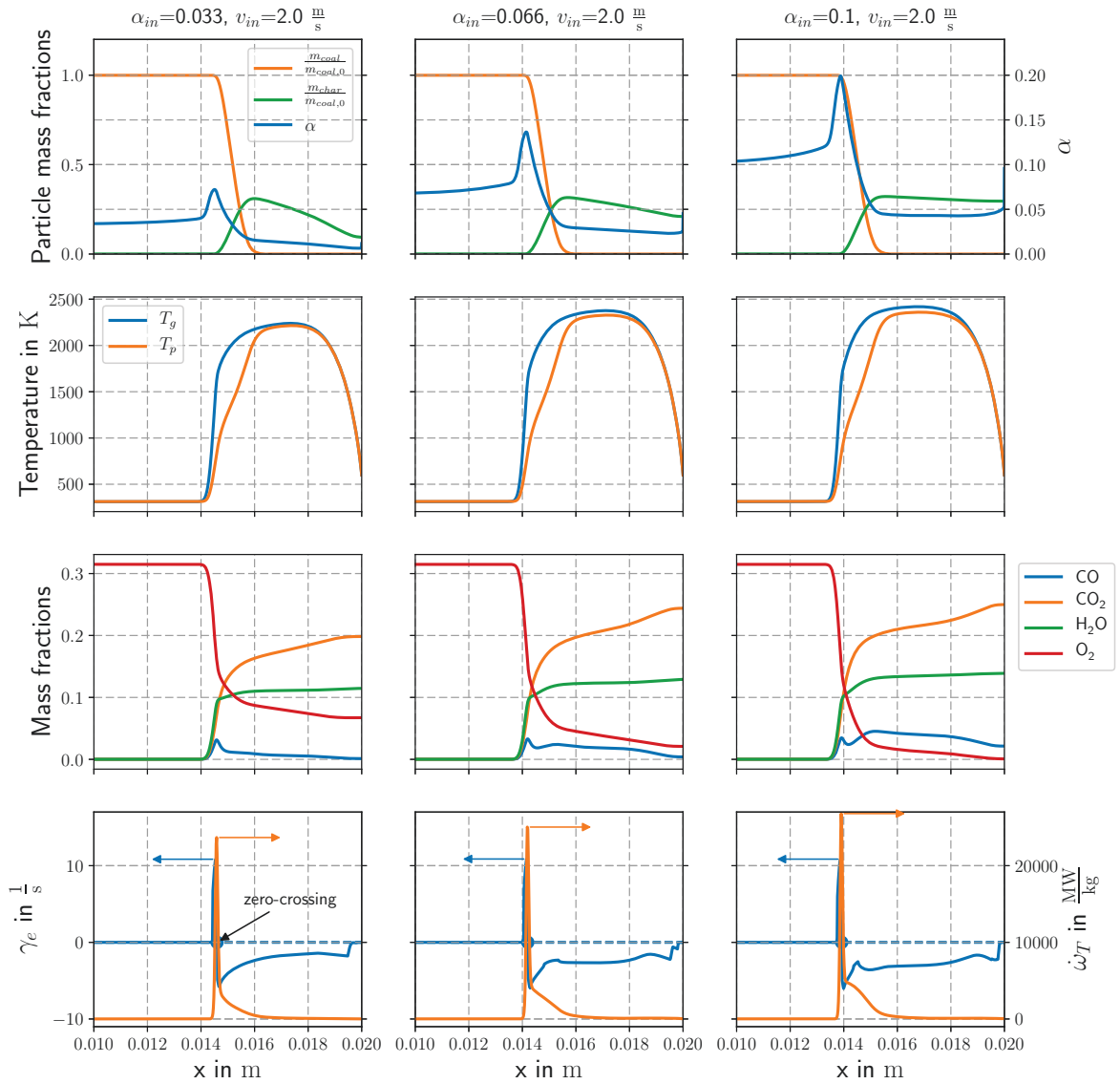


Figure 3.26.: Influence of coal loading on the flame structure of a coal-oxidizer stagnation flame with fixed inlet velocity $v_{in} = 2.0 \frac{m}{s}$.

RESULTS

The a posteriori analysis for the parametric study

Following the findings of the discussion on the flame structure for the parametric study, an *a posteriori* analysis is performed for the whole set of parameters listed in Table 3.11 using a PFLUT. For the sake of consistency, the same studies will be presented here as in the previous section.

INFLUENCE OF INLET VELOCITY ON THE *a posteriori* ANALYSIS The influence of the inlet velocity v_{in} on the results for the *a posteriori* analysis is depicted in Fig. 3.27. In the

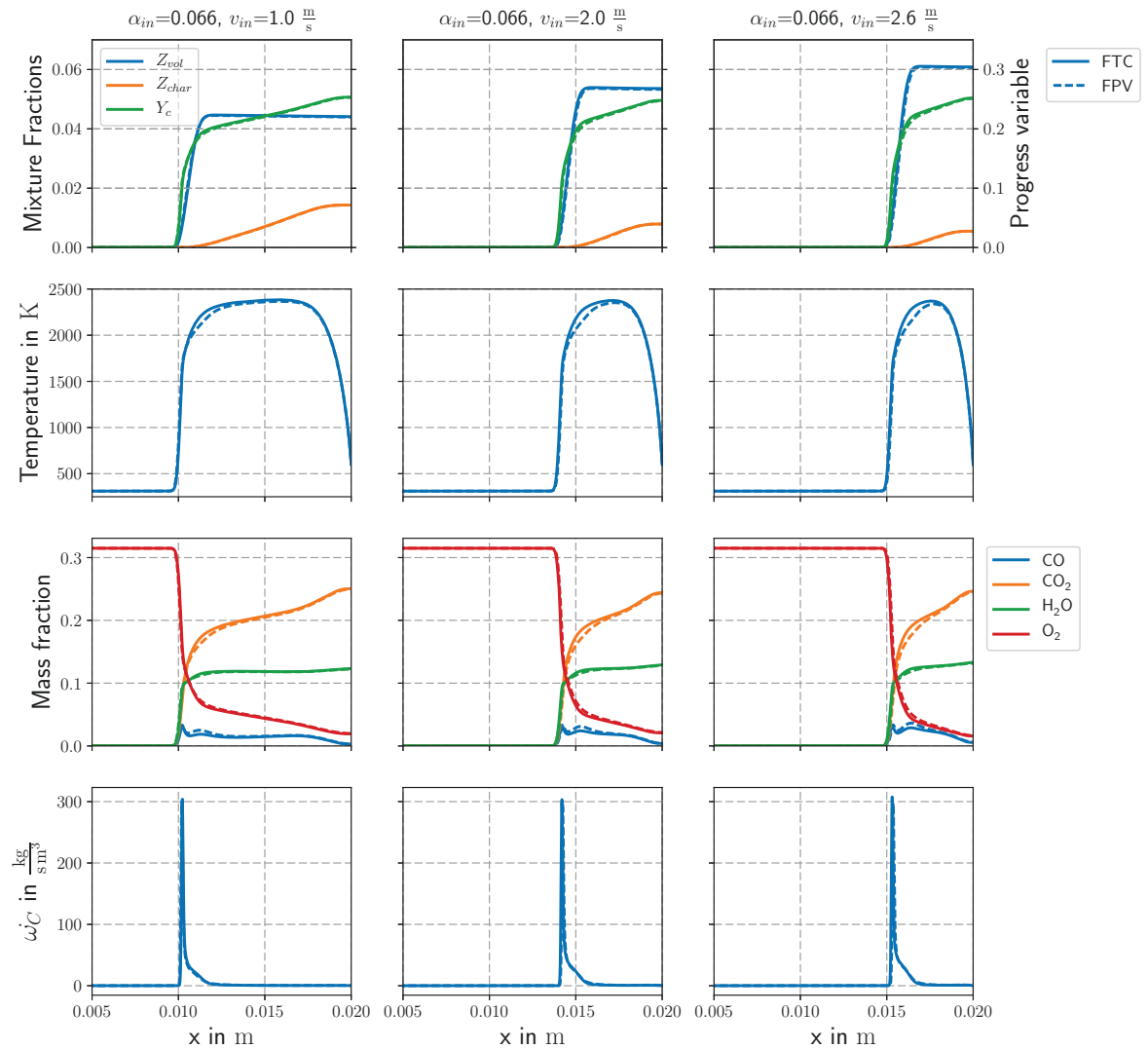


Figure 3.27.: The *a posteriori* analysis of a coal-oxidizer stagnation flame with fixed coal-to-oxidizer ratio $\alpha_{in} = 0.066$ and a varied the inlet velocity. The dashed lines are the results of the FPV model and solid lines representing the FTC solutions.

first row, the comparison for the mixture fractions Z_{vol} and Z_{char} and the progress variable Y_c is shown. For both mixture fractions FTC and FPV models agree very well. The point of rapid increase in Y_c is captured in all three cases however, there are some discrepancies near

RESULTS

the point of the highest curvature in the PV profiles. The differences increase as the velocity rises.

The regions with deviations in PV are aligned with the occurrence of the deviations for the temperature profile displayed in the second row. The underprediction of PV in that regions is doubtless related to the underprediction of temperature. Beside these regions, the temperature and major species profiles for the FTC and FPV solutions in the third row agree well.

Usually, differences in Y_c are connected to differences in the source term $\dot{\omega}_c$ of the progress variable. Therefore, these profiles are visualized in the last row, but no significant differences are observable in order to explain the partial mismatch of the corresponding progress variables.

In conclusion, the *a posteriori* analysis for a PFLUT can reproduce the flame characteristics very well. Any influence of the inlet velocity is unverifiable.

INFLUENCE OF COAL LOADING ON THE *a posteriori* ANALYSIS The results for the influence of coal loading on the *a posteriori* analysis are summarized in Fig. 3.28. In the first row the state variables Z_{vol} , Z_{char} and Y_c are shown. The general structure is well reproduced by the FPV model. However, while the ignition zone of the medium loaded case $\alpha_{in} = 0.066$ is matched well, a small shift towards the nozzle occurs for the lower coal loading and a shift towards the wall is visible for the higher loading case. These deviations in position are also visible also for other reported quantities, such as the gas temperature in the second row, the major species in the third row and the source term of the PV in the last row. The observed shift in the profiles could not be verified in an *a priori* analysis. Maybe the resolution of the table is too weak for a perfect agreement in an *a posteriori* analysis.

Similarly to the previous study, the gas temperature (second row) for the FPV model is slightly underpredicted compared to the FTC solution directly after the ignition, whereas the maximum temperature and the general trend are similar in both methods.

The highest discrepancies for the species (third row) are found near the ignition zone, which is consistent with the findings of the previous study for the influence of the velocity and the discussion on the state variables here. However, the overall progress of the reported species is captured well by the FPV approach.

The progress and the maximum value of the source term of the PV $\dot{\omega}_c$ in the last row is reproduced well, whereas the same shift is also observable as discussed for the other reported properties.

In conclusion, the influence of the coal loading on the results of the *a posteriori* analysis are contradictory. While the overall comparison is good, the prediction of the position for the ignition varies slightly with the coal loading compared to the FTC results. For the lower loading case ($\alpha_{in} = 0.033$) a shift in all the profiles towards the inlet is achieved, whereas the higher loaded case ($\alpha_{in} = 0.1$) predicts a shift towards the wall.

RESULTS

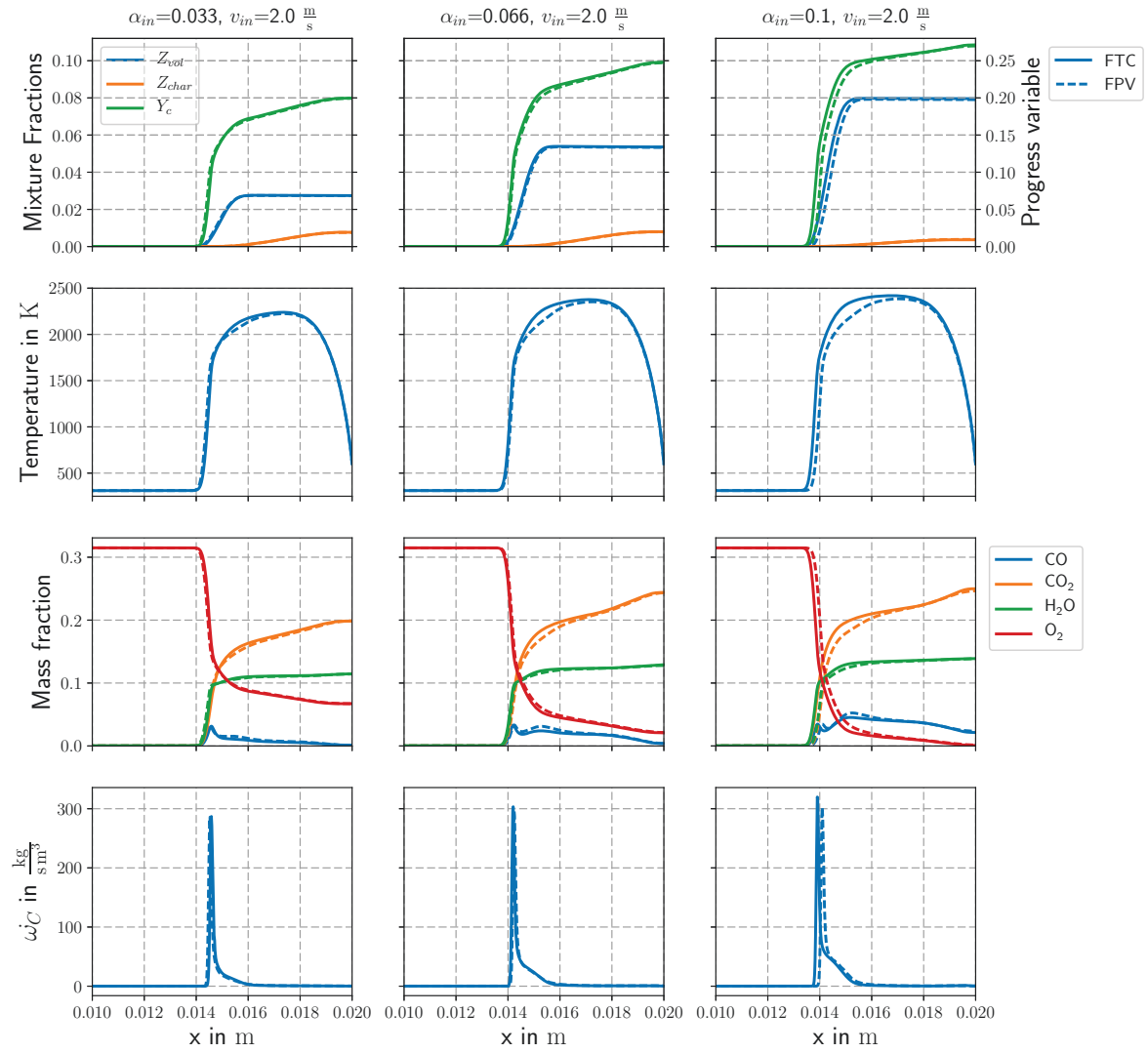


Figure 3.28.: The *a posteriori* analysis of a coal-oxidizer stagnation flame with fixed inlet velocity $v_{in} = 2.0 \frac{\text{m}}{\text{s}}$ by varying the coal-to-oxidizer ratio α_{in} . The dashed lines are the results of the FPV-model and solid lines representing the FTC-solutions.

SUMMARY AND CONCLUSIONS

The purpose of this work was to propose a predictive and computationally affordable method for modeling pulverized coal combustion. A tabulation strategy based on gaseous flamelets was suggested. The advantage of this approach is a detailed description of the chemistry from flamelet look-up tables (FLUTs) at moderate computational costs, since only a small set of control parameters has to be transported in CFD. This approach can be transferred to turbulent coal-loaded flames. The models considered for coal particles are selected to close the gap between the accurate prediction of the coal conversion process and being computationally affordable for use in fully coupled simulations. Therefore, simple kinetic models are calibrated in advance with highly sophisticated, structure-based single particle models. Special focus is placed on restoring the overall mass and energy balance, further including temperature-dependent properties for the coal such as enthalpy, heat capacity and the pyrolysis heat. It was proven that non-adiabatic effects have to be included in the FLUTs due to the intense heat exchange between the gaseous and dispersed phases.

The thesis reports on tabulation strategies based on diffusion and premixed flame structures. The applicability of the tabulation strategies was assessed with *a priori* and *a posteriori* analyses. In an *a priori* analysis the thermo-chemical state of a detailed chemistry solution is compared with the tabulated one. Therefore, the control variables for the table look-up are taken from the detailed solution. This analysis enables the standalone error to be evaluated for a specific table. The *a posteriori* analysis measures the cumulated error for the tabulation strategy by comparing the state of a fully coupled simulation with the detailed one. One-dimensional configurations are considered in the thesis, because only simple, resolved configurations with well-defined boundary conditions allow the model to be assessed properly. In all applications considered, the suitable table is identified by flame structure analysis using different flame markers to determine the burning mode.

The first solely numerical test case observes two preheated, opposing air streams in a counterflow configuration, one stream being additionally loaded with coal. The flame structure analysis shows a complex interplay of premixed and non-premixed flame structures for the detailed chemistry solutions. Two tables with different burning modes were evaluated with an *a priori* analysis for different inlet velocities and coal loadings. It turns out that the

consideration of non-adiabatic effects is necessary because of an intense transfer of heat and mass between the gas phase and coal particles. Furthermore, a table based on non-premixed flame structures is able to reproduce the complex flame structures. The usability of this table was finally demonstrated with the *a posteriori* analysis.

The validation of the code and workflow developed and models used was performed against experimental data for lean methane-oxygen-nitrogen mixtures impinging on a wall. The experiments were carried out with and without coal loading, which allowed for stepwise validation of pure gaseous phase modeling and the used coal models. It turns out that the most sensitive part of the simulation results was the pyrolysis modeling, while the differences between the mono-disperse and the Rosin-Rammler-Sperling-Bennett size distribution modeling was negligible. The domination of premixed flames in all cases was demonstrated by the flame structure analysis, which suggested the usage of a corresponding FLUT based on premixed flame structures. The *a posteriori* analysis for this kind of a table shows good agreement with the detailed chemistry solutions.

In order to demonstrate the validity and robustness of the tabulation strategy suggested, a parametric study is presented on the effect of inlet velocity and coal loading on the results. The greatest influence on the flame structure is based on the inlet velocities. The biggest deviations in an *a posteriori* analysis are observed for the coal loading; however, the approach was still able to reproduce the general trends.

In conclusion, for the laminar configurations considered, tables with different burning modes are necessary. This could be due to some disadvantages of the tabulation strategies used, as discussed hereafter. The proposed tabulation strategy based on premixed flame structures is not able to consider mixing along the mixture fraction direction and does not account for strain effects. One option for subsequent works could be to consider reactants-to-products or stratified mixtures in a counterflow configuration. For tables based on steady laminar flamelets, the gradient of the progress variable is directly linked to the scalar dissipation rate. Therefore, the rate of mixing determines the reaction progress. The development of two-dimensional flamelet equations for the mixture fraction and progress variable would solve that issue.

Throughout the thesis, coal drying was neglected. There are two possible ways of overcoming this fact. In both approaches, a third mixture fraction is necessary to describe the mixing of moisture with the other streams. The first approach assumes that drying is fast and therefore mixing with the oxidizer occurs before the interactions with volatiles and the products of char burnout. Based on the coal loading, the moisture of the coal could be directly considered part of the oxidizer for boundary conditions in canonical flame setups for the tables. The tables are created as proposed in this thesis. In the second approach, all possible combinations of the three mixture fractions have to be considered when creating the tables. In subsequent studies both approaches should be evaluated for different configurations and different coals.

SUMMARY AND CONCLUSIONS

This thesis addresses laminar configurations for a direct assessment of flamelet tabulation strategies. For application in turbulent coal flames, the laminar tables have to be filtered, as briefly discussed in the thesis. Future works will need to filter the tables and evaluate their applicability in turbulent coal flame simulations. The necessary framework is already coupled to several turbulent flame solver.

Another interesting point is to further investigate the influence of char burnout. This thesis considers the reaction of char with oxygen. The application of other heterogeneous reactions such as the Boudouard reaction or the heterogeneous water gas reaction would lead to more mixture fractions for tabulation strategies. However, the influence of these reactions could be investigated in a further study of a detailed chemistry solution.

To close it can be stated that this thesis forms the foundation for further investigations into the simulation large-scale pulverized coal combustors.

A

APPENDIX

A.1 DETAILED DESCRIPTION OF THE SOLUTION PROCEDURE

This sections deals with solution procedure of the derived stationary equations in Sections 2.2.3 and 2.3.6.

The main idea is to split the equations in two sets and solving the sets iteratively in succession by fixing the solution of the respective other set [65]. The first set describes the governing equations for gaseous properties and the second set contains the stationary equations for the coal particles (Section 2.2.2). The solution procedure of gaseous properties is given in Section A.1.1, while the particle equation are solved in the Lagrangian way (Section A.1.2).

A.1.1 *Modified damped Newton's method with pseudo time stepping*

For the first set of equations a finite differencing approach is used to obtain an algebraic set of equation

$$F(\phi) = 0, \quad (\text{A.1})$$

where F is the residual vector and ϕ the solution of the equation set. The Newton's method in the original form

$$\phi_{n+1} = \phi_n - \left(\frac{\partial F}{\partial \phi} \right)_{\phi_n}^{-1} F(\phi_n) \quad (\text{A.2})$$

is an iteratively process which converges quadratically, if the initial solution ϕ_0 is sufficiently good¹. This procedure is to time consuming and could lead to unphysical intermediate results therefore the modified damped Newton method is applied here

$$\phi_{n+1} = \phi_n - \lambda_n (J_n)^{-1} F(\phi_n) \quad (\text{A.3})$$

where, $\lambda \in (0, 1]$ is the damping parameter to ensure validity and the Jacobian J_n is equal to the previously used Jacobian J_{n-1} or reevaluated as $J_n = \frac{\partial F}{\partial \phi_{\phi_n}}$. Instead of computing the inverse of the Jacobian the linear equation system $J_n \Delta \phi_n = F(\phi_n)$ is solved, where $\Delta \phi_n = \phi_{n+1}|_{\lambda_n=1} - \phi_n$ is the undamped correction vector. The selection of J_n and λ_n is

¹ The initial solution ϕ_0 has to be placed in the convergence region of the final solution ϕ .

governed by a look-ahead procedure to the solution of ϕ_{n+2} . The criterion [107] for accepting ϕ_{n+1} is that the undamped steps decrease in magnitude

$$|(J_n)^{-1}F(\phi_{n+1})| < |(J_n)^{-1}F(\phi_n)|. \quad (\text{A.4})$$

If this criterion is not fulfilled by ϕ_{n+1} , the procedure restarts with a halved damping factor or a reevaluation of J_n . The damped Newton method stops, if the undamped correction vector $\Delta\phi_n$ is below an user selected threshold.

If the procedure is not able solve the system (Eq. (A.1)) within a certain amount of steps, then pseudo time stepping is performed. Therefore a pseudo-time derivative is defined as the left-hand side of the residual vector F

$$\frac{\partial\phi}{\partial\tau} = F(\phi). \quad (\text{A.5})$$

Let $\phi_{0,k}$ be an initial guess and the damped Newton method is not able to converge. The next potential initial guess $\phi_{0,k+1}$ is obtained by solving the ordinary differential equation (ODE) system (A.5) for a certain pseudo time step $\Delta\tau_k$ with initial state $\phi_{0,k}$.

Pseudo time stepping is performed until the damped Newton solver converges.

A.1.2 Lagrangian tracking

The particle equations do not contain any diffusion terms, therefore they can be transformed to a Lagrangian framework by introduction a pseudo residence time τ of the particle. Following relation is valid for τ

$$v_p \frac{\partial\phi}{\partial x} = \frac{\partial\phi}{\partial\tau}. \quad (\text{A.6})$$

With relation (A.6) the Lagrangian version of Equations (2.46)-(2.50) read:

$$\frac{\partial m_p}{\partial\tau} = -\dot{m}_p, \quad (\text{A.7})$$

$$m_p \frac{\partial U_p}{\partial\tau} = -\frac{F_r}{r} - m_p U_p^2, \quad (\text{A.8})$$

$$m_p \frac{\partial v_p}{\partial\tau} = -F_x, \quad (\text{A.9})$$

$$m_p c_{p,p} \frac{\partial T_p}{\partial\tau} = -\dot{q}_{\text{conv}} - \dot{q}_{\text{rad}} - \dot{m}_{\text{vol}} \Delta h_{\text{pyr}}(T_p) - \dot{m}_{\text{char}} \Delta h_{\text{cb}}(T_p), \quad (\text{A.10})$$

$$\frac{\partial n_p}{\partial\tau} = -2n_p U_p - n_p \frac{\partial v_p}{\partial x}. \quad (\text{A.11})$$

The solution of the particles are obtained by solving above ODE system with the initial state of the particles at the inlet. For the sake of simplicity the inlet position of the particles is at x_0 . In order to update the particle properties from Lagrangian framework back to the Eulerian

grid x of the gaseous phase solution, the residence time to reach position x_i is calculated according to

$$\begin{aligned}\tau_0 &= 0.0, \\ \tau_{i+1} &= \tau_i + 0.5 \left(\frac{1}{u_{p_i}} + \frac{1}{u_{p_{i+1}}} \right) (x_{i+1} - x_i),\end{aligned}\quad (\text{A.12})$$

and the above ODE system is solved from τ_i to τ_{i+1} . To determine the particle velocity $u_{p_{i+1}}$ the previous/initial solution of the particles is used. All necessary gas-phase properties $\phi(t)$ for $t \in [\tau_i, \tau_{i+1}]$ are linearly interpolated between ϕ_i and ϕ_{i+1} , as well as the term $\frac{\partial v_p}{\partial x}$ in Equation (A.11).

The Lagrangian tracking is numerically much more robust compared to Eulerian framework.

A.2 DERIVATION OF FLAMELET MODEL FOR NON-PREMIXED FLAMES

This section includes the derivation of the laminar flamelet equations by using $Le_k = 1$ for all species k . As a first step the conservative form of the Equations (2.24), (2.25) and (2.63) are needed. Therefore the product rule for the derivatives of $\rho_g \phi$

$$\frac{\partial}{\partial y} (\rho_g \phi) = \rho_g \frac{\partial \phi}{\partial y} + \phi \frac{\partial \rho_g}{\partial y} \quad (\text{A.13})$$

is applied

$$\rho_g \frac{\partial Z}{\partial t} + Z \frac{\partial \rho_g}{\partial t} + \rho_g u_{g,i} \frac{\partial Z}{\partial x_i} + Z \frac{\partial}{\partial x_i} (\rho_g u_{g,i}) = \frac{\partial}{\partial x_i} \left(\rho_g D_Z \frac{\partial Z}{\partial x_i} \right), \quad (\text{A.14})$$

$$\rho_g \frac{\partial h_g}{\partial t} + h_g \frac{\partial \rho_g}{\partial t} + \rho_g u_{g,i} \frac{\partial h_g}{\partial x_i} + h_g \frac{\partial}{\partial x_i} (\rho_g u_{g,i}) = - \frac{\partial}{\partial x_i} \left(\sum_{k=1}^{N_s} h_{g,k} V_{k,i} \right) + \frac{\partial}{\partial x_i} \left(\lambda_g \frac{\partial T_g}{\partial x_i} \right) + \dot{Q}_R, \quad (\text{A.15})$$

$$\rho_g \frac{\partial Y_k}{\partial t} + Y_k \frac{\partial \rho_g}{\partial t} + \rho_g u_{g,i} \frac{\partial Y_k}{\partial x_i} + Y_k \frac{\partial \rho_g u_{g,i}}{\partial x_i} = - \frac{\partial V_{k,i}}{\partial x_i} + \dot{\omega}_k, \quad (\text{A.16})$$

With continuity Equation (2.22) this reduces to

$$\rho_g \frac{\partial Z}{\partial t} + \rho_g u_{g,i} \frac{\partial Z}{\partial x_i} = \frac{\partial}{\partial x_i} \left(\rho_g D_Z \frac{\partial Z}{\partial x_i} \right), \quad (\text{A.17})$$

$$\rho_g \frac{\partial h_g}{\partial t} + \rho_g u_{g,i} \frac{\partial h_g}{\partial x_i} = - \frac{\partial}{\partial x_i} \left(\sum_{k=1}^{N_s} h_{g,k} V_{k,i} \right) + \frac{\partial}{\partial x_i} \left(\lambda_g \frac{\partial T_g}{\partial x_i} \right) + \dot{Q}_R, \quad (\text{A.18})$$

$$\rho_g \frac{\partial Y_k}{\partial t} + \rho_g u_{g,i} \frac{\partial Y_k}{\partial x_i} = - \frac{\partial V_{k,i}}{\partial x_i} + \dot{\omega}_k, \quad (\text{A.19})$$

APPENDIX

For $Le_k = Le_Z = 1$ it holds

$$V_{k,i} = -\frac{\lambda_g}{c_{p_g}} \frac{\partial Y_k}{\partial x_i}, \quad (\text{A.20})$$

$$\rho_g D_Z = \frac{\lambda_g}{c_{p_g}}. \quad (\text{A.21})$$

Equations (A.18) and (A.19) are now rewritten for $Le = 1$ formulation:

$$\rho_g \frac{\partial h_g}{\partial t} + \rho_g u_{g,i} \frac{\partial h_g}{\partial x_i} = \frac{\partial}{\partial x_i} \left(\sum_{k=1}^{N_s} h_{g,k} \rho_g D_Z \frac{\partial Y_k}{\partial x_i} \right) + \frac{\partial}{\partial x_i} \left(\lambda_g \frac{\partial T_g}{\partial x_i} \right) + \dot{Q}_R, \quad (\text{A.22})$$

$$\rho_g \frac{\partial Y_k}{\partial t} + \rho_g u_{g,i} \frac{\partial Y_k}{\partial x_i} = \frac{\partial}{\partial x_i} \left(\rho_g D_Z \frac{\partial Y_k}{\partial x_i} \right) + \dot{\omega}_k, \quad (\text{A.23})$$

Equation (A.22) can be further reduced by taking the definition of $h_{g,k}$, h_g and the corresponding derivatives $\frac{\partial h_{g,k}}{\partial x_i}$, $\frac{\partial h_g}{\partial x_i}$ into account

$$h_{g,k}(T_g) = \int_{T_0}^{T_g} c_{p,k} dT' + h_{f,k}^0, \quad (\text{A.24})$$

$$\frac{\partial h_{g,k}}{\partial x_i} = c_{p_g,k} \frac{\partial T_g}{\partial x_i}, \quad (\text{A.25})$$

$$h_g = \sum_{k=1}^{N_s} Y_k h_{k,g}, \quad (\text{A.26})$$

$$\frac{\partial h_g}{\partial x_i} = c_{p_g} \frac{\partial T_g}{\partial x_i} + \sum_{k=1}^{N_s} h_{g,k} \frac{\partial Y_k}{\partial x_i}. \quad (\text{A.27})$$

By usage of Equations (A.21) and (A.27) Equation (A.22) reduces to

$$\rho_g \frac{\partial h_g}{\partial t} + \rho_g u_{g,i} \frac{\partial h_g}{\partial x_i} = \frac{\partial}{\partial x_i} \left(\rho_g D_Z \frac{\partial h_g}{\partial x_i} \right) + \dot{Q}_R, \quad (\text{A.28})$$

Now the transformation rules

$$\begin{aligned} \frac{\partial}{\partial t} &= \frac{\partial}{\partial \tau} + \frac{\partial Z}{\partial t} \frac{\partial}{\partial Z}, \\ \frac{\partial}{\partial x_1} &= \frac{\partial Z}{\partial x_1} \frac{\partial}{\partial Z}, \\ \frac{\partial}{\partial x_\beta} &= \frac{\partial}{\partial Z_\beta} + \frac{\partial Z}{\partial x_\beta} \frac{\partial}{\partial Z} \quad (\beta = 2, 3), \end{aligned} \quad (\text{A.29})$$

are applied step by step to the different terms of a general transport equation

$$\rho_g \frac{\partial \phi}{\partial t} + \rho_g u_i \frac{\partial \phi}{\partial x_i} = \frac{\partial}{\partial x_i} \left(\rho_g D_Z \frac{\partial \phi}{\partial x_i} \right) + S_\phi. \quad (\text{A.30})$$

APPENDIX

For a general time derivative $\frac{\partial\phi}{\partial t}$ it follows

$$\frac{\partial\phi}{\partial t} = \frac{\partial\phi}{\partial Z} \frac{\partial Z}{\partial t} + \frac{\partial\phi}{\partial\tau}. \quad (\text{A.31})$$

A general convective term $u_i \frac{\partial\phi}{\partial x_i}$ will be transformed to

$$u_i \frac{\partial\phi}{\partial x_i} = u_1 \frac{\partial Z}{\partial x_1} \frac{\partial\phi}{\partial Z} + u_\beta \frac{\partial Z}{\partial x_\beta} \frac{\partial\phi}{\partial Z} + \underbrace{u_\beta \frac{\partial\phi}{\partial Z_\beta}}_{\approx 0 \text{ (asymptotic analysis[108])}}, \quad (\text{A.32})$$

$$\approx \frac{\partial\phi}{\partial Z} u_i \frac{\partial Z}{\partial x_i}. \quad (\text{A.33})$$

Finally the transformation of the general diffusion term $\frac{\partial}{\partial x_i} \left(\rho_g D_Z \frac{\partial\phi}{\partial x_i} \right)$ gives

$$\begin{aligned} \frac{\partial}{\partial x_i} \left(\rho_g D_Z \frac{\partial\phi}{\partial x_i} \right) &= \frac{\partial}{\partial x_1} \left(\rho_g D_Z \frac{\partial Z}{\partial x_1} \frac{\partial\phi}{\partial Z} \right) + \frac{\partial}{\partial x_\beta} \left(\rho_g D_Z \frac{\partial Z}{\partial x_\beta} \frac{\partial\phi}{\partial Z} + \rho_g D_Z \frac{\partial\phi}{\partial Z_\beta} \right), \\ &\stackrel{(\text{A.29})}{=} \rho_g D_Z \frac{\partial Z}{\partial x_1} \frac{\partial}{\partial x_1} \left(\frac{\partial\phi}{\partial Z} \right) + \frac{\partial\phi}{\partial Z} \frac{\partial}{\partial x_1} \left(\rho_g D_Z \frac{\partial Z}{\partial x_1} \right) \\ &\quad + \rho_g D_Z \frac{\partial Z}{\partial x_\beta} \frac{\partial}{\partial x_\beta} \left(\frac{\partial\phi}{\partial Z} \right) + \frac{\partial\phi}{\partial Z} \frac{\partial}{\partial x_\beta} \left(\rho_g D_Z \frac{\partial Z}{\partial x_\beta} \right) \\ &\quad + \frac{\partial}{\partial x_\beta} \left(\rho_g D_Z \frac{\partial\phi}{\partial Z_\beta} \right), \\ &\stackrel{(\text{A.29})}{=} \frac{\partial\phi}{\partial Z} \frac{\partial}{\partial x_i} \left(\rho_g D_Z \frac{\partial Z}{\partial x_i} \right) + \frac{\partial}{\partial x_\beta} \left(\rho_g D_Z \frac{\partial\phi}{\partial Z_\beta} \right) \\ &\quad + \rho_g D_Z \left(\frac{\partial^2\phi}{\partial Z^2} \sum_{k=1}^3 \left(\frac{\partial Z}{\partial x_k} \right)^2 + \frac{\partial Z}{\partial x_\beta} \frac{\partial}{\partial Z_\beta} \left(\frac{\partial\phi}{\partial Z} \right) \right), \\ &= \frac{\partial\phi}{\partial Z} \frac{\partial}{\partial x_i} \left(\rho_g D_Z \frac{\partial Z}{\partial x_i} \right) + \frac{\partial^2\phi}{\partial Z^2} \underbrace{\rho_g D_Z \frac{\partial Z}{\partial x_i} \frac{\partial Z}{\partial x_i}}_{=:\frac{\chi}{2}} \\ &\quad + \underbrace{\frac{\partial}{\partial x_\beta} \left(\rho_g D_Z \frac{\partial\phi}{\partial Z_\beta} \right) + \rho_g D_Z \frac{\partial Z}{\partial x_\beta} \frac{\partial}{\partial Z_\beta} \left(\frac{\partial\phi}{\partial Z} \right)}_{\approx 0 \text{ (asymptotic analysis[108])}}, \\ &\approx \frac{\partial\phi}{\partial Z} \frac{\partial}{\partial x_i} \left(\rho_g D_Z \frac{\partial Z}{\partial x_i} \right) + \frac{\rho_g \chi}{2} \frac{\partial\phi}{\partial Z}. \end{aligned} \quad (\text{A.34})$$

To retrieve the transformed version of Equation (A.30) the Equations (A.31) to (A.34) has to be add up

$$\rho_g \frac{\partial\phi}{\partial\tau} + \frac{\partial\phi}{\partial Z} \underbrace{\left(\rho_g \frac{\partial Z}{\partial t} + \rho_g u_i \frac{\partial Z}{\partial x_i} - \frac{\partial}{\partial x_i} \left(\rho_g D_Z \frac{\partial Z}{\partial x_i} \right) \right)}_{=0, \text{ according to Eq. (A.17)}} = \frac{\rho_g \chi}{2} \frac{\partial^2\phi}{\partial Z^2} + S_\phi. \quad (\text{A.35})$$

APPENDIX

The $Le = 1$ -formulation of flamelet equations is obtained for $\phi = h_g$ and $\phi = Y_k$:

$$\rho_g \frac{\partial h_g}{\partial \tau} = \frac{\rho_g \chi}{2} \frac{\partial^2 h_g}{\partial Z^2} + \dot{Q}_R \dots, \quad (\text{A.36})$$

$$\rho_g \frac{\partial Y_k}{\partial \tau} = \frac{\rho_g \chi}{2} \frac{\partial^2 Y_k}{\partial Z^2} + \dot{\omega}_k \dots \quad (\text{A.37})$$

Very common is solve the temperature equation instead of enthalpy equation. The derivation of the temperature equation is based on the linearity² of the derivative and the definition of enthalpy Eq. (A.26). Eq. (A.36) can be rewritten as

$$\rho_g c_{p_g} \frac{\partial T_g}{\partial \tau} + \rho_g \sum_{k=1}^{N_s} h_{g,k} \frac{\partial Y_k}{\partial Z} = \rho_g c_{p_g} \frac{\chi}{2} \frac{\partial^2 T_g}{\partial Z^2} + \frac{\rho_g \chi}{2} \sum_{k=1}^{N_s} h_{g,k} \frac{\partial^2 Y_k}{\partial Z^2} + \dot{Q}_R \quad (\text{A.38})$$

By using Eq. (A.37) the temperature equation is obtained

$$\rho_g c_{p_g} \frac{\partial T_g}{\partial \tau} = \rho_g c_{p_g} \frac{\chi}{2} \frac{\partial^2 T_g}{\partial Z^2} - \underbrace{\sum_{k=1}^{N_s} h_{g,k} \dot{\omega}_k}_{=:\dot{\omega}_T} + \dot{Q}_R \quad (\text{A.39})$$

² A function $f : X \mapsto Y$ is called linear, if following hold: $\forall a, b \in X$ and constant c : $f(ca + b) = cf(a) + f(b)$.

BIBLIOGRAPHY

- [1] David M. Grant, Ronald J. Pugmire, Thomas H. Fletcher, and Alan R. Kerstein. Chemical model of coal devolatilization using percolation lattice statistics. *Energy Fuels*, 3(2):175–186, 1989.
- [2] P. R. Solomon, D. G. Hamblen, R. M. Carangelo, M. A. Serio, and G. V. Deshpande. General model of coal devolatilization. *Energy & Fuels*, 2(4):405–422, 1988.
- [3] Stephen Niksa and Alan R. Kerstein. FLASHCHAIN theory for rapid coal devolatilization kinetics. 1. formulation. *Energy & Fuels*, 5(5):647–665, 1991.
- [4] Stephen Niksa, Gui-Su Liu, and Robert H. Hurt. Coal conversion submodels for design applications at elevated pressures. part i. devolatilization and char oxidation. *Progress in Energy and Combustion Science*, 29(5):425–477, 2003.
- [5] M. Vascellari, R. Arora, M. Pollack, and C. Hasse. Simulation of entrained flow gasification with advanced coal conversion submodels. Part 1: Pyrolysis. *Fuel*, 113:654 – 669, 2013.
- [6] C.D. Pierce and P. Moin. Progress-variable approach for large-eddy simulation of non-premixed turbulent combustion. *Journal of Fluid Mechanics*, 504:73–97, 2004.
- [7] Junya Watanabe, Teruyuki Okazaki, Kenji Yamamoto, Koji Kuramashi, and Akira Baba. Large-eddy simulation of pulverized coal combustion using flamelet model. *Proceedings of the Combustion Institute*, 36(2):2155 – 2163, 2017.
- [8] D. Messig, M. Vascellari, and C. Hasse. Flame structure analysis and flamelet progress variable modelling of strained coal flames. *Combustion Theory and Modelling*, 2017.
- [9] M. Xia, D. Zabrodiec, P. Scouffaire, B. Fiorina, and N. Darabiha. Experimental and numerical studies of pulverized coal combustion in a strained flow configuration. *Proceedings of the Combustion Institute*, 2016.
- [10] Meng Xia. personal communication, 2017.
- [11] U.S. Energy Information Administration. <https://www.eia.gov/outlooks/ieo/world.php>, 2017. Accessed: 2017-07-02.
- [12] G.R. Gavalas. *Coal Pyrolysis*. Number Bd. 4 in Coal Pyrolysis. Elsevier Scientific Publishing Company, 1982.
- [13] T. Poinso and D. Veynante. *Theoretical and Numerical Combustion*. T. Poinso and D. Veynante, third edition, 2012.

BIBLIOGRAPHY

- [14] R. J. Kee, J. A. Miller, and G. H. Evans. A computational model of the structure and extinction of strained, opposed flow, premixed methane-air flames. *Proceedings of the Combustion Institute*, 22:1479–1494, 1988.
- [15] Steffen Weise, Sebastian Popp, Danny Messig, and Christian Hasse. A computationally efficient implementation of tabulated combustion chemistry based on polynomials and automatic source code generation. *Flow, Turbulence and Combustion*, 2017.
- [16] N. Darabiha, P. Scoufflaire, M. Xia, and B. Fiorina. Experimental and numerical studies of pulverized coal combustion in a strained flow configuration. *European Combustion Meeting*, 2015.
- [17] B Fiorina, R Baron, O Gicquel, D Thevenin, S Carpentier, and N Darabiha. Modelling non-adiabatic partially premixed flames using flame-prolongation of ildm. *Combustion Theory and Modelling*, 7(3):449–470, 2003.
- [18] Gui-Su Liu and Stephen Niksa. Coal conversion submodels for design applications at elevated pressures. part II. char gasification. *Progress in Energy and Combustion Science*, 30(6):679–717, 2004.
- [19] Michele Vascellari, Rahul Arora, and Christian Hasse. Simulation of entrained flow gasification with advanced coal conversion submodels. part 2: Char conversion. *Fuel*, 118: 369–384, 2014.
- [20] B. W. Brown, L. D. Smoot, P. J. Smith, and P. O. Hedman. Measurement and prediction of entrained-flow gasification processes. *AIChE Journal*, 34(3):435–446, 1988.
- [21] O. T. Stein, G. Olenik, A. Kronenburg, F. Cavallo Marincola, B. M. Franchetti, A. M. Kempf, M. Ghiani, M. Vascellari, and C. Hasse. Towards Comprehensive Coal Combustion Modelling for LES. *Flow, Turbulence and Combustion*, 90(4):859–884, 2013.
- [22] Seung min Hwang, Ryoichi Kurose, Fumiteru Akamatsu, Hirofumi Tsuji, Hisao Makino, and Masashi Katsuki. Application of optical diagnostics techniques to a laboratory-scale turbulent pulverized coal flame. *Energy & Fuels*, 19(2):382–392, 2005.
- [23] Seung-Min Hwang, Ryoichi Kurose, Fumiteru Akamatsu, Hirofumi Tsuji, Hisao Makino, and Masashi Katsuki. Observation of detailed structure of turbulent pulverized-coal flame by optical measurement (part 1, time-averaged measurement of behavior of pulverized-coal particles and flame structure). *JSME International Journal Series B Fluids and Thermal Engineering*, 49(4):1316–1327, 2006.
- [24] Seung-Min Hwang, Ryoichi Kurose, Fumiteru Akamatsu, Hirofumi Tsuji, Hisao Makino, and Masashi Katsuki. Observation of detailed structure of turbulent pulverized-coal flame by optical measurement (part 2, instantaneous two-dimensional measurement of combustion reaction zone and pulverized-coal particles). *JSME International Journal Series B Fluids and Thermal Engineering*, 49(4):1328–1335, 2006.

BIBLIOGRAPHY

- [25] R. Kurose and H. Makino. Large eddy simulation of a solid-fuel jet flame. *Combustion and Flame*, 135(1–2):1–16, 2003.
- [26] P. Edge, M. Gharebaghi, R. Irons, R. Porter, R.T.J. Porter, M. Pourkashanian, D. Smith, P. Stephenson, and A. Williams. Combustion modelling opportunities and challenges for oxy-coal carbon capture technology. *Chemical Engineering Research and Design*, 89(9):1470 – 1493, 2011. Special Issue on Carbon Capture & Storage.
- [27] B.M. Franchetti, F. Cavallo Marincola, S. Navarro-Martinez, and A.M. Kempf. Large Eddy simulation of a pulverised coal jet flame. *Proceedings of the Combustion Institute*, 34(2):2419–2426, 2013.
- [28] G. Olenik, O.T. Stein, and A. Kronenburg. LES of swirl-stabilised pulverised coal combustion in IFRF furnace No. 1. *Proceedings of the Combustion Institute*, 35(3):2819–2828, 2015.
- [29] M. Rabacal, B.M. Franchetti, F. Cavallo Marincola, F. Proch, M. Costa, C. Hasse, and A.M. Kempf. Large Eddy Simulation of coal combustion in a large-scale laboratory furnace. *Proceedings of the Combustion Institute*, 35(3):3609–3617, 2015.
- [30] B.M. Franchetti, F. Cavallo Marincola, S. Navarro-Martinez, and A.M. Kempf. Large Eddy Simulation of a 100 kWth swirling oxy-coal furnace. *Fuel*, 181:491–502, 2016.
- [31] S.B. Pope. Pdf methods for turbulent reactive flows. *Progress in Energy and Combustion Science*, 11(2):119 – 192, 1985.
- [32] A.Y. Klimenko and R.W. Bilger. Conditional moment closure for turbulent combustion. *Progress in Energy and Combustion Science*, 25(6):595 – 687, 1999.
- [33] A.R. Kerstein. A linear-eddy model of turbulent scalar transport and mixing. *Combustion Science and Technology*, 60:391–421, 1988.
- [34] N. Peters. Laminar diffusion flamelet models in non-premixed turbulent combustion. *Progress in Energy and Combustion Science*, 10:319–339, 1984.
- [35] J.A. Van Oijen and L.P.H. De Goey. Modelling of premixed laminar flames using flamelet-generated manifolds. *Combustion Science and Technology*, 161(1):113–137, 2000.
- [36] O. Gicquel, N. Darabiha, and D. Thévenin. Laminar premixed hydrogen/air counterflow flame simulations using flame prolongation of ILDM with differential diffusion. *Proceedings of the Combustion Institute*, 28(2):1901 – 1908, 2000.
- [37] A Eaton, L Smoot, S Hill, and C Eatough. Components, formulations, solutions, evaluation, and application of comprehensive combustion models. *Progress in Energy and Combustion Science*, 25(4):387–436, 1999.

BIBLIOGRAPHY

- [38] Lei Chen, Sze Zheng Yong, and Ahmed F. Ghoniem. Oxy-fuel combustion of pulverized coal: Characterization, fundamentals, stabilization and cfd modeling. *Progress in Energy and Combustion Science*, 38(2):156 – 214, 2012.
- [39] F. Tabet and I. Gökalp. Review on cfd based models for co-firing coal and biomass. *Renewable and Sustainable Energy Reviews*, 51:1101 – 1114, 2015.
- [40] Junya Watanabe and Kenji Yamamoto. Flamelet model for pulverized coal combustion. *Proceedings of the Combustion Institute*, 35(2):2315 – 2322, 2015.
- [41] Pedro J Coelho. Turbulence–radiation interaction: From theory to application in numerical simulations. *Journal of Heat Transfer*, 134(3):031001 – 031001–13, 2012.
- [42] B. Garten, F. Hunger, D. Messig, B. Stelzner, D. Trimis, and C. Hasse. Detailed radiation modeling of a partial-oxidation flame. *International Journal of Thermal Sciences*, 87:68–84, 2015.
- [43] F. Hunger, B. Stelzner, D. Trimis, and C. Hasse. Flamelet-modeling of inverse rich diffusion flames. *Flow, Turbulence and Combustion*, 90:833–857, 2013.
- [44] Chungeng Yin. On gas and particle radiation in pulverized fuel combustion furnaces. *Applied Energy*, 157:554 – 561, 2015.
- [45] Thomas H. Fletcher. Time-resolved temperature measurements of individual coal particles during devolatilization. *Combustion Science and Technology*, 63(1-3):89–105, 1989.
- [46] Alejandro Molina and Christopher R. Shaddix. Ignition and devolatilization of pulverized bituminous coal particles during oxygen/carbon dioxide coal combustion. *Proceedings of the Combustion Institute*, 31(2):1905–1912, 2007.
- [47] Ryang-Gyoon Kim, Dongfang Li, and Chung-Hwan Jeon. Experimental investigation of ignition behavior for coal rank using a flat flame burner at a high heating rate. *Experimental Thermal and Fluid Science*, 54:212 – 218, 2014.
- [48] International workshop on measurement and computation of turbulent nonpremixed flames. <http://www.sandia.gov/TNF/abstract.html>, 2016.
- [49] Workshop on Measurement and Simulation of Coal and Biomass Conversion. <http://www.cbc.uni-due.de/>, 2017. Accessed: 2017-07-02.
- [50] Axel Zschutschke, Danny Messig, Arne Scholtissek, and Christian Hasse. Universal Laminar Flame Solver (ULF). 2017.
- [51] David Merrick. Mathematical models of the thermal decomposition of coal: 2. Specific heats and heats of reaction. *Fuel*, 62(5):540–546, 1983.

BIBLIOGRAPHY

- [52] David G. Goodwin, Harry K. Moffat, and Raymond L. Speth. Cantera: An object-oriented software toolkit for chemical kinetics, thermodynamics, and transport processes. <http://www.cantera.org>, 2017. Version 2.3.0.
- [53] Stanley Badzioch and Peter G. W. Hawksley. Kinetics of Thermal Decomposition of Pulverized Coal Particles. *Ind. Eng. Chem. Proc. Des. Dev.*, 9(4):521–530, 1970.
- [54] Dieter Förtsch, Frank Kluger, Uwe Schnell, Hartmut Spliethoff, and Klaus R.G. Hein. A kinetic model for the prediction of no emissions from staged combustion of pulverized coal. *Symposium (International) on Combustion*, 27(2):3037–3044, 1998.
- [55] Michael Stöllinger, Bertrand Naud, Dirk Roekaerts, Nijso Beishuizen, and Stefan Heinz. Pdf modeling and simulations of pulverized coal combustion - part 2: Application. *Combustion and Flame*, 160(2):396–410, 2013.
- [56] M. Rieth, A. G. Clements, M. Rabacal, F. Proch, O. T. Stein, and A. M. Kempf. Flamelet LES modeling of coal combustion with detailed devolatilization by directly coupled CPD. *Proceedings of the Combustion Institute*, 2016.
- [57] M. Rieth, F. Proch, M. Rabacal, B. Franchetti, F. Cavallo Marincola, and A.M. Kempf. Flamelet LES of a semi-industrial pulverized coal furnace. *Combustion and Flame*, 2016.
- [58] D Genetti. An Advanced Model of Coal Devolatilization Based on Chemical Structure. Master’s thesis, Department of Chemical Engineering Brigham Young University, 1999.
- [59] W.A. Selvig and F.H. Gibson. Calorific Value of Coal. In H.H. Lowry, editor, *Chemistry of Coal Utilization*, volume I, pages 132–144. J. Wiley & sons, inc., 1945.
- [60] M. M. Baum and P. J. Street. Predicting the combustion behaviour of coal particles. *Combustion Science and Technology*, 3(5):231–243, 1971.
- [61] ANSYS. *ANSYS Fluent Theory Guide*. ANSYS, Inc, 15.0 edition, 2013.
- [62] O. Hirschfelder, C. F. Curtiss, and R. B. Bird. *Molecular Theory of Gases and Liquids*. John Wiley and Sons, New York, 1954.
- [63] T.P. Coffee and J.M. Heimerl. Transport algorithms for premixed, laminar steady-state flames. *Combustion and Flame*, 43:273, 1981.
- [64] R. J. Kee, F. M. Rupley, J. A. Miller, M. E. Coltrin, J. F. Grcar, E. Meeks, H. K. Moffat, A. E. Lutz, G. Dixon-Lewis, M. D. Smooke, J. Warnatz, G. H. Evans, R. S. Larson, R. E. Mitchell, L. R. Petzold, W. C. Reynolds, M. Caracotsios, W. E. Stewart, and P. Glarborg. *OPPDIF, A PROGRAM FOR COMPUTING OPPOSED-FLOW DIFFUSION FLAMES*. Reaction Design, Inc., San Diego, CA, chemkin collection release 3.5 edition, 1999.
- [65] G. Continillo and W.A. Sirignano. Counterflow spray combustion modeling. *Combustion and Flame*, 81(3):325–340, 1990.

BIBLIOGRAPHY

- [66] B. Franzelli, B. Fiorina, and N. Darabiha. A tabulated chemistry method for spray combustion. *Proceedings of the Combustion Institute*, 34(1):1659 – 1666, 2013.
- [67] M. Hossain, J.C. Jones, and W. Malalasekera. Modelling of a bluff-body nonpremixed flame using a coupled radiation/flamelet combustion model. *Flow, Turbulence and Combustion*, 67(3):217–234, 2001.
- [68] A. Kempf, A. Sadiki, and J. Janicka. Prediction of finite chemistry effects using large eddy simulation. *Proceedings of the Combustion Institute*, 29(2):1979 – 1985, 2002.
- [69] K. Claramunt, R. Consul, D. Carbonell, and C.D. Perez-Segarra. Laminar flamelet concept for laminar and turbulent diffusion flames. In *42 nd AIAA Aerospace Sciences Meeting and Exhibit*, 2004.
- [70] H. Pitsch and N. Peters. A consistent flamelet formulation for non-premixed combustion considering differential diffusion effects. *Combustion and Flame*, 114(1-2):26 – 40, 1998.
- [71] M. Ihme, C.M. Cha, and H. Pitsch. Prediction of local extinction and re-ignition effects in non-premixed turbulent combustion using a flamelet/progress variable approach. *Proceedings of the Combustion Institute*, 30(1):793 – 800, 2005.
- [72] H. Pitsch. *Modellierung der Zündung und Schadstoffbildung bei der dieselmotorischen Verbrennung mit Hilfe eines interaktiven Flamelet-Modells*. PhD thesis, RWTH Aachen, 1997.
- [73] A. Scholtissek, W.L. Chan, H. Xu, F. Hunger, H. Kolla, J.H. Chen, M. Ihme, and C. Hasse. A multi-scale asymptotic scaling and regime analysis of flamelet equations including tangential diffusion effects for laminar and turbulent flames. *Combustion and Flame*, 162(4):1507 – 1529, 2015.
- [74] H. Pitsch, H. Barths, and N. Peters. Three-dimensional modeling of nox and soot formation in di-diesel engines using detailed chemistry based on the interactive flamelet approach. In *SAE Technical Paper*. SAE International, 1996.
- [75] G. Lodier, L. Vervisch, V. Moureau, and P. Domingo. Composition-space premixed flamelet solution with differential diffusion for in situ flamelet-generated manifolds. *Combustion and Flame*, 158(10):2009 – 2016, 2011.
- [76] N. Peters. *Turbulent Combustion*. Cambridge University Press, 2000.
- [77] M. Vascellari, H. Xu, and C. Hasse. Flamelet modeling of coal particle ignition. *Proceedings of the Combustion Institute*, 34(2):2445–2452, 2013.
- [78] S. Popp, F. Hunger, S. Hartl, D. Messig, B. Coriton, J.H. Frank, F. Fuest, and C. Hasse. LES flamelet-progress variable modeling and measurements of a turbulent partially-premixed dimethyl ether jet flame. *Combustion and Flame*, 162(8):3016 – 3029, 2015.

BIBLIOGRAPHY

- [79] Michele Vascellari, Hongbin Xu, Sandra Hartl, Franziska Hunger, and Christian Hasse. Flamelet/progress variable modeling of partial oxidation systems: From laboratory flames to pilot-scale reactors. *Chemical Engineering Science*, 134:694–707, 2015.
- [80] Steffen Weise, Danny Messig, Bernd Meyer, and Christian Hasse. An abstraction layer for efficient memory management of tabulated chemistry and flamelet solutions. *Combustion Theory and Modelling*, 17(3):411–430, 2013.
- [81] S. Weise and C. Hasse. Reducing the memory footprint in large eddy simulations of reactive flows. *Parallel Computing*, 49:50–65, 2015.
- [82] K. Claramunt, R. Cònsul, D. Carbonell, and C.D. Pérez-Segarra. Analysis of the laminar flamelet concept for nonpremixed laminar flames. *Combustion and Flame*, 145(4):845 – 862, 2006.
- [83] Y.-S. Niu, L. Vervisch, and P.D. Tao. An optimization-based approach to detailed chemistry tabulation: Automated progress variable definition. *Combustion and Flame*, 160(4): 776 – 785, 2013.
- [84] U. Prüfert, S. Hartl, F. Hunger, D. Messig, M. Eiermann, and C. Hasse. A constrained control approach for the automated choice of an optimal progress variable for chemistry tabulation. *Flow Turbulence and Combustion*, 94(3):593–617, 2015.
- [85] B. Marracino and D. Lentini. Radiation Modelling in Non-Luminous Nonpremixed Turbulent Flames. *Combustion Science and Technology*, 125:23–48, 1997.
- [86] M. Ravikanti, W. Malalasekera, M. Hossain, and T. Mahmud. Flamelet Based NO_x -Radiation Integrated Modelling of Turbulent Non-premixed Flame using Reynolds-stress Closure. *Flow, Turbulence and Combustion*, 81:301–319, 2008. 10.1007/s10494-007-9127-x.
- [87] H. Pitsch. Unsteady flamelet modeling of differential diffusion in turbulent jet diffusion flames. *Combustion and Flame*, 123(3):358 – 374, 2000.
- [88] D. Messig, F. Hunger, J. Keller, and C. Hasse. Evaluation of radiation modeling approaches for non-premixed flamelets considering a laminar methane air flame. *Combustion and Flame*, 160:251–264, 2013.
- [89] M. Ihme and H. Pitsch. Modeling of radiation and nitric oxide formation in turbulent nonpremixed flames using a flamelet/progress variable formulation. *Physics of Fluids*, 20(5), 2008.
- [90] R.S. Barlow and J.H. Frank. Effects of turbulence on species mass fractions in methane/air jet flames. *Symposium (International) on Combustion*, 27(1):1087 – 1095, 1998.
- [91] Martin Rieth. personal communication, 2017.

BIBLIOGRAPHY

- [92] C. Hasse. *A Two-Dimensional Flamelet Model for Multiple Injections in Diesel Engines*. PhD thesis, RWTH Aachen, 2004.
- [93] C. Hasse and N. Peters. A two mixture fraction flamelet model applied to split injections in a DI diesel engine. *Proceedings of the Combustion Institute*, 30(2):2755 – 2762, 2005.
- [94] S. S. Girimaji. Assumed β -pdf model for turbulent mixing: Validation and extension to multiple scalar mixing. *Combustion Science and Technology*, 78(4-6):177–196, 1991.
- [95] Eliseo Ranzi, Alessio Frassoldati, Silvia Granata, and Tiziano Faravelli. Wide-Range Kinetic Modeling Study of the Pyrolysis, Partial Oxidation, and Combustion of Heavy n-Alkanes. *Ind. Eng. Chem. Res.*, 44(14):5170–5183, 2005.
- [96] A. Stagni, A. Frassoldati, A. Cuoci, T. Faravelli, and E. Ranzi. Skeletal mechanism reduction through species-targeted sensitivity analysis. *Combustion and Flame*, 163:382–393, 2016.
- [97] G.L. Tufano, O.T. Stein, A. Kronenburg, A. Frassoldati, T. Faravelli, L. Deng, A.M. Kempf, M. Vascellari, and C. Hasse. Resolved flow simulation of pulverized coal particle devolatilization and ignition in air- and o₂/co₂-atmospheres. *Fuel*, 186:285 – 292, 2016.
- [98] B.O. Ayoola, R. Balachandran, J.H. Frank, E. Mastorakos, and C.F. Kaminski. Spatially resolved heat release rate measurements in turbulent premixed flames. *Combustion and Flame*, 144(1 - 2):1 – 16, 2006.
- [99] Robert L. Gordon, Assaad R. Masri, and Epaminondas Mastorakos. Heat release rate as represented by [OH] x [CH₂O] and its role in autoignition. *Combustion Theory and Modelling*, 13(4):645–670, 2009.
- [100] T. F. Lu, C. S. Yoo, J. H. Chen, and C. K. Law. Three-dimensional direct numerical simulation of a turbulent lifted hydrogen jet flame in heated coflow: a chemical explosive mode analysis. *Journal of Fluid Mechanics*, 652:45–64, 2010.
- [101] Ruiqin Shan, Chun Sang Yoo, Jacqueline H. Chen, and Tianfeng Lu. Computational diagnostics for n-heptane flames with chemical explosive mode analysis. *Combustion and Flame*, 159(10):3119–3127, 2012.
- [102] F. Hunger. *Numerical Simulations of Laminar and Turbulent Partial Oxidation Flames*. PhD thesis, TU Bergakademie Freiberg, 2016.
- [103] G.P. Smith, D.M. Golden, M. Frenklach, W.M. Niguel, B. Eiteneer, M. Goldenberg, C.T. Bowman, R.K. Hanson, S. Song, W.C. Gardiner, Jr., V.V. Lissianski, and Z. Qin. Gas Research Institute. http://www.me.berkeley.edu/gri_mech/version30, 2012.
- [104] P. Rosin and E. Rammler. The laws governing the fineness of powdered coal. *Journal of the Institute of Fuel*, (7):29–36, 1933.

BIBLIOGRAPHY

- [105] C.S. Panoutsos, Y. Hardalupas, and A.M.K.P. Taylor. Numerical evaluation of equivalence ratio measurement using oh^* and ch^* chemiluminescence in premixed and non-premixed methane–air flames. *Combustion and Flame*, 156(2):273 – 291, 2009.
- [106] D. Alviso, J.C. Rolon, P. Scouffaire, and N. Darabiha. Experimental and numerical studies of biodiesel combustion mechanisms using a laminar counterflow spray premixed flame. *Fuel*, 153:154 – 165, 2015.
- [107] P. Deuffhard. A modified newton method for the solution of ill-conditioned systems of nonlinear equations with application to multiple shooting. *Numerische Mathematik*, 22(4):289–315, 1974.
- [108] N. Peters. Local quenching due to flame stretch and non-premixed turbulent combustion. *Combustion Science and Technology*, 30(1-6):1–17, 1983.